Diffractive production of $\pi^- f_1$ in $\pi^- p$ interactions at COMPASS(CERN)

Hao Yang

Munich 2012

Diffractive production of $\pi^- f_1$ in $\pi^- p$ interactions at COMPASS(CERN)

Hao Yang

Dissertation
an der Fakultät für Physik
der Ludwig–Maximilians–Universität
München

vorgelegt von
Hao Yang
aus
JiangSu(China)

München, den 21 May 2012

Erstgutachter: Prof.Dr.Martin Faessler
Zweitgutachter: Prof.Dr.Otmar Biebel
Tag der mündlichen Prüfung: 6 Nov. 2012

Contents

List of Figures

List of Tables

Abstract

Diffractive dissociation of a π^- beam(190 GeV/c) on a proton target was measured at the COMPASS spectrometer. During a run in 2008, a large number of events with $\pi^-\pi^-\pi^+\eta$ in the final state was recorded. Partial wave analyses(PWA) of these data are being performed, concentrating on the kinematic domain of momentum transfer t' from 0.1 to 1.0 GeV^2/c^2.

Subject of this thesis is the diffractive production of X from $\pi^-p \to Xp$ with the subsequent decays $X \to \pi^- f_1$ and $f_1 \to \pi^-\pi^+\eta$. Two different decays of the η were selected: $\eta \to \pi^-\pi^+\pi^0(\gamma\gamma)$ and $\eta \to \gamma\gamma$. A kinematic fitting routine was used to improve the data selection. In order to do the PWA, a Monte Carlo(MC) simulation is needed to account for the detector acceptance. In the mass-independent PWA the angular distributions of the real events are compared with the event distributions imposed on Monte Carlo(MC) events in order to determine the production amplitudes of different assumed partial waves in mass bins of 50 MeV/c^2 of the invariant mass m_X of X in the range $1.3 < m_X < 3.0$ GeV/c^2, by means of a maximum-likelihood-fit. Then a simplified mass-dependent fit of Breit-Wigner amplitudes has been applied to the distributions of production intensities as a function of m_X in order to determine the contributions of known or presumed resonances.

In the $\pi^- f_1$ channel, we focus on the S, P and D wave i.e. orbital angular momentum L=0, 1, 2 between π^- and f_1. Significant intensity and phase motion are observed for the following $J^{PC}M^{\epsilon}$ combinations, where J, P, C, M and ϵ stand for the total angular momentum, parity and charge conjugation, total spin projection and reflectivity: $1^{-+}1^+$ (S wave), $1^{++}0^+$ (P wave), $2^{-+}0^+$ (D wave). Parts of these intensities can be assumed to be linked to the known mesons $\pi_1(1600)$, $a_1(1640)$ and $\pi_2(1880)$. Relative branching ratios of the exotic meson $\pi_1(1600)$ with $J^{PC} = 1^{-+}$ are estimated to be roughly BR$(1^{-+} \to \pi^-\rho(770))$: BR$(1^{-+} \to \pi^-\eta')$: BR$(1^{-+} \to \pi^- f_1)$= 3:1:2.

ZUSAMMENFASSUNG

Die diffraktive Anregung von π^--Mesonen mit einem Impuls von 190 GeV/c an einem Proton Target wurde am COMPASS Spektrometer gemessen. Während einer Messperiode im Jahr 2008 wurde eine grosse Anzahl von Ereignissen mit der Kombination $\pi^-\pi^-\pi^+\eta$ im Endzustand aufgezeichnet. Partialwellenanalysen (PWA) dieser Daten werden durchgeführt. Sie konzentrieren sich auf den kinematischen Bereich von Impulsüberträgen im Quadrat, t', von 0.1 bis 1.0 $(GeV/c)^2$.

Gegenstand dieser Arbeit ist die diffraktive Produktion von angeregten Zuständen X über die Reaktion $\pi^- p \to Xp$ mit den anschliessenden Zerfällen des Systems $X \to \pi^- f_1$ und des Mesons $f_1 \to \pi^+\pi^-\eta$. Zwei daran anschliessende Zerfälle des η -Mesons wurden selektiert: $\eta \to \pi^+\pi^-\pi^0$, wobei $\pi^0 \to 2\gamma$ zerfällt, und der direkte Zerfall $\eta \to 2\gamma$. Ein kinematischer Fit wurde verwendet, um die Datenselektion zu verbessern. Bei der Durchführung der PWA wird eine Monte-Carlo-Simulation (MC) benötigt, um die Detektorakzeptanz zu berücksichtigen. Bei der "massen-unabhängigen" PWA werden die gemessenen Winkelverteilungen der Ereignisse verglichen mit denen, die man theoretisch erwartet mit MC-simulierten Ereignissen, um die Produktionsamplituden der verschiedenen angenommenen Partialwellen in Massenintervallen von 50MeV/c^2 über den Massenbereich $1.3 < m_X < 3.0 GeV/c^2$ der invarianten Masse von X zu bestimmen, mittels eines Maximum-Likelihood-Fits. Im Anschluss daran wurde ein vereinfachter massenabhängiger Fit von Breit-Wigner-Amplituden auf die Produktionsintensitäten der verschiedenen Partialwellen als Funktion von m_X angewandt, um die Beiträge von bekannten oder vermuteten Resonanzen zu bestimmen.

Beim $\pi^- f_1$-Endzustand konzentrieren wir uns auf die S, P und D-Welle, d.h. Bahndrehimpulse L = 0, 1, 2 zwischen π^- und f_1. Signifikante Intensitäts und Phasenbewegungen werden beobachtet für die folgenden $J^{PC}M^{\epsilon}$ Kombinationen, wobei J, P, C, M und ϵ den Gesamtspin, die innere Parität,

die Ladungsparität, die Projektion des Gesamtspins auf die z-Achse und die Reflektivität bezeichnen: $1^{-+}1^{+}$ (S-Welle), $1^{++}0^{+}$ (P-Welle), $2^{-+}0^{+}$ (D-Welle). Teile der beobachteten Intensitäten können mit den bekannten Resonanzen $\pi_1(1600)$, $a_1(1640)$ und $\pi_2(1880)$ in Verbindung gebracht werden. Relative Verzweigungsverhältnisse des exotischen Mesons $\pi_1(1600)$ mit $J^{PC} = 1^{-+}$ wurden abgeschätzt und betragen etwa: $\mathrm{BR}(1^{-+} \to \pi^{-}\rho(770))$: $\mathrm{BR}(1^{-+} \to \pi^{-}\eta')$: $\mathrm{BR}(1^{-+} \to \pi^{-}f_1) = 3{:}1{:}2$.

Chapter 1

Introduction

One of the most important questions in contemporary particle physics is to understand the phenomena related to the dynamics of the strong force. Quantum Chromodynamics (QCD), the theory of the strong interactions, is certainly most successful as its viability has been confirmed by many experiments. However, one of its most striking predictions - the existence of new classes of non-$q\bar{q}$ mesons - still awaits definite experimental confirmation: Glueballs ought to exist, objects composed entirely of valence gluons, as should hybrids, states in which a color-octet $q\bar{q}$ pair is neutralized in color by a constituent gluon[23].

The main lesson that has been learnt from the previous experiments is that the identification of glueballs requires complete information on all neighboring states, in particular include[23]:
1) Availability of high-statistics data samples;
2) Reconstruction of final states containing both neutral and charged particles;
3) Observation of the same meson in many different channels;
4) Production of mesons in different reactions.
Interesting in the context of the search for exotics is the study of diffractively produced meson systems by the use of π^- interactions with a proton[23].

One of the main goals of the COMPASS experiment (located at SPS at CERN: see figure 2.1) is the study of meson spectroscopy in the gluon-rich proton-proton central production and in diffractive pion and kaon scattering. One of the main objectives is to identify new glueballs or hybrid states[22] or to confirm still uncertain candidates. An exotic meson has been observed and published in previous experiments, also by COMPASS. However, the better understanding of exotic states is needed. Subject of this thesis is the diffractive production of X from $\pi^- p \to Xp$ with the subsequent decays $X \to \pi^- f_1$ and

$f_1 \to \pi^-\pi^+\eta$. COMPASS incorporates a large (30 mrad to 180 mrad) and small (0 mrad to 30 mrad) angle spectrometer, which enable the investigation of various physics topics. The good momentum resolution is the advantage of such a twostage spectrometer technique[23].

As for the reasons of interest in the πf_1 channel comparing with the $\pi\rho$, $\pi\eta$ and $\pi\eta^{'}$ channel, we can list the following:
1) Predicted decay of 1^{-+} in πf_1 channel have large branching ratio.
2) The width of f_1 is narrow, almost like η and $\eta^{'}$, so we can treat the decay $X \to \pi^- f_1$ as two-body decay(see section 1.3).
3) Due to the fact that f_1 has higher mass than η, ρ and $\eta^{'}$, the X($m_X > m_\pi + m_{f_1}$) also has higher mass.

In order to provide the necessary knowledge for the physics results presented in this thesis, this chapter covers topical features in meson spectroscopy. First of all, introduce the Standard Model and Quark Model. Then the main properties of mesons are summarized and exotic states are introduced. Finally, a brief overview of the partial wave analysis is given.

1.1 Models

1.1.1 Standard Model

The Standard Model of particle physics is a theory concerning the electromagnetic, weak and strong nuclear interactions which mediate the dynamics of the known subatomic particles. Developed throughout the early and middle 20th century, the current formulation was finalized in the mid 1970s upon experimental confirmation of the existence of quarks. Since then, discoveries of the bottom quark (1977), the top quark (1995) and the tau neutrino (2000) have given credence to the standard model. Because of its success in explaining a wide variety of experimental results, the standard model is sometimes regarded as a theory of almost everything[13].

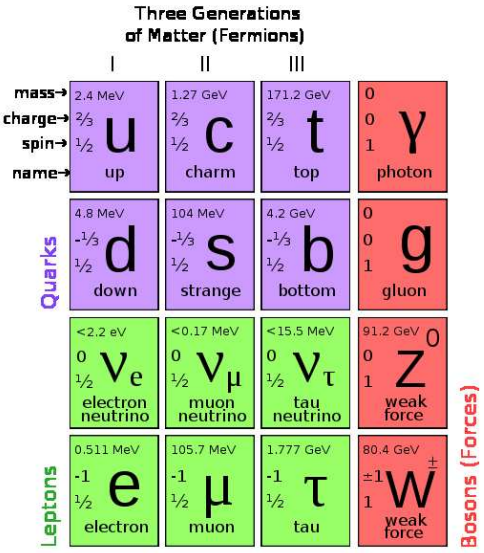

Figure 1.1: The elementary particles of Standard Model[13]

The standard model falls short of being a complete theory of fundamental interactions because it does not incorporate the physics of general relativity, such as gravitation and dark energy[36]. The theory does not contain any viable dark matter particle that possesses all of the required properties deduced from observational cosmology. It also does not correctly account for neutrino oscillations (and their non-zero masses). Although the standard model is theoretically self-consistent, it has several unnatural properties giving rise to puzzles like the strong CP problem and the hierarchy problem.

Nevertheless, the standard model is important to theoretical and experimental particle physicists alike[36]. For theoreticians, the standard model is a paradigm example of a quantum field theory, which exhibits a wide range of physics including spontaneous symmetry breaking, anomalies, non-perturbative behavior, etc. It is used as a basis for building more exotic models which incorporate hypothetical particles, extra dimensions and elaborate symmetries (such as supersymmetry) in an attempt to explain experimental results at variance with the standard model such as the existence of dark matter and neutrino oscillations. In turn, the experimenters have incorporated the standard model into simulators to help search for new physics beyond the standard model from relatively uninteresting background.

The first step towards the Standard Model was Sheldon Glashow's discovery, in 1960, of a way to combine the electromagnetic and weak interactions.[37] In 1967, Steven Weinberg and Abdus Salam incorporated the Higgs mechanism[48] into Glashow's electroweak theory, giving it its modern form.

The Higgs mechanism is believed to give rise to the masses of all the elementary particles in the Standard Model[40]. This includes the masses of the W and Z bosons, and the fermions. The Higgs mechanism is also believed to give rise to the masses of quarks and leptons.

After the neutral weak currents caused by Z boson exchange were discovered at CERN in 1973,[45] the electroweak theory became widely accepted. Glashow, Salam, and Weinberg shared the 1979 Nobel Prize in Physics for discovering the electroweak theory. The W and Z bosons were discovered experimentally in 1981, and their masses were found to be as the Standard Model predicted.

The theory of the strong interaction, to which many contributed, acquired its modern form around 1973-1974, when experiments confirmed that the hadrons were composed of fractionally charged quarks[46].

Recently, the standard model has found applications in other fields besides particle physics such as astrophysics and cosmology, in addition to nuclear physics.

At present, matter and energy are best understood in terms of the kinematics and interactions of elementary particles. To date, physics has reduced the laws governing the behavior and interaction of all known forms of matter and energy to a small set of fundamental laws and theories. A major goal of physics is to find the "common ground" that would unite all of these theories into one integrated theory of everything, of which all the other known laws would be special cases, and from which the behavior of all matter and energy could be derived[41](at least in principle).

The Standard Model groups two major extant theories, quantum electroweak and quantum chromodynamics, into an internally consistent theory that describes the interactions between all known particles in terms of quantum field theory. For a technical description of the fields and their interactions, see Standard Model (mathematical formulation)[41].

The Standard Model includes 12 elementary particles of spin -1/2 known as fermions. According to the spin-statistics theorem, fermions respect the Pauli Exclusion Principle. Each fermion has a corresponding antiparticle[30].

The fermions of the Standard Model are classified according to how they interact (or equivalently, by what charges they carry)[36]. There are six quarks (up, down, charm, strange, top, bottom), and six leptons (electron, electron neutrino, muon, muon neutrino, tau (particle), tau neutrino). Pairs from each classification are grouped together to form a generation, with corresponding particles exhibiting similar physical behavior[see figure 1.1].

The defining property of the quarks is that they carry color charge, and hence, interact to the strong interaction. A phenomenon called color confinement results in quarks being perpetually (or at least since very soon after the start of the big bang) bound to one another, forming color-neutral composite particles (hadrons) containing either a quark and an antiquark (mesons) or three quarks (baryons). The familiar proton and the neutron are the two baryons having the smallest mass. Quarks also carry electric charge and weak isospin. Hence they interact with other fermions both electromagnetically and via the weak nuclear interaction.

The remaining six fermions do not carry color charge and are called leptons[30]. The three neutrinos do not carry electric charge either, so their motion is directly influenced only by the weak nuclear force, which makes them notoriously difficult to detect. However, by virtue of carrying an electric charge, the electron, muon, and tau all interact electromagnetically[27].

Each member of a generation has greater mass than the corresponding particles of lower generations[36]. The first generation charged particles do not decay; hence all ordinary (baryonic) matter is made of such particles. Specifically, all atoms consist of electrons orbiting atomic nuclei ultimately constituted of up and down quarks. Second and third generations charged particles, on the other hand, decay with very short half lives, and are observed only in very high-energy environments. Neutrinos of all generations also do not decay, and pervade the universe, but rarely interact with baryonic matter.

Interactions in physics are the ways that particles influence other particles[31]. At a macro level, electromagnetism allows particles to interact with one another via electric and magnetic fields, and gravitation allows particles with mass to attract one another in accordance with Einstein′s General Relativity[31].

The standard model explains such forces as resulting from matter particles exchanging other particles, known as force mediating particles (Strictly speaking, this is only so if interpreting literally what is actually an approximation method known as perturbation theory, as opposed to the exact theory)[31]. When a force mediating particle is exchanged, at a macro level the effect is equivalent to a force influencing both of them, and the particle is therefore said to have mediated (i.e., been the agent of) that force. The Feynman-diagram calculations, which are a graphical form of the perturbation theory approximation, invoke force mediating particles and when applied to analyze high-energy scattering experiments are in reasonable agreement with the data. Perturbation theory (and with it the concept of force mediating particle) in other situations fails[31]. These include low energy QCD, bound states, and solitons.

The known force mediating particles described by the Standard Model also all have spin (as do matter particles), but in their case, the value of the spin is 1, meaning that all force mediating particles are bosons[36]. As a result, they do not follow the Pauli Exclusion Principle. The different types of force mediating particles are described below. Photons mediate the electromagnetic force between electrically charged particles. The photon is massless and is well-described by the theory of quantum electrodynamics.

The W^+, W^-, and Z gauge bosons mediate the weak interactions between particles of different flavors (all quarks and leptons). They are massive, with the Z being more massive than the W[31]. The weak interactions involving the W act on exclusively left-handed particles and right-handed antiparticles. Furthermore, the $W^\pm$ carry an electric charge of +1 and -1 and couple to the electromagnetic interactions. The electrically neutral Z boson interacts with both left-handed particles and antiparticles. These three gauge bosons along with the photons are grouped together which collectively mediate the electroweak interactions.

The eight gluons mediate the strong interactions between color charged particles (the quarks)[36]. Gluons are massless. The eightfold multiplicity of gluons is labeled by a combination of color and an anticolor charge (e.g., redantigreen). Because the gluon has an effective color charge, they can interact among themselves. The gluons and their interactions are described by the theory of quantum chromodynamics.

The Higgs particle is a hypothetical massive scalar elementary particle the-

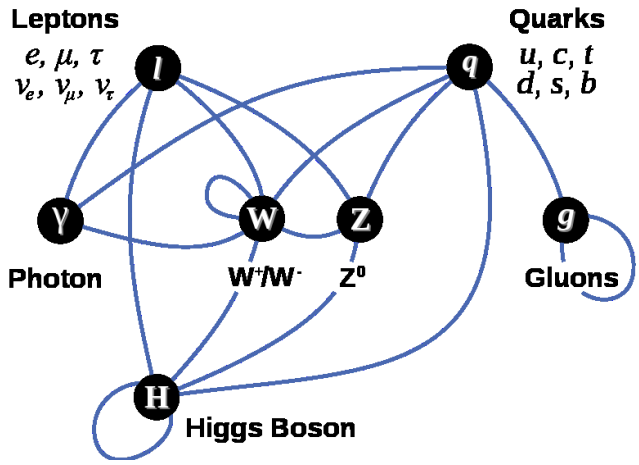

Figure 1.2: The role which Higgs boson plays in the Standard Model[48]

orized by Robert Brout, Francois Englert, Peter Higgs, Gerald Guralnik, C. R. Hagen, and Tom Kibble in 1964 (see 1964 PRL symmetry breaking papers) and is a key building block in the Standard Model.[13] It has no intrinsic spin, and for that reason is classified as a boson (like the force mediating particles, which have integer spin). Because an exceptionally large amount of energy and beam luminosity are theoretically required to observe a Higgs boson in high energy colliders, it is the only fundamental particle predicted by the Standard Model that has yet to be observed[48].

The Higgs boson plays a unique role in the Standard Model, by explaining why the other elementary particles, the photon and gluon excepted, are massive[31]. In particular, the Higgs boson would explain why the photon has no mass, while the W and Z bosons are very heavy. Elementary particle masses, and the differences between electromagnetism (mediated by the photon) and the weak force (mediated by the W and Z bosons), are critical to many aspects of the structure of microscopic (and hence macroscopic) matter. In electroweak theory, the Higgs boson generates the masses of the leptons (electron, muon, and tau) and quarks.

Maybe the Large Hadron Collider at CERN will confirm the existence of this particle. It is also possible that the Higgs boson may already have been produced but overlooked.

1.1.2 Quark Model

In physics, the quark model is a classification scheme for hadrons in terms of their valence quarks-the quarks and antiquarks which give rise to the quantum numbers of the hadrons[34].

The quark model was originally just a very good classification scheme to organize the depressingly large number of hadrons that were being discovered starting in the 1950's and continuing through the 1960's, received experimental verification beginning in the late 1960's and continuing to the present[34].

These quantum numbers are labels identifying the hadrons, and are of two kinds. One set comes from the Poincare symmetry J^{PC}, where J, P and C stand for the total angular momentum, parity and charge conjugation[34]. The remainder are flavour quantum numbers such as the isospin, strangeness, charm, and so on. The quark model is the follow-up to the Eightfold Way classification scheme.

All quarks are assigned a baryon number of 1/3[35]. Up, charm and top quarks have an electric charge of +2/3, while the down, strange, and bottom quarks have an electric charge of -1/3. Antiquarks have the opposite quantum numbers. Quarks are also spin 1/2 particles, meaning they are fermions. Mesons are made of a valence quark-antiquark pair (thus have a baryon number of 0), while baryons are made of three quarks (thus have a baryon number of 1)[34].

In particle physics, color charge is a property of quarks and gluons that is related to the particles' strong interactions in the theory of quantum chromodynamics[4]. Colour quantum numbers have been used from the beginning. However, colour was discovered as a consequence of this classification when it was realized that the spin S = 3/2 baryon, the Δ^{++} required three up quarks with parallel spins and vanishing orbital angular momentum, and therefore could not have an antisymmetric wavefunction unless there was a hidden quantum number (due to the Pauli exclusion principle)[39]. Oscar Greenberg noted this problem in 1964, suggesting that quarks should be para-fermions. Six months later Moo-Young Han and Yoichiro Nambu suggested the existence of three triplets of quarks to solve this problem[43].

While the quark model is derivable from the theory of quantum chromodynamics, the structure of hadrons is more complicated than this model

reveals[43].

1.2 Meson World and Resonances

1.2.1 Meson Characteristics

Normal(no-exotic) mesons are bound states of a quark (q) and an antiquark ($\bar{q}$). Each of the two quarks has a spin of s = 1/2 so overall the system can have a total spin of S = 0 or S = 1[32]. The vector sum of total spin and orbital angular momentum L define the total angular momentum J of the $q\bar{q}$ system. In addition to that one could get radial excitations supplement the ground state. Using the preceding characteristics, mesons are classified in the following way[11]:

Type	J	P	S	L	names
Pseudoscalar Meson	0	-	0	0	π, K, η, $\eta^{'}$
Scalar Meson	0	+	1	1	a_0, K_0^*, f_0, $f_0^{'}$
Vector Meson	1	-	1	0	ρ, K^*, ω, ϕ
Pseudovector Meson	1	+	1	1	a_1, K_{1A}, f_1, $f_1^{'}$
Pseudovector Meson	1	+	0	1	b_1, K_{1B}, h_1, $h_1^{'}$

Table 1.1: Types of mesons and quantum numbers for the lowest lying states[11]. Here J, P and S stand for the total angular momentum, parity and total spin. The L is the orbital angular momentum between quarks.

Flavourless mesons consist of a quark and an antiquark (same flavour)[3], flavoured mesons are made of quarks and antiquarks of different flavours.

In particle physics we distinguish between C-Parity (charge conjugation) and G-Parity. C-Parity is only defined for mesons that are their own antiparticle. G-Parity is a generalization of the C-parity[11].

Strictly speaking C is only a good quantum number for neutral mesons[33](like π^0), however, for charged ones made up from u and d quarks only it can be defined through the neutral component of the corresponding isospin multiplet. More precisely the G-parity is introduced as a charge conjugation operation followed by a rotation in isospin space about the y axis. Both isospin I(additive quantum number) and G-parity(multiplicative quantum number)

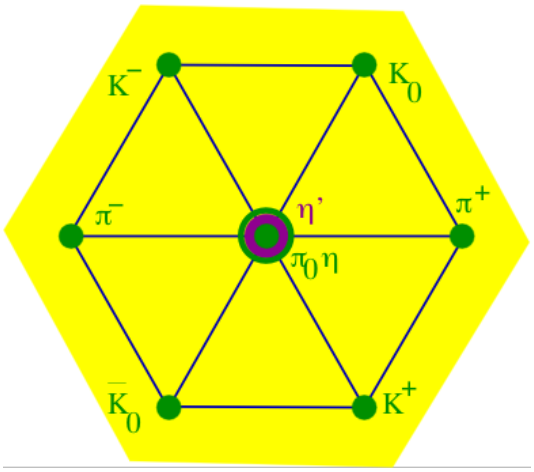

Figure 1.3: The pseudoscalar meson nonet. Members of the octet are shown in green, the singlet in magenta. The name of the Eightfold Way derives from this classification[35].

are conserved in strong interactions and, in the $q\bar{q}$ model, the following relations hold[32]:

$$P = (-1)^{L+1} \tag{1.1}$$

$$C = (-1)^{L+S} \tag{1.2}$$

$$G = (-1)^I C = (-1)^{L+S+I}. \tag{1.3}$$

The members of different nonets differ in the relative spin orientation of the constituent quarks and their relative orbital angular momentum. The members of the same group differ in their isospin and strangeness. The nonets(see figure 1.3) are classified by their meson-spin J, P-parity and C-parity.

Well known mesons with the classification L=0, J=0, P=-1 and spin S=0 are called pseudoscalar mesons(e.g. figure 1.3). Lightest mesons weakly decay into lepton pairs or electromagnetically decay into two photons[11]. They decay into hadrons by virtue of the strong interaction, if their mass is high enough.

Mesons which have a spin S=1 (parallel quark spin) and L=0, J=1, P=-1 and C=-1 are called vector mesons(see table 1.1). They have a higher mass

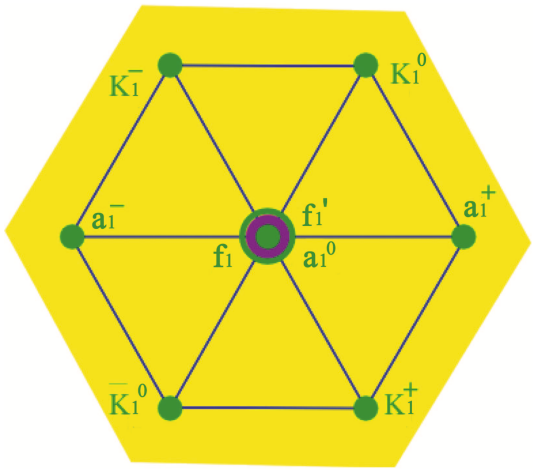

Figure 1.4: The pseudovector meson nonet. The K_1 meson observed are $K_1(1270)$ and $K_1(1400)$. They are mixtures of the quark model states with J^{PC}= 1^{++} and 1^{+-}.

than the pseudoscalar mesons (the lowest lying state). Vector mesons dominantly decay due to the strong interaction, with a short average lifetime[32].

Mesons which have a spin S=0 or 1 (parallel quark spin) and L=1, J=1, P=+1 and C=+1 are called pseudovector mesons(see figure 1.4). The pseudovector mesons have the same P as scalar mesons and have the same J=1 as vector mesons(see table 1.1)

From equations 1.1-1.3, it is apparent that J^{PC} quantum numbers like 0^{+-}, 1^{-+} , 2^{+-}, are not accessible in $q\bar{q}$ systems[63]. The firm establishment of such spin-exotic states would be a direct hint for the existence of objects with either gluonic excitations or more than two quarks involved[47]. In that context hybrids[51], glueballs or tetraquarks are mostly discussed, which are in general referred to as exotics[55]. This should not be confused with spin-exotics, because also a hybrid for example can have normal quantum numbers allowed for any $q\bar{q}$ system. This brings up a general feature of mesons, namely that those with identical external quantum numbers can mix, even if they have a different internal flavor structure[52]. In fact many of the physically observed particles like the η have uu, dd and even ss components. This composes a big challenge for the detection of exotics with normal quantum numbers since they would most likely mix with ordinary $q\bar{q}$ states and it is extremely difficult to prove this small admixture. Thus it is much more encouraging to look for

spin-exotic states[63].

1.2.2 Resonances

Particles with a long lifetime can easily be seen by track detectors or bubble chambers. Particles having a very short lifetime decay rapidly into different particles. It is not possible to detect them directly but to reconstruct them from their decay products. These decaying particles are called "resonances". Resonances can be produced in two different types of experiments[11]:

1) In a "resonance formation" two particles collide and generate a resonance as an intermediate state of the incoming and outgoing particle.

2) At a "resonance production" we infer the presence of a resonance when the invariant energy of the two or more outgoing particles has a favoured value.

It is difficult to find resonances in this manner because one needs to examine all combinations of outgoing particles and assign their energies (invariant masses) to see if there is an enhancement. High-energy experiments allow to generate new particles and one can check whether they originate from resonances yet unknown. The mass of an absolutely stable particle is well defined. A less stable particle always has a blurred value of mass which can be explained by the uncertainty principle[11].

In this thesis the mass dependence of the production amplitude of a resonance is usually parameterized by means of a relativistic Breit-Wigner (BW) function[63],

$$BW(m, M_0, \Gamma_0) \sim \frac{1}{M_0^2 - m^2 - iM_0\Gamma_T(m)} \tag{1.4}$$

where M_0 and Γ_0 are the mass and width of the resonance, respectively. This formula takes a mass dependent total width into account.

$$\Gamma_T(m) = \sum_n \Gamma_{0n} \frac{M_0}{m} \frac{q_n}{q_{0n}} \frac{F_{Ln}^2(q_n)}{F_{Ln}^2(q_{0n})} \tag{1.5}$$

with $\Gamma_0 = \Gamma_T(M_0)$, which represents a sum over all possible decay channels n (partial width Γ_{0n}) of the resonance. Here q_n denotes the break-up momentum of the particular (two-body) decay 3 and $q_{0n} = q_n(M_0)$. The functions F_{Ln} are the so-called Blatt-Weisskopf barrier factors, which are connected to the

spherical Hankel functions[63]. From those they carry over an asymptotic behavior when q_n approaches the threshold defined by the mass of the decay particles, which can effect the resonance shape.

1.3 Partial Wave Introduction

In the 90s of the last century high statistics experiments have lead to a better insight in the spectrum of hadrons[57]. In particular the finding of crypto-exotic and J^{PC} exotic states tremendously improved the experimental situation in meson spectroscopy. All this was possible only with sophisticated analysis methods like the decomposition of measured phase-space distribution into partial waves and to express the partial waves in terms of complicated dynamical functions[57].

The basic task is to find all resonances, with their static properties like mass, width, spin and parities[57]. This is a very demanding task, since a lot of resonances overlap. In addition complicated production processes or scattering with many waves in the intermediate state complicate the situation[50].

Before we want to begin the partial wave analysis, first of all we should learn the kinematics and two-body reactions at least.

1.3.1 Kinematics

Center of mass and laboratory system

In the collision of two particles of masses m_1 and m_2, the total center of mass energy $\sqrt{s} = E_{cm}$ can be expressed by the Lorentz-invariant form[26]:

$$\sqrt{s} = E_{cm} = ((E_1 + E_2)^2 - (\vec{p_1} + \vec{p_2})^2)^{1/2} \tag{1.6}$$

Here E_1 and E_2 are the energies of two particles. The particle of mass m_1 has energy E_1 and 3-momentum $\vec{p_1}$. Together E_1 and $\vec{p_1}$ are a 4-vector $p_1 = (E_1, \vec{p_1})$. So the $p_1^2 = (E_1, \vec{p_1})(E_1, -\vec{p_1}) = E_1^2 - |\vec{p_1}|^2 = m_1^2$ and $E_2^2 - |\vec{p_2}|^2 = m_2^2$.

From formula 1.6 one derives:

$$E_{cm} = [m_1^2 + m_2^2 + 2E_1E_2(1 - \beta_1\beta_2 \cos\theta)]^{1/2} \tag{1.7}$$

where θ is the angle between two particles(particle 1 and particle 2). β is the velocity of the particle where $\beta_1 = |\vec{p_1}|/E_1$ and $\beta_2 = |\vec{p_2}|/E_2$. In the laboratory

frame where one particle (of mass m_2) is at the rest (laboratory frame)[26]. β_2=0 one obtain:

$$E_{cm} = [m_1^2 + m_2^2 + 2E_{1lab}m_2]^{1/2} \tag{1.8}$$

The velocity of the center of mass in the lab system is

$$\beta_{cm} = |\vec{p}_{lab}|/(E_{1lab} + m_2) \tag{1.9}$$

The $\vec{p}_{lab}$ is the 3-momentum $\vec{p}$ in laboratory system. Here the $\vec{p}_{lab} \equiv \vec{p}_{1lab}$.

Two-body reactions

Two particles of momenta (4-vector) p_1 and p_2, masses m_1 and m_2, energy E_1 and E_2 scatter to particles of momenta (4-vector) p_3 and p_4, masses m_3 and m_4, energy E_3 and E_4; the $\vec{p_i}$ are the 3-momenta. The Lorentz-invariant variables are defined by[28]. Here the s correspond to the squared c.m. energy E_{cm}^2 in formula 1.6

$$s = (p_1 + p_2)^2 = (p_3 + p_4)^2 = m_1^2 + 2E_1E_2 - 2\vec{p_1}\vec{p_2} + m_2^2 \tag{1.10}$$

$$t = (p_1 - p_3)^2 = (p_2 - p_4)^2 = m_1^2 - 2E_1E_3 + 2\vec{p_1}\vec{p_3} + m_3^2 \tag{1.11}$$

$$u = (p_1 - p_4)^2 = (p_2 - p_3)^2 = m_1^2 - 2E_1E_4 + 2\vec{p_1}\vec{p_4} + m_4^2 \tag{1.12}$$

And they satisfy

$$s + t + u = m_1^2 + m_2^2 + m_3^2 + m_4^2 \tag{1.13}$$

In the center of mass system[28]:

$$t = (E_{1cm} - E_{3cm})^2 - (p_{1cm} - p_{3cm})^2 - 4|p_{1cm}p_{3cm}|sin^2(\theta_{cm}/2) \tag{1.14}$$

Here p_{cm} are absolute values of the 3-momenta in the center of mass system. The θ_{cm} is the angle between particle 1 and particle 3 in the center of mass system.

$$t = t_0 - 4|\vec{p}_{1cm}||\vec{p}_{3cm}|sin^2(\theta_{cm}/2) \tag{1.15}$$

where θ_{cm} is between particle 1(In) and particle 3(Out) in the center of mass system. The limiting values $t_0(\theta_{cm} = 0)$ and $t_1(\theta_{cm} = \pi)$ for $2 \to 2$ scattering are:

$$t_0 = [(m_1^2 - m_3^2 - m_2^2 + m_4^2)/2s^{-1/2}]^2 - (p_{1cm} - p_{3cm})^2 \tag{1.16}$$

and

$$t_1 = [(m_1^2 - m_3^2 - m_2^2 + m_4^2)/2s^{-1/2}]^2 - (p_{1cm} + p_{3cm})^2 \tag{1.17}$$

In the literature the notation $t_{min}(t_{max})$ for $t_0(t_1)$ is sometimes used, which should be discouraged since $t_0 > t_1$. The energies and momenta of the incoming particles in the center-of-mass reference system are[28]:

$$E_{1cm} = (s + m_1^2 - m_2^2)/2s^{1/2} \tag{1.18}$$

Here E_{1cm} is the energy of particle 1 in the center of mass system. s is defined in formula 1.10.

$$E_{2cm} = (s + m_2^2 - m_1^2)/2s^{1/2} \tag{1.19}$$

Here E_{2cm} is the energy of particle 2 in the center of mass system. For E_{3cm} and E_{4cm}, change m_1 to m_3 and m_2 to m_4. Then

$$p_{icm} = [E_{icm}^2 - m_i^2]^{1/2} \tag{1.20}$$

and

$$p_{1cm} = p_{1lab} m_2 / s^{1/2} \tag{1.21}$$

Here the subscript laboratory refers to the frame where particle 2 is at rest[28]. The p_{icm} is the absolute value of the 3-momenta p of particle i(1 to 4) in the center of mass system. The E_{icm} is the energy of particle i(1 to 4) in the center of mass system. The m_i is the mass of particle i(1 to 4). The p_{lab} is the absolute values of the 3-momenta p in laboratory system.

1.3.2 Diffractive dissociation

Diffractive scattering is studied at Compass using π^- beam, proton target and can be used for the production of exotic particles. The decay products of the resonances can be analyzed with the help of the spectrometer[11].

The incoming pion scatters off the target and gets excited to some state X. Then X decays into $\pi^- f_1$ and f_1 decays to $\pi^-\pi^+\eta$. Thus X=$\pi^-\pi^-\pi^+\eta$ in the case of the analysis presented in this thesis and the reaction studied is symbolically written as: $\pi^- + p \to X + p \to \pi^-\pi^-\pi^+\eta p$.

In the diffractive scattering process a direct excitation of the beam particle occurs by the exchange of a reggeon to a resonance[63]. At the excitation a

momentum t is transferred to the target proton. Mesons are mainly produced in diffractive processes. The meson production from pion disscociation is a method to produce hadrons with the same internal quantum numbers as a pion. Hybrids can also be produced, like the pseudovector mesons with the exotic quantum number $J^{PC} = 1^{-+}$. Three of these resonances were reported by the VES and E852 experiment: $\pi_1(1400)$, $\pi_1(1600)$ and $\pi_1(2000)$[11].

At elastic vertices, a particular reggeon plays a dominant role, the so called pomeron($\mathbb{P}$). The real nature of the pomeron is perhaps not entirely understood but experiments and theoretical predictions have shown that it should be a gluonic object as only momentum and angular momentum is exchanged[11].

The squared four-momentum transfer t of a diffractive reaction can be assigned by measuring the momenta of the involved particles:

$$t = (p_\pi - p_X)^2 = (E_\pi - E_X)^2 - (\vec{p}_\pi - \vec{p}_X)^2 \tag{1.22}$$

The four-momentum-vectors of the incoming particle (p) and the produced particle or resonance (X), are described by p_π and p_X. The energy of π and X are defined by E_π and E_X. $\vec{p_\pi}$ and $\vec{p_X}$ stands for the three-momentum-vectors of the incoming particle and the produced particle or resonance. The recoiling nucleon remains intact, while the incoming particle is excited[11]. However, in one event the same t applies to the proton vertex t=$(P_p - P_{rec})^2$= $(m_p - E_{rec})^2 - \vec{p}^2_{rec} \approx -|\vec{p}_{rec}|^2$ The resonance or particle X which is produced in this reaction, subsequently decays into lighter particles and can be reconstructed from its decay products.

1.3.3 Isobar Model and Decay amplitude

Before we want to write down a decay amplitude using a particular spin formalism, it has to be defined how the final state particles are grouped to construct the decay chain. The most popular approach is the isobar model. In this model it is assumed that not only the primary interaction $\pi^- p \to Xp$ leads to a two-body final state but also all subsequent decays of X appear to be two-body decays[63]. For the case of $\pi^-\pi^-\pi^+\eta$ final states, the produced state X can decay into f_1(also referred to as isobar) and a bachelor π^-. Then f_1 decays to either the isobar $a_0^\pm$ and bachelor $\pi^\mp$ or the isobar called $(\pi^-\pi^+)_S$ and bachelor η. In general, the isobar model has been found to work extremely well in very different environments and for most of the known hadrons[63]. Exceptions may of course be direct decays in more than two particles or decay

chains involving rescattering processes of the final state particles.

The full description of the state X will be shown in section 7.1 which includes J, M(the total spin projection) and ϵ(the reflectivity basis) also its parity P and charge conjugation C.

The amplitude of X decay into the final states $\pi^- f_1$ has the same structure as the amplitude describing the decay of f_1 into its childrens. The total amplitude is the product of the amplitudes describing each step of the chain, where each step is a two-body decay in the isobar model.

The initial decay of the X into its children is evaluated in the Gottfried-Jackson frame. This frame is a rest frame of the resonance X with the z axis in the direction of the beam and the y axis perpendicular to the production plane. As for general case the state X has spin J with z projection M. It decays into two children x_1 and x_2 with helicity λ_1 and λ_2. These children have a breakup momentum $\vec{p}$ and relative orbital angular momentum L. The decay amplitude can be written as:

$$A_X = (2L+1)^{1/2} \sum_{\lambda} D^{J*}_{M\lambda}(\Omega_G)(L0s\lambda|J\lambda)(s_{x_1}\lambda_{x_1}s_{x_2} - \lambda_{x_2}|s\lambda)F_L(p)a_{Ls}A_{x_1}A_{x_2} \tag{1.23}$$

Where the total spin $s = s_{x_1} + s_{x_2}$ and $\lambda = \lambda_{x_1}$ - λ_{x_2} is the component of s in the direction defined by x_1 and x_2's momentum helicity frame. The A_{x_1} is the decay amplitude of x_1 and the A_{x_2} is the decay amplitude of x_2. $\tau = (\theta_G, \phi_G, \theta_H, \phi_H, m_{x_1})$. The $\sqrt{2L+1}$ factor which along with the two Clebsch-Gordon coefficients come from the fact that we are using helicity states and must relate the helicity coupling constant to the Ls-coupling constant.

$F_L(p)$ where p= $|\vec{p}|$ is an angular momentum barrier factor added to give the amplitude the correct behavior near threshold. The a_{Ls} depending on the m_X is the Ls coupling constant which contains the dynamics of the decay.

Rotational properties of the helicity states lead to the D-function $D^{J*}_{M\lambda}(\Omega_G)$. Here $\Omega_G = (\theta, \phi, 0)$ are the Euler angles of x_1 in the Gottfried-Jackson frame. The choice of $\gamma = 0$ means the third angle γ defines the phase convention.

In our case, the state X decays to π^- and f_1. Here π^- with spin s_1 =0 and helicity λ_1=0, f_1 with spin s_2 =1 and helicity λ_2=0, $\pm$1. This decay amplitude

will then be used in section 7.3.

Chapter 2

The COMPASS Experiment

COMPASS(Common Muon Proton Apparatus for Structure and Spectroscopy) is one of the fixed target experiments at CERN. In COMPASS there are more than 300 physicists from 26 institutions all over the world, they have the same aim which is know more about the hadron structure. The COMPASS spectrometer comprises several types of tracking detectors, hadronic and electromagnetic calorimeters, RICH detector and muon filters[24]. It is a two-stage spectrometer consisting of a small angle (0 - 30 mrad) and a large angle part (30 - 180 mrad).

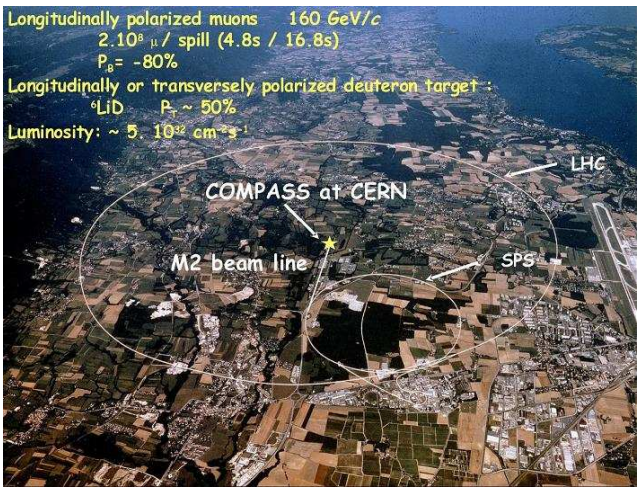

Figure 2.1: Location of the COMPASS experiment at CERN[22]

The COMPASS spectrometer was assembled in 1999-2000 and commissioned during a technical run in 2001. The first data taking period started in

summer 2002 and ended in fall 2004. The experiment had its first shut down in 2005 for repairs, refits and new installations. The years 2006 and 2007 were dedicated to the muon run, 2008 and 2009 to the hadron programme. In 2010 a polarized proton was used again to study structure functions[63].

2.1 COMPASS Setup

The construction of the spectrometer is shown in figure 2.2[14].

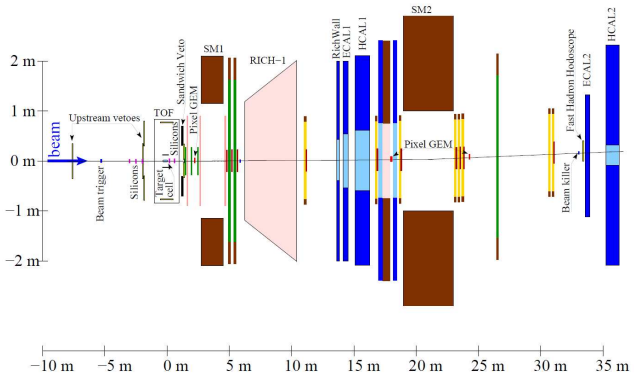

Figure 2.2: Schematic design of the spectrometer[14]

The figure 2.2 provides an overview of the 2-stage COMPASS spectrometer indicating important parts. The target was surrounded by a Recoil Proton Detector (RPD) measuring the signature of diffractive processes, the recoil proton. The final states, neutral and charged, of decaying resonances excited in the target were identified and measured by the spectrometer behind the target. The principle of a spectrometer is bending of charged particle tracks by dipole magnets in order to measure their momentum with high accuracy and acceptance over a wide momentum range.

To do so the spectrometer was built up in two stages. The first Spectrometer Magnet (SM1) is a 110cm long dipole and it was located about 4m downstream the target. The field integral is about 1Tm and the angular acceptance of ±180 mrad defined the required detector acceptance in the first stage in the horizontal plane. The first stage, which is also called Large Angle Spectrometer (LAS), featured besides various tracking detectors also a charged final state PID with the Ring Imaging Cherencov (RICH) detector, the first

electromagnetic calorimeter (ECAL1) for neutral state identification, the first hadronic calorimeter (HCAL1) and the first muon wall (MW1) for muon identification. A momentum range starting from below 1 GeV/c up to about 60 GeV/c was covered by this stage[63].

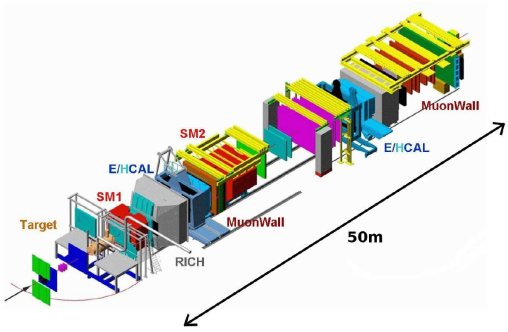

Figure 2.3: Artistic view of COMPASS[20]

Particles higher in momenta than 60 GeV/c were passing the second Spectrometer Magnet (SM2). Its field integral of 4.4Tm deflected charged particles up to ±30 mrad and was therefore defining the required acceptance of the Small Angle Spectrometer (SAS). It was featuring a similar set-up as found in the LAS apart from a RICH. It was originally foreseen to place also one RICH in the second stage but has not been realized yet mostly due to financial reasons.

2.1.1 Target Region

With the different requirements of different experiments, the COMPASS target has to satisfy different conditions. The hadron beam consists of different particles: The beam, which was used for this thesis consists of pions with some kaons and antiproton contaminations (negative hadron beam). Fast Cherenkov counters are used to identify the incoming particles in such a mixed beam[63].

Depending on the individual experimental requirements a proton or lead target can be used. The target is surrounded by a recoil proton detector(RPD), which comprises two rings that are made of scintillating material. Two stations of silicon microstrip detectors in front of and behind the target, with a

high spatial resolution and a good resistance against high fluxes, are used to measure the angle between the incoming and outgoing beam[11].

2.1.2 Recoil Proton Detector

The mission of Recoil Proton Detector is to collect protons coming from the target, detect and reconstruct their momentum. The detector consists of two cylinders, each consisting of several scintillator strips[49]. The inner cylinder has a distance of 120 mm from the steel shaft. The two rings in the beam direction are asymmetrically aligned to the target, the forward movement of the recoil protons are be considered. The scintillators cover an angle of 55° to 90°[5].

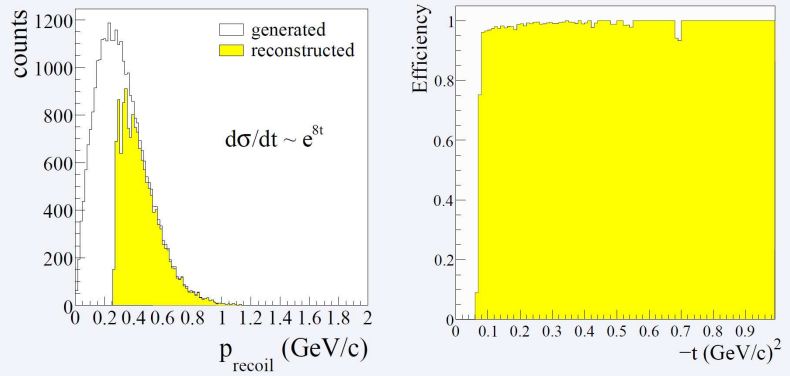

Figure 2.4: Acceptance range of Recoil-Proton-Detector[5]

2.1.3 Tracking Detectors

Tracking detectors measure the 3D positions of charged particles as they travel through it, usually in a magnetic field, accordingly to allow measurement of their momentum[17]. The tracking system at COMPASS is used to cope with the expected particle flux in the different positions along the whole spectrometer. Along the beam and very close to the target the used detectors must unify two important factors. A high particle rate capability (up to a few MHz per channel) is needed as well as a very good space resolution ($100\mu m$ and better)[11]. The beam path itself is surrounded only by some material to diminish secondary interactions of beam particles and to minimize multiple scattering effects. Many tracking stations are arranged alongside the

spectrometer. Each station consists of a set of detectors of the same type at approximately the same z-coordinate along the beam. According to their different requirements these stations are installed at different locations of the spectrometer:

VSAT(Very Small Area Tracking):
With the help of the BMS(beam momentum station) it is possible to determine the momentum of the incoming muons on an event-by-event basis[11]. At a radial distance of 2.5-3cm, the beam region is covered by eight scintillating fiber hodoscopes which ensure the tracking of incoming and scattered beam particles as well as the detection of all other reaction products arising near the beam. For the hadron beam the BMS can not be used. Too many interactions of the beam would take place in the BMS.

The COMPASS silicon microstrip detectors are situated upstream of the target and used to detect incoming muons in the muon programme and for track and vertex reconstructions of hadron particles. The beam divergence is taken into account by using various sizes of these microstrip detectors[11].

SAT(Small Area Tracking):
For distances larger than 3cm from the beam, 12 Micromegas detectors (Micromesh Gaseous Structure), assembled in 3 stations and 11 GEMs (Gas Electron Multipliers) cover the region from the upstream side of the SM1 magnet to the end of the spectrometer[11].

The Micromegas detector has a two parallel electrode structure and a set of microstrips for readout at the bottom. When a particle passes through the conversion area it comes to an ionisation. The produced primary electrons drift into a moderate field. An avalanche is then produced in the amplication gap. The resulting electron pairs can now be detected by the strips. The mesh is used to separate the two gaps and to avoid the reflux of produced ions to the conversion gap. GEM detectors are built of 3 copper plated foils instead of one mesh. These detectors ensure a high space resolution($< 100\mu m$) with a low radiation length in the small area region[11].

LAT(Large Area Tracking):
The large angle tracking system consists of planar drift and straw tube chambers. These are gas detectors with anode wires of different types[11]. The MWPCs (Multiwire Proportional Counters) are installed along the entire spectrometer. These counters are able to amplify single photoelectrons and detect

them.

2.1.4 RICH Detector

The RICH Detector, located in the first spectrometer (RICH-1), is needed for hadron identification[11]. It separates hadrons into kaons, pions and protons, according to their momenta. The RICH-1 is a large-size Cherenkov Counter and works in the domain of 5 GeV/c to 80 GeV/c.

Therefore, it covers the whole angular acceptance of COMPASS LAS[11]. The working principle is based on the emission of Cherenkov photons in C_4F_{10} radiator gas and their subsequent reflection by two spherical mirrors. These photons are dissipated to electrons by the CsI photocathodes of 8 MWPCs and finally detected by the latter.

2.1.5 Electromagnetic Calorimeters

An electromagnetic calorimeter is a detector which determines the energy of electrons, positrons and photons[11]. The COMPASS spectrometer contains two electromagnetic calorimeters ECAL1 and ECAL2. ECAL1 is directly installed in front of HCAL1, ECAL2 in front of HCAL2. Hadrons only lose a small amount of their energy due to electromagnetic interactions. Therefore, hadrons are likely to be detected in the proximate HCALs. Electromagnetic Calorimeters with good performances are needed for the COMPASS hadron program and for the studies of GPDs.

The $\gamma\gamma$ of a decaying π^0 or η are detected in the two electromagnetic calorimeters ECAL1 and ECAL2. Neutral pions are reconstructed from neutral clusters in the calorimeters, as it was described(more details see[11], page 79).

2.2 Hadron beam

The COMPASS hall is connected to the SPS by means of a 600m long beam line. At its beginning, the intense primary proton beam impinges on a beryllium production target with a thickness of 500mm. From the produced par-

ticles, secondary hadrons (mainly pions) up to 280 GeV/c can be selected by tuning a series of focussing and bending magnets.

Here we show the overview of the CERN accelerator facility where we can know the role of SPS in CERN.

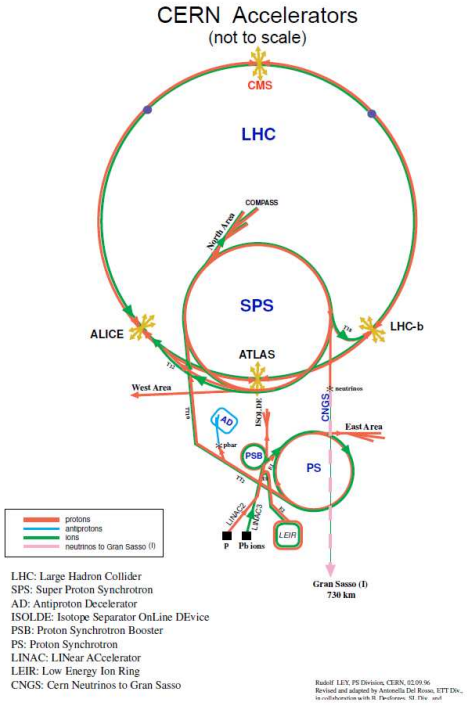

Figure 2.5: The role of SPS which provides the beam for COMPASS can be seen from the overview of the CERN accelerator facility. The COMPASS spectrometer is located at the north area of the SPS.[63]

The beam consisted mainly of charged pions, kaons and (anti)protons when running in hadron mode. Both, positive or negative charges could be selected. The choice of the charge had direct impact on the beam composition. The composition depends also on the selected beam momentum.

In the positive hadron beam, protons were dominant with a large contributions of pions. While protons dominated as they are produced as leading particles from the primary beam, anti-protons require a pair production process and are thus a minor component in the negatively charged hadron beam.

There mostly pions were found. In both cases kaons were just a small component of several percent[20].

2.3 Sandwich Veto Detector

The Sandwich Veto Detector(SVD) vetoes an event when one of the particles has a large angle($> 11°C$) with larger than the acceptance of the LAS. The SVD is a common detector for the Central Production as well as the Diffractive Dissociation that has been carried out in 2008 and 2009[64]. It is capable of detecting charged as well as neutral particles. The SVD consists of alternate layers of Pb and scintillators.

2.3.1 Role of the SVD in COMPASS

Figure 2.6 summarizes how the Sandwich Veto Detector is used in the COMPASS setup(more details will be shown in section 3.1[11]).

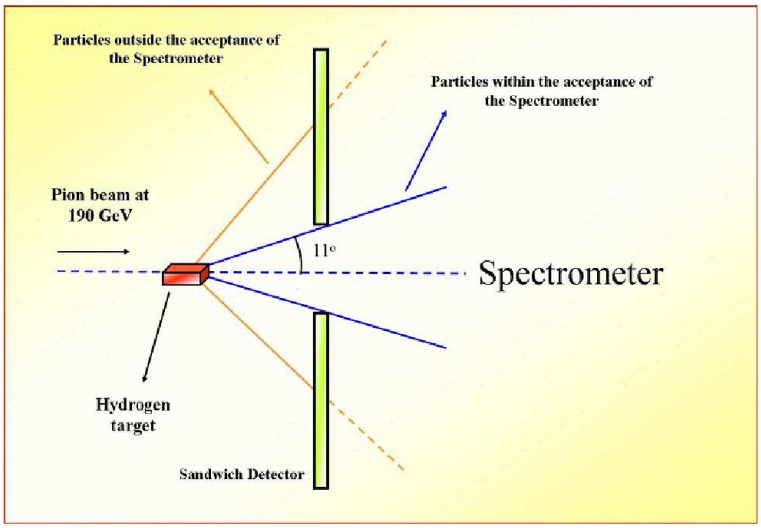

Figure 2.6: Sandwich Veto Detector in the COMPASS setup[64]

The two stage spectrometer located downstream of the target has a certain acceptance limit for particles incident on it. This acceptance limit with respect to the centre of the target is about 180 mrad. If events with particles which fall within this acceptance angle, we record or store these events. If events

with particles falling outside this acceptance angle, we prevent these from entering our Data Acquisition System[64]. Since the memory space is limited, so these events would unnecessarily eat up a lot of memory space and more importantly they would add a lot of junk to our relevant data, thus making them impure. The offline analysis of this impure data would then be a difficult job. So in order to prevent these unimportant data from entering into our memory system, we put the sandwich Veto detector in between the target and the Spectrometer which would then reject the events falling outside the acceptance angle of the spectrometer. The central hole of the Sandwich detector is allowed to make a solid angle of 192 mrad by placing the detector at a distance of 1550 mm and fixing the radius of the hole to 250 mm. The particles corresponding to our desired events (those falling within the acceptance angle of the spectrometer less than 192 mrad) are allowed to pass through the hole undisturbed. The particles corresponding to undesired events (those falling outside the acceptance angle of the spectrometer bigger than 192 mrad) are allowed to hit the Sandwich detector, which then vetoes these events (rejects these events) and prevents them from entering the data system. Thus the Sandwich detector reduces the junk from the data and thereby acts as a data purifier[11].

2.3.2 The Components of SVD

The sandwich Veto Detector is composed of Steel plates, steel base plates, air gaps and lead(Pb)/scintillator layers.

The steel plates are 1mm thick. These plates provide mechanical stability to the scintillators and the Pb plates, and keep them in proper place. The steel base plates are 8 mm thick. These are also meant for providing mechanical stability to the detector and they are also used to attach the detector to the support structure.

The role of the air gaps is to maximize internal reflections in the scintillators and thus to increase the efficiency of the detector. Air has a smaller refractive index than the scintillators, so it assists well in total internal reflection. Apart from the air gaps, a 0.1 mm specially designed paper is wrapped around the scintillators to aid reflections of the escaped light back into the scintillators.

As for the Pb/scintillator layers: The Sandwich veto is meant to detect high energy as well as neutral particles[11]. If we were concerned in detecting

only low energy electrons then the plastic scintillators alone would have served our purpose. But since we are concerned with detecting high energy electrons, photons and other charged particles, the low Z scintillators alone would not do. The reason for this is explained as follows: For high energy electrons the dominant process of energy loss is bremsstrahlung. This energy loss is proportional to Z^2. For such electrons, the photons produced by bremsstrahlung are also of very high energy, well above the threshold for electron positron pair production, so the photons will typically produce an electron positron pair, each having an average half the energy of the photon. These new particles are still very fast and may give further bremsstrahlung, leading to further pair production and so on.

The result is that an incident electron of very high energy will produce an electromagnetic shower. A similar electromagnetic shower is produced when a high energy photon is incident on a high Z material. So we see that both high energy electrons as well as photons initiate electromagnetic showers, and this process is facilitated by high Z materials. In order to meet the high Z requirements NaI scintillators can be used. But this would mean that we will need a very thick and huge piece of NaI in order to capture an appreciable amount of shower. However for a large detector, this is practically not feasible since it would be too costly. So an alternate choice is to use a passive layer (such as Pb in our case) which provides the high Z necessary for electromagnetic shower generation followed by a scintillation layer which would record the charged particle's signal. Many layers of alternate Pb and scintillator are used in order to capture a substantial amount of shower.

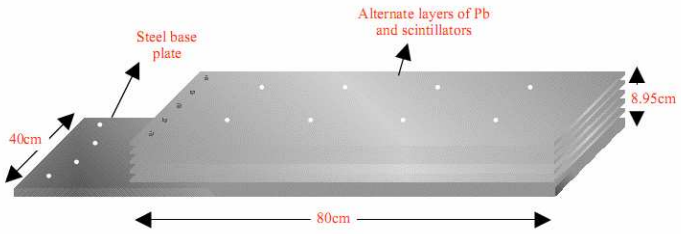

Figure 2.7: Module of Sandwich Veto Detector

The frontal active area of a module is 800*400 mm^2. The thickness of the module is 89.5 mm, which is also the thickness of the complete detector. The thickness of a module is shared among the scintillators, Pb plates, steel plates,

ground steel plate and air gaps[11] are as follows:

(a) 10 steel plates of 1 mm thickness each

(b) 1 ground steel plate of 8 mm thickness

(c) 3 layers of scintillators with 10 mm thickness each

(d) 2 layers of scintillators with 5 mm thickness each

(e) 5 Pb plates of 5 mm thickness each

(f) Air gap between the Pb plates and scintillators (of 10 mm thickness) is 1.5 mm, so for three layers a total of 4.5 mm air gap

(g) Air gap between the Pb plates and scintillators (of 5 mm thickness) is 1mm, so for two layers a total of 2 mm air gap

Fig. 2.8 shows how the thickness is divided among the various components.

Wavelength shifting optical fibres of 1 mm diameter are glued into the grooves of the scintillators(more details see[64]).

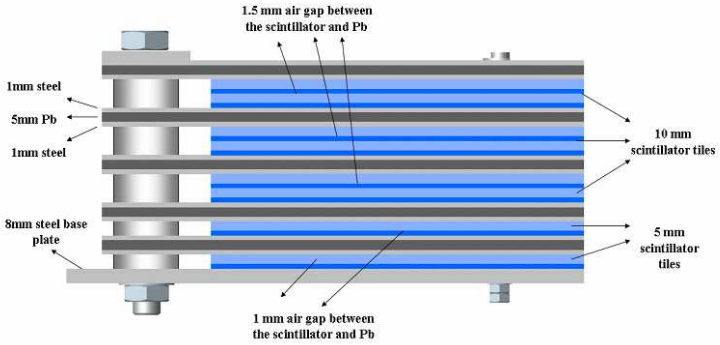

Figure 2.8: The divided thickness among the various components

The fibres hanging out from the scintillator ends are connected to PM tubes. The arrangement of the PM tubes is shown in figure 2.9.

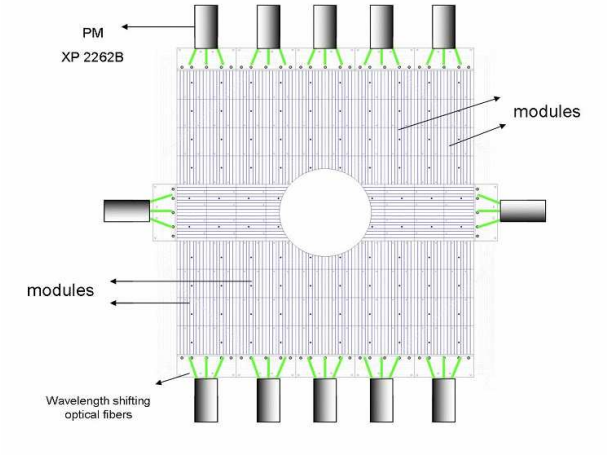

Figure 2.9: The arrangement of the PM tubes

The analog signals coming out of each PM tube are led to a discriminator and the logical signals from the discriminator are led to Time Digital Converter(TDC).

Chapter 3

Measurements with the SVD

In this chapter measurements with the Sandwich Veto Detector(SVD) are described. The goal was to determine how many photons are produced when a minimum ionizing particle(MIP) passes through. First section describes the setup of the experiment. In the second section we describe the analysis. Last but not the least, we show the efficiency of the SVD.

3.1 Experimental setup

An experiment was set up to show the efficiency of sandwich veto detector(SVD). Through the calculation we can know the properties of the SVD.

In order to know the number of photons which are produced by a minimum ionizing particle (MIP) we measure both the recorded signal and the signals of single photons, then compare with each other.

To this end, we took advantage of muons from cosmic radiation, since they have enough energy to pass through the detector, and thus their energy is only determined by the traversed detector thickness. The distribution of energy corresponds to a Landau distribution.

In this experiment we set two triggers to measure the Sandwich(PMT1 and PMT2). The PMT1 base with 2 connectors and the PMT2 base with 4 connectors. The HV of Ch0(Trigger PMT1) was 1453 V and the HV of Ch1(Trigger PMT2) was 1809 V.

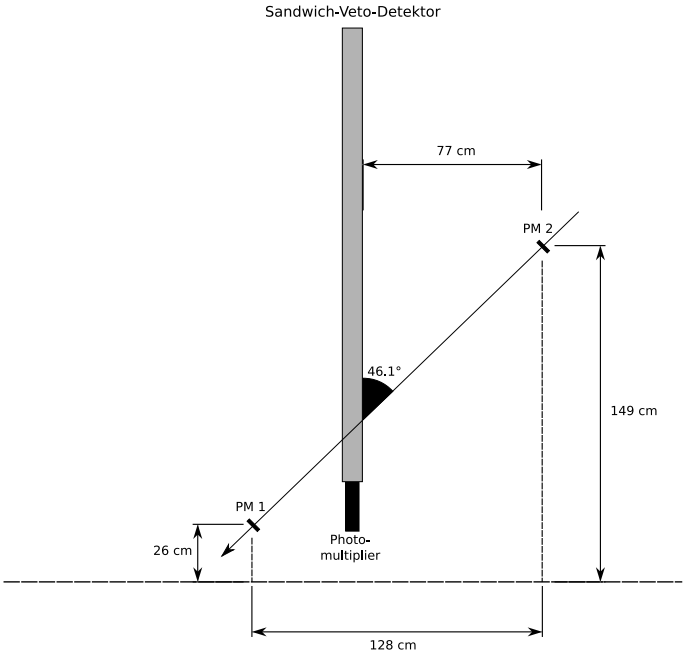

Figure 3.1: The Setup of Sandwich Measurements[64]

For the first measurement we set the angle at 45 degree.

SVD module 12: single photon @5mV, HV ch2 @1895V.

SVD module 11: single photon @5mV, HV ch3 @2054V.

The parameters value of experiment setup have been listed in the table 3.1.

	Single photo	HV	connectors
SVD module 12	5mV	1895V	ch2
SVD module 11	5mV	2045V	ch3
PM1T	/	1453V	ch0
PM2T	/	1809V	ch1

Table 3.1: The parameter value of experiment setup

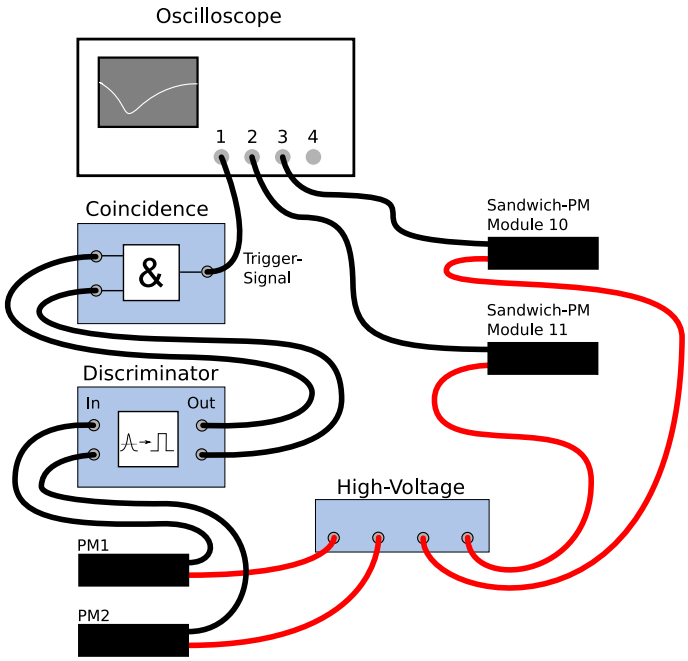

Figure 3.2: Schematic view of the experimental arrangement[64]

These two photo multipliers(PM 1 and PM 2) were each associated with a discriminator. When a signal from the photomultiplier exceeds a certain threshold value, the discriminator produces the logic signals, then these signals are sent to a coincidence unit. The coincidence was connected as a logical "and"(not "or") thereby it outputs a logic signal only when the two discriminators both send the signals. If the coincidence outputs a logic signal, it will trigger the oscilloscope to record the PM signals from the sandwich. In order to reduce the large number of spurious coincidences, the width of the discriminator output was set to 5 ns. The experiment arrangement is shown in figure 3.2[64].

3.2 Analysis

Photon signals from scintillating material can be detected and converted by wavelength shifting fibres(see page 29). The fibres are connected to the photomultiplier window, so that the light transported by the fibres hit the photocathode. The number of photoelectrons emitted from the photocathode are

multiplied in the photomultiplier.

The MIP signals were recorded for module 11 of the sandwich detector as shown in the figure 3.3.

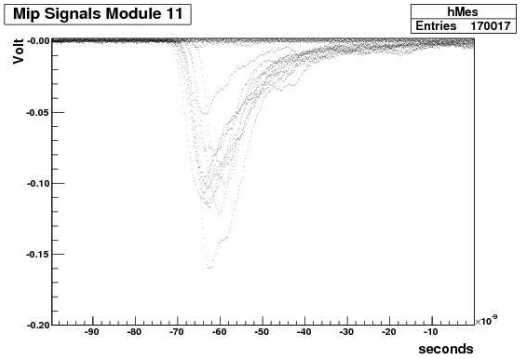

Figure 3.3: Signals from MIPs[64]

Photomultiplier signals from cosmic muons traversing the final detector assembly have average rise times $(20\% - 80\%)$ of 3.3 ns, logarithmic decay times of 9 ns, and widths at half maximum of 12 ns(see fig. 3.4). These values are larger by a factor of almost three than those obtained for single photons and they are also larger than the corresponding values for a single double layer. The differences are attributed to the statistical spread of light collection times from scintillator via wavelength shifting fibres(see page 29).

The value of MIP signals are averaged in figure 3.4.

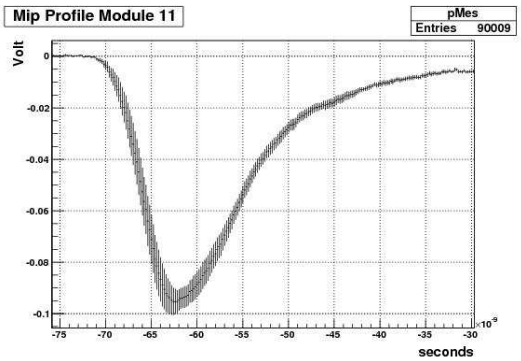

Figure 3.4: The averaged shape of the MIP signals[64]

Single photon signals are recorded for module 11 of the sandwich detector which are shown in the figure 3.5.

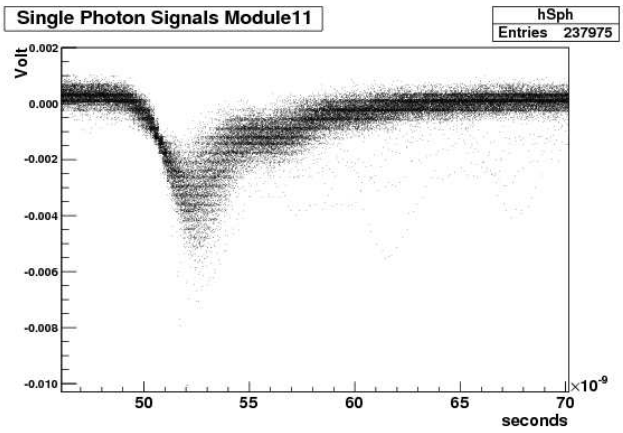

Figure 3.5: Overlay of single photon signals in module 11

The average shape for a single photon is shown in figure 3.6.

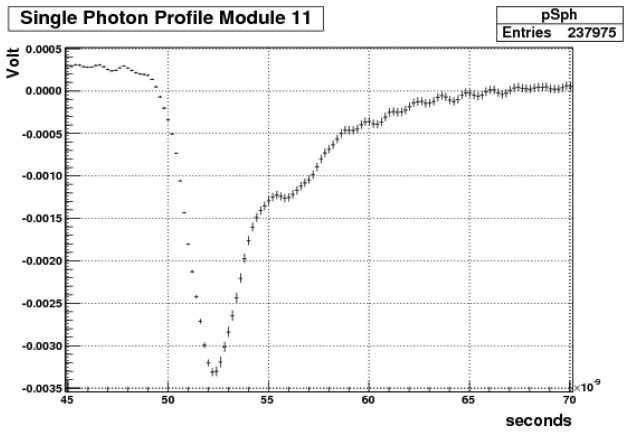

Figure 3.6: Average shape of single photon signals[64]

With these results we can achieve our goal, and determine how many photons are produced when the minimum ionizing particle pass through. For this purpose, the values from the MIP signals are divided by the values of single photons. The area under the PM signal is proportional to the integral of voltage over time and (since the voltage on the oscilloscopy is measured on a 50 Ω

resistor) hence proportional to the integral of current over time, hence charge equivalent to that proportion is the desired integral.

Here we evaluate the numbers in table 3.2 by comparing the results of MIP and Single Photon.

	MIP	Single photo	ratio
top value	95.74 mV	3.60 mV	26.59
half-value width	12.09 ns	3.52 ns	3.43
integral	1488.6 mV ns	23.5 mV ns	63.3

Table 3.2: Comparing of MIP and Single Photon.

The conclusion is that a minimum ionizing particle produces an average of 63.3 photons in the sandwich veto detector.

3.3 Efficiency of SVD

The efficiency for the MIPs was determined with 160GeV muon beams using a halo trigger (see COMPASS spectrometer). This beam is normally used for the alignment. The distribution of muons in the detector, which was reconstructed in the spectrometer for a track are shown in figure 3.7. A veto flag probability of 98% was obtained for the muons with a reconstructed track traversing the SVD, This value refers to homogeneous irradiation of the complete detector plane excluding the central hole. Tracks at the block edges contribute more than half of the missing 2%[23].

As registered matches all tracks are counted, which gave a hit(TDC) in the corresponding module of SVD. The voltage signal from one of the photomultiplier of the detector will be further processed by the TDC. The TDC indicates the arrival signal time relative to a reference time, thus the TDC signal contains time information. To determine the efficiency just need to compare the number of recorded with the number of muon tracks hits in the detector[64].

The aim was to determine the efficiency for the sandwich detector.

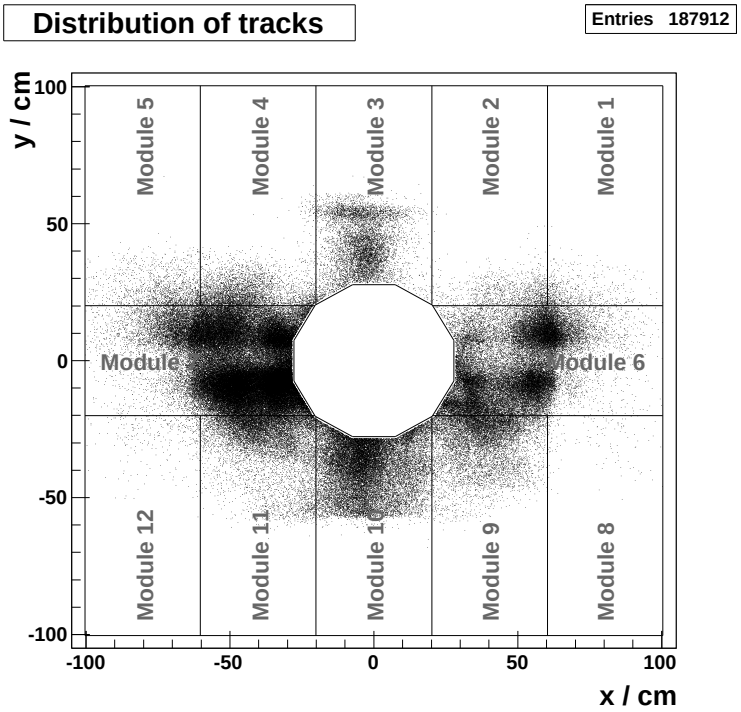

Figure 3.7: Distribution of reconstructed muon tracks in the sandwich - veto - detector as a function of the coordinates x, y perpendicular to the beam. Lines indicate the twelve modules from which the detector is composed.

The definition of the total efficiency is[64]:

$$\frac{\sum_i A_i \cdot \varepsilon_i}{\sum_i A_i} \tag{3.1}$$

Here the A_i is the area i of SVD, the ε_i is the efficiency of area i. In order to do the evaluation of the efficiency, the whole detector was divided in areas approximately $9.5cm \times 9.5cm$. For each area efficiency is calculated as the number of hits registered divided by the total number of hits. The efficiencies of the individual areas are shown in figure 3.8 with color palette.

$$\varepsilon_i = \frac{N_i^D}{N_i^H} \tag{3.2}$$

Where N_i^D is the number of detected μ in area i and N_i^H is the number of μ hitting area i.

Here we present the efficiency of the sandwich detector, which includes 12 modules which have been introduced in section 2.3.

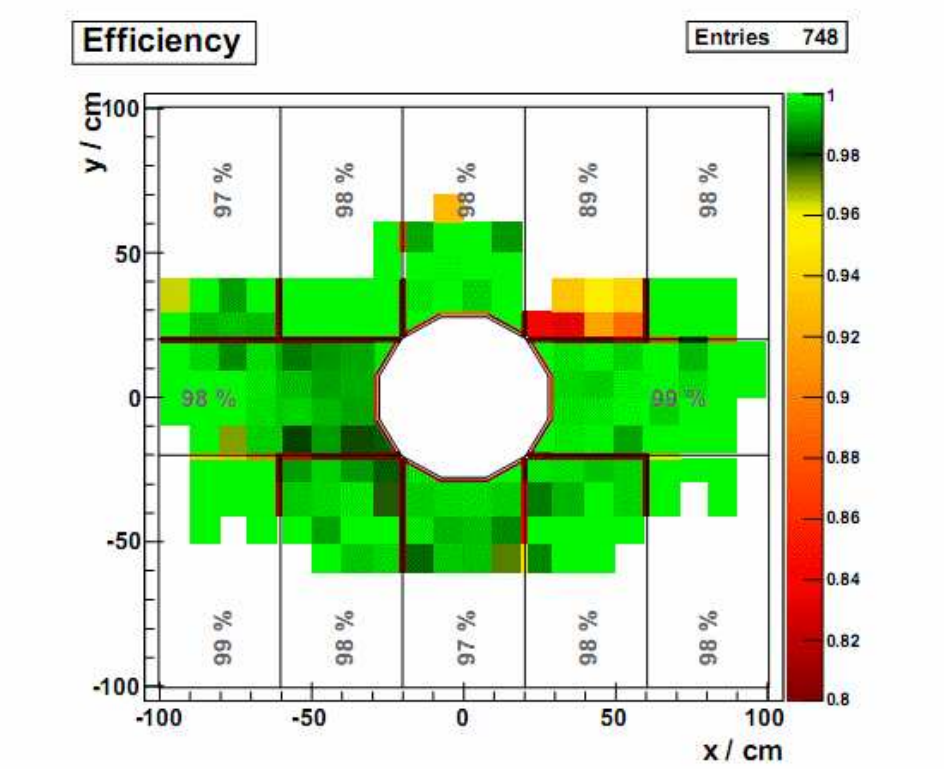

Figure 3.8: The efficiency of Sandwich Detector[64]

We sum over the efficiency of all bins weighted with their area(see figure 3.8).

Intrinsic Efficiency A: similar definition as total efficiency, just cut the border bins with 1cm margin.

Intrinsic Efficiency B: Sum of hits in one module divided the number of tracks which go through the module.

The table 3.3 show the efficiency for every Module and for the whole Sandwich with the 2008 and 2009 data[64].

	2009			**2008**
Module	total	intrinsic A	intrinsic B	intrinsic B
1	98.2 %	100.0 %	100.0 %	98.2 %
2	88.7 %	90.8 %	89.3 %	100.0 %
3	98.1 %	99.3 %	99.8 %	100.0 %
4	97.7 %	100.0 %	100.0 %	99.1 %
5	97.0 %	99.1 %	99.4 %	98.6 %
6	98.6 %	99.8 %	99.8 %	99.8 %
7	97.8 %	99.3 %	99.0 %	99.3 %
8	98.5 %	100.0 %	100.0 %	92.2 %
9	98.0 %	99.7 %	99.6 %	99.6 %
10	97.3 %	99.2 %	99.5 %	100.0 %
11	97.9 %	99.4 %	99.2 %	99.6 %
12	99.1 %	100.0 %	100.0 %	98.7 %
Detector	97.6 %	99.2 %		

Table 3.3: Efficiency of Sandwich-Veto-Detectors for 2009 and 2008 Data[64]. Intrinsic Efficiency A: Same as total efficiency, but without border areas (with 1cm margin). Intrinsic Efficiency B: Sum of hits in one module divided the number of tracks which goes through the module.

From the table 3.3 we can see the total efficiency of SVD is 97.6%. The efficiency A is (99.2 - 97.6)% higher than the total efficiency, which means the hole and edges lose tracks less than 1.6%. In the 12 modules there are six modules with the efficiency higher than 98% and six modules with the efficiency lower than 98%. If we take away the best module and worst module(88%), the efficiency of SVD should be 98%.

Chapter 4

Event selection of $\pi^- f_1$

In this chapter the event selection of $\pi^- f_1$ is presented. First of all the tools which are usually used in COMPASS should be introduced. Then the analyzed data set and the event selection are presented. In order to understand what we have detected with all kinds of detectors, event selection takes a very important role. In this thesis, we concentrate on the event selection of these processes:

$$\pi^- p \to X p,$$
$$\mathrm{X} \to \pi^- f_1,$$
$$f_1 \to \pi^- \pi^+ \eta,$$

Then we have two cases of η decays, $\begin{cases} \eta \to \pi^- \pi^+ \pi^0, \pi^0 \to \gamma\gamma \\ \eta \to \gamma\gamma. \end{cases}$

In the first section we describe the event selection of $\gamma\gamma$, $\pi^-\pi^+\gamma\gamma$, $\pi^-\pi^+\pi^-\pi^+\gamma\gamma$, $\pi^-\pi^-\pi^+\pi^-\pi^+\gamma\gamma$. Then we apply the cut for π^0, η, f_1, $\mathrm{X}(\pi^- f_1)$ and reconstruct all the reactions during the process $\pi^- p \to \pi^- f_1 p$.

4.1 The analysis tools in COMPASS

In order to extract physics from the experiment at COMPASS, we need some tools to analyse the raw data which we get from the experiment. The usual tools include ROOT, PHAST, CORAL and so on. The goal is to obtain the information about the mass, angular, t distribution, four vector of particles and so on. The raw data is first decoded using a Data Decoding library. Data from calibration and slow control measurements are stored in a MySQL data base.[15]

4.1.1 ROOT

The amount of data generated from the Large Hadron Collider(LHC), beginning to run at the year 2009, is larger than anything seen before. And the twenty-year-old FORTRAN libraries can not meet the request. Although PAW(Physics Analysis Workstation), and GEANT(program describes the passage of elementary particles through the matter) are still very popular, these tools could not scale up to the challenges. The ROOT looks like the tools specially for the experiment of LHC and COMPASS experiment profits from this.

ROOT is an object-orientated analysis tool to analyse data in high energy physics[29]. It was developed in the context of the NA49 experiment at CERN. NA49 has generated an impressive amount of data, around 10 TB per run. This rate provided the perfect environment to test and develop the next generation data analysis. Before use of ROOT, we should know something about CINT(its C++ interpreter). It is an independent production which ROOT is using for the command line and script processor[29].

The development of ROOT is a continuous conversation between users and developers with the line between the two blurring at times and the users becoming codevelopers. When it comes to storing and mining large amount of data, physics plows the way with its Terabytes, but other fields and industry follow close behind as they acquire more and more data over time. They are ready to use the true and tested technologies physics has invented. In this way, other fields and industries have found ROOT useful and they have started to use it also. The data is structured in branches and store in trees on an event-by-event basis[29].

The results can be presented visually in order to analyse and evaluate the information. This program plays a very important role in the COMPASS analysis work. It provides an efficient way to archive diverse data in a structured way. All the non-calibration data are stored in ROOT files, include raw data, mDST and so on.

4.1.2 CORAL

CORAL(Compass Reconstruction and AnaLysis) is the data reconstruction programme in COMPASS. With the help of the DAQ(Data Acquisition) and MySQL(Structured Query Language)[11] data base the programme CORAL

is able to reconstruct vertices and tracks for every processed event, while the reconstruction occurs in several steps.

First of all, the data read-out of the hardware is digitized and transformed into time information and signal amplitudes. For that purpose abstract electronics identification numbers of all detector channels are mapped to real 3-dimensional coordinates. These informations shed light on particle trajectories, using magnets (SM1, SM2) and the RICH detector[63].

Subsequently, the output is written into mDST (Mini Data Summary Tree) files which can be reconstructed by the analysis tool PHAST.

4.1.3 PHAST

PHAST(Physics Analysis Software Tool) is used to read the produced mDST files, which provides access to reconstructed event information and allows the proceeding and filtering of event subsamples[16].

PHAST is the framework for data analysis of the COMPASS experiment on the level of mDST. It provides:
1) access to reconstructed event information
2) environment for physics analysis code developments
3) tools for mDST processing and filtering of events' sub-samples

PHAST also provides mDST output data stream at the stage of event reconstruction. Moreover, PHAST allows to use standardized selection routines for analysis purposes and gives the opportunity to create reduced mDST files (called μDST) which contain preselected event samples.

4.2 Event selection

What can happen when an incoming negative π beam with 190 GeV energy(E_{π^-}) hits the proton? After this chapter we should get some answers from here.

For this analysis, which is presented in this thesis, the principle of particle identification and reconstruction is based on the knowledge, that neutral particles (like the π^0 and η) decay into $\gamma\gamma$ which are detected and charged pions $\pi^{\pm}$ do not decay, in general, inside the spectrometer.

An η in the final state $\pi^- p \to \pi^-\pi^-\pi^+\eta$p rapidly decays into $\gamma\gamma$, whose energy and position are assigned by the electromagnetic calorimeters of the COMPASS experiment.

The data selection occurs in several steps, which will be described in the following[11]:

(1)the trigger selection

(2)the beam composition

(3)vertex selection (within the target)

(4)Recoil Proton Detector

(5)cluster selection in ECAL1 and ECAL2 calorimeters

(6)kinematic fitting routines were integrated into the data selection to improve the reconstruction

The figure 4.1 show the process.

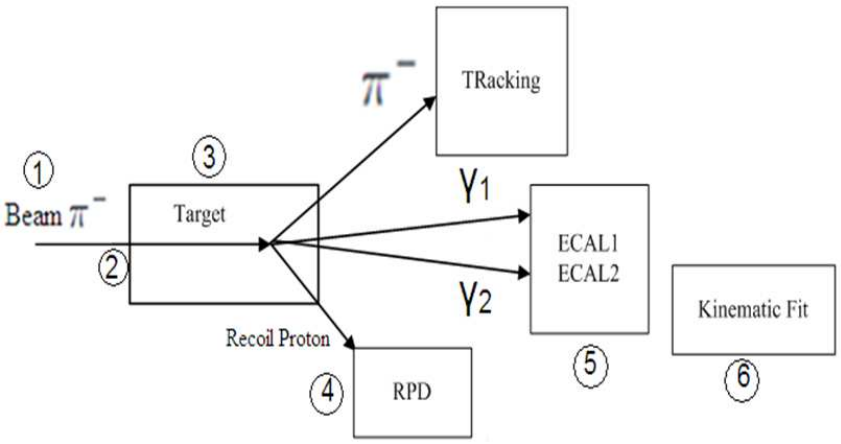

Figure 4.1: The process of event selection. Selected event topology in the reaction $\pi^- p \to \pi^-\pi^0 p$ or $\pi^-\eta p$ is shown as an example.

1) Trigger

The preselection is done with the DT0 Trigger. The DT0 is a hadron trigger which is used in 2008 data to select events where the beam particle (π^-) is diffractively excited[21]. The composition of the DT0 trigger is the following (used for minimum selection criteria).

The Beam Trigger is used to trigger on interactions of the beam in the target region[11]. To respect the geometrical properties of the target, such as its cylindrical shape, this trigger is provided.

A Proton Trigger is used to select recoiling protons emitted from the target. These protons are detected by the Recoil Proton Detector (RPD). They are identified by time-of-flight and energy loss measurements[11].

The veto system is used to detect secondary particles produced along the beamline (hadronic interactions), halo particles, non-interacting particles and interactions leading to particles going outside the angular acceptance of the spectrometer and to reject such events.

2) The π^- Beam

The incoming beam from the M2 beam line is not a pure pion beam: It contains kaons ($\approx$ 4.5 percent) and anti-protons ($\approx$0.5 percent)[38].

To exclude negatively charged kaons of the incoming beam, a majority of hits in CEDAR 1 and CEDAR 2 less than 6 was claimed. The two CEDAR detectors were set to detect kaons. Majority < 6 correspond to a veto on Kaons[18]. This cut reduces the small fraction of kaons. Unfortunately, an exact percentage of the rejected kaons is unknown. One possible explanation for not knowing the exact value is that only 1/3 of the beam is tagged by the CEDARs[18].

3)Vertex Selection

For vertex selection we are asking for exactly one primary vertex. A primary vertex is a detected crossing point between the incoming beam and outgoing particles from the first(primary) interaction point of the beam hitting the target (in a fixed target experiment)[11]. In collision experiments this interaction point is defined as the point where the particles collide.

Due to pileup events which often occur in the reconstruction, we lose statistics. Pileup are background events which are added to the observed signal[62]. They originate in multiple events that appear in the same time window as the signal of interest. Pileup frequently occurs in high luminosity experiments, such as colliding experiments, where multiple collisions can happen during a

single bunch crossing.

There are three outgoing negative charged tracks from every vertex in the reactions $\pi^- p \to \pi^- \pi^+ \gamma\gamma\pi^- p$ or 5 charged tracks in $\pi^- p \to \pi^- \pi^+ \pi^- \pi^+ \gamma\gamma\pi^- p$. One incoming π beam and 3 or 5 outgoing tracks are from the primary vertex. The primary vertex was located inside of the cylindrical hydrogen target: R [cm] < 1.57 and -67.5 < z (beam direction) [cm] < -29.5.

Every individual track can be defined by a Lorentz vector[62]. Then we can get information about the energy of each track. For the f_1 final state 3 or 5 charged tracks are requested for every primary vertex. In the case of 3 or 5 outgoing particles, the $\pi^- f_1$ system fulfilled the energy balance given by the incident beam particle: $186 < E[GeV] < 196$ (The recoil proton carries a negligible amount of kinetic energy).

4) RPD Criteria

For the azimuthal correlation between the direction of the flight of a recoiling track (proton in this case) in the RPD with the direction of the flight of the negatively charged system X(πf_1), the azimuthal angles were required to be in the range of -0.3 < ϕ_{f_1}-ϕ_{π^-} < 0.3[61].

5) Cluster Selection in ECAL1 and ECAL2

$\gamma\gamma$ result from the π^0 or η decay, therefore exactly 2 "good" clusters were selected in ECAL1 and ECAL2, in accordance with the following criteria: Each cluster, which is detected by the electromagnetic calorimeters, correlates to an electromagnetic shower in a group of neighbouring crystals. These clusters are not pointed by a charged track[11].

A minimum of energy deposition in the calorimeter cells is essential, therefore we use 1 GeV for ECAL1 clusters and 4 GeV for ECAL2[11]. Since all of the clusters must be in time with the beam, an additional time cut was performed: the difference of the beam time and the cluster time must be within t = -3 ns and t = 5 ns.

6) Kinematic Fitting

Experimental measurements of quantities like momentum, mass, time, 4-vectors etc. are always with errors. For this reason we need a procedure which is able

to improve our measurements and to give better results(This was introduced by Tobias Schlüter[11]).

A kinematic fitting routine is a mathematical process, that uses physical constraints to enhance the measurements. To check the performance of the fitting, two distributions are used, confidence level distribution and pull distribution[11].

The confidence level distribution checks the amicability of a fit (data) to the hypothesized event, while the pull distribution estimates the quality of the error estimation[62].

Kinematic fitting works as this, using a reliable hypothesis for an event, one can derive constraints which convert the measured values within their error to fulfill special requirements[12].

4.3 Selection of events with 2 good γ clusters

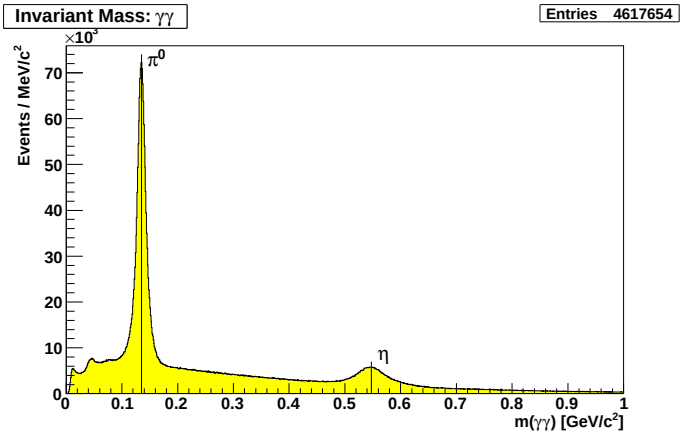

Figure 4.2: Invariant mass of $\gamma\gamma$. Distribution of the events as a function of the invariant mass $m_{\gamma\gamma}$ in $\pi^- p$ reaction[64].

After we get the mass distribution about $\gamma\gamma$, we can see two peaks corresponding to π^0 and η. We have two ways to detect the $\pi^- f_1$ final state. One is using the decay $\eta \to \pi^-\pi^+\pi^0, \pi^0 \to \gamma\gamma$. Another is the decay $\eta \to \gamma\gamma$. Peaks at low mass $\approx 0.03\ GeV/c^2$ are unphysical(see Tobias Schlüter's talk[60]).

4.4 5π final state

The $\eta \to \pi^-\pi^+\gamma\gamma$ are discussed in this section. The mass distributions in the decay channel of X $\to$ 5 charged π and $\gamma\gamma$ has been shown in figure 4.3, 4.4 and 4.5.

4.4.1 Selection of events with $\eta \to \pi^-\pi^+\pi^0$

The figure 4.3 shows the invariant mass distribution of $\pi^-\pi^+\pi^0$.

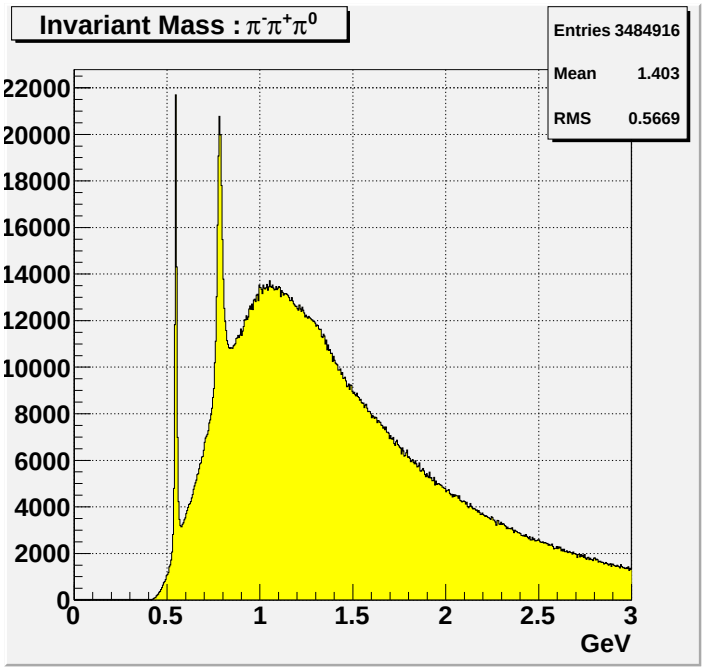

Figure 4.3: Invariant mass of $\pi^-\pi^+\pi^0$. Distribution of the events as a function of the invariant mass $m_{\pi^-\pi^+\pi^0}$ in the $\pi^- p$ reaction after the selection $\pi^0 \to \gamma\gamma$ with the cut window: $|m_{\gamma\gamma} - m_{\pi^0}| < 20 MeV/c^2$.

The mass distribution of $\pi^-\pi^+\pi^0$ displays two peaks. First one at the mass 560±2 MeV corresponds to the η and second one at the mass 782±5 MeV corresponds to the ω.

From the figure 4.3 we learn that the ω has higher background than η.

4.4.2 Selection of events with $f_1 \to \pi^-\pi^+\eta$

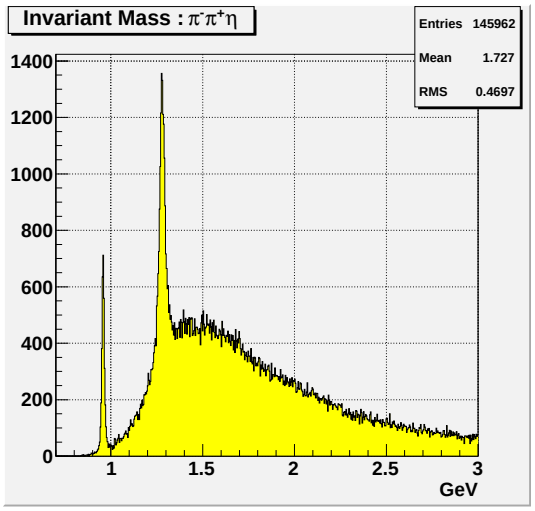

Figure 4.4: Invariant mass of $\pi^-\pi^+\eta$. Distribution of the events as a function of the invariant mass $m_{\pi^-\pi^+\eta}$ in the $\pi^- p$ reaction after the selection $\eta \to \pi^-\pi^+\pi^0$ with the cut window: $|m_{\pi^-\pi^+\pi^0} - m_\eta| < 20 MeV/c^2$.

From the mass distribution of $\pi^-\pi^+\eta(\eta \to \pi^-\pi^+\pi^0)$, we can see two peaks at the mass 0.95 and 1.25 GeV corresponding to $\eta^{'}$ and f_1 (Figure 4.4).

4.4.3 Selection of events with $X \to \pi^- f_1$

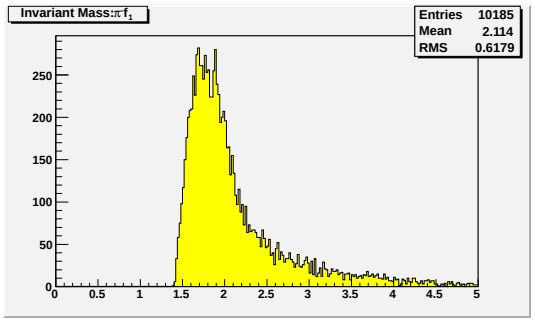

Figure 4.5: Invariant mass of $\pi^- f_1$. Distribution of the events as a function of the invariant mass $m_{\pi^- f_1}$ in the $\pi^- p$ reaction after the selection $f_1 \to \pi^-\pi^+\eta$ with the cut window: $|m_{\pi^-\pi^+\eta} - m_{f_1}| < 30 MeV/c^2$ which is range [1.255,1.315] GeV/c^2.

The mass distribution of $\pi^- f_1(5\pi)$ shows that the leading events are concentrated in the mass range [1.6, 2.0]GeV after the total energy exclusively cut for 5 π.

4.5 3π final state

The $\eta \to \gamma\gamma$ are discussed in this section. The mass distributions in the decay channel of X $\to$ 3 charged π and $\gamma\gamma$ has been shown in figure 4.6, 4.7 and 4.8.

4.5.1 Event selection for $f_1 \to \pi^-\pi^+\eta(\gamma\gamma)$

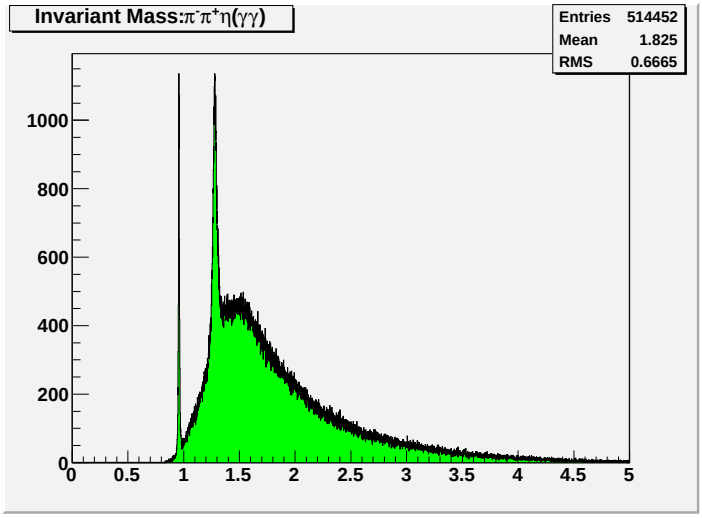

Figure 4.6: Invariant mass of $\pi^-\pi^+\eta$. Distribution of the events as a function of the invariant mass $m_{\pi^-\pi^+\eta}$ in the $\pi^- p$ reaction after the selection $\eta \to \gamma\gamma$ with the cut window: $|m_{\gamma\gamma} - m_\eta| < 20 MeV/c^2$.

From the mass distribution of $\pi^-\pi^+\eta(\eta \to \gamma\gamma)$, we can see two peaks at 958±1 MeV and 1282±5 MeV corresponding to $\eta^{'}$ and f_1.

4.5.2 Event selection for $X \to \pi^- f_1$

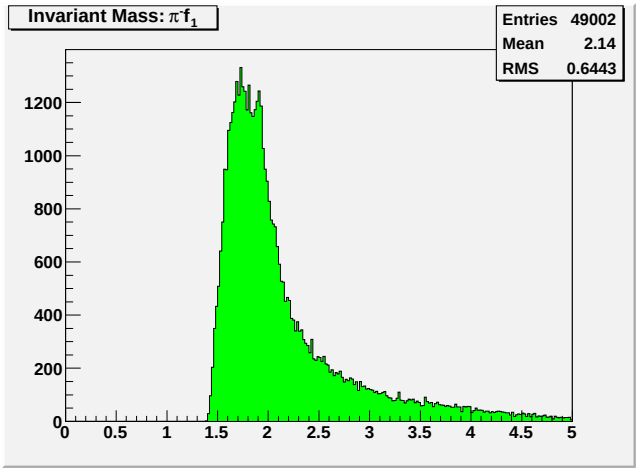

Figure 4.7: Invariant mass of $\pi^- f_1$. Distribution of the events as a function of the invariant mass $m_{\pi^- f_1}$ in the $\pi^- p$ reaction after selection $f_1 \to \pi^-\pi^+\eta, \eta \to \gamma\gamma$ with the cut window: $|m_{\pi^-\pi^+\eta} - m_{f_1}| < 30 MeV/c^2$ which is range [1.255,1.315] GeV/c^2.

The mass distribution of $\pi^- f_1(3\pi)$ plot is consistent with the one shown in the figure 4.5 after the total energy exclusively cut for 3 π.

Selections	Events	Mass peak	possible particles
$\gamma\gamma$	4617654	135±1MeV	π^0,η
$\pi^-\pi^+\pi^0$	3484916	560±2MeV,782±5MeV	η,ω
$\pi^-\pi^+\eta(3\pi)$	145962	958±2MeV,1282±5MeV	$\eta^{'}$,f_1
$\pi^-\pi^+\eta(\gamma\gamma)$	514452	958±2MeV,1282±5MeV	$\eta^{'}$,f_1
$\pi^- f_1(5\pi)$	10185	around 1700 MeV	$\pi_1(1600)$, $a_1(1640)$, $\pi_2(1880)$...
$\pi^- f_1(3\pi)$	49002	around 1700 MeV	$\pi_1(1600)$, $a_1(1640)$, $\pi_2(1880)$...

Table 4.1: The Event numbers and possible particles are listed after different selections. The third line is $\eta \to \pi^-\pi^+\pi^0$ and fourth line is $\eta \to \gamma\gamma$. The fifth line is $f_1 \to \pi^-\pi^+\pi^-\pi^+\pi^0$ and sixth line is $f_1 \to \pi^-\pi^+\gamma\gamma$.

4.6 Dalitz plotz

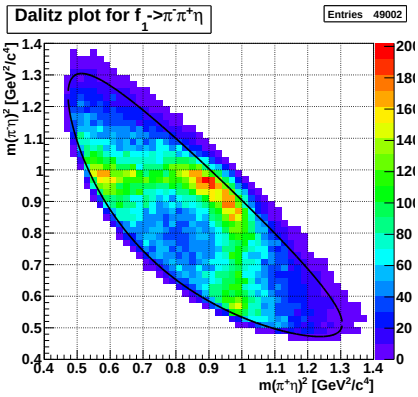

Figure 4.8: $f_1 \to \pi^-\pi^+\eta, \eta \to \gamma\gamma$. The y-axis is the $m^2_{\pi^-\eta}$ and the x-axis is the $m^2_{\pi^+\eta}$[64].

In the Dalitz plot, the number of events of a 3-body final state are plotted as a function of two (of the three) invariant 2-body masses squared.

From the Dalitz plot for the decay $f_1 \to$ both $\pi^-\eta$ and $\pi^+\eta$ we can see the a_0 around 1.0 GeV/c^2. In the middle, with the overlap of $\pi^-\eta$ and $\pi^+\eta$, the number of events is double to the events in the $\pi^-\eta$ or $\pi^+\eta$.

Chapter 5

Kinematical distribution of $\pi^- f_1$

In this chapter we present the kinematical distributions of the $\pi^- f_1$ channel. First we show the mass distributions. We take all of the combinations into consideration. Second we list the t distribution in 500MeV/bin of the $\pi^- f_1$ mass and compare two kinds of fit, one is $Aexp(-bt^{'})$, another one is $At^{'}exp(-bt^{'})$. Third we present the angular distribution. We compare the angular distributions in the Gottfried-Jackson and the helicity frame.

5.1 Mass distributions

After event selection, which has been discussed in chapter 4, now we want to understand more about the different π^- and π^+ distributions. There are two π^- in the final state for the case $\eta \to \gamma\gamma$. In most cases(more than 98%) one is uniquely associated to the f_1 decay. Here we set the X as $\pi_2^- f_1$ and f_1 as $\pi_1^-\pi^+\eta$. It means that the π_1^- is the π^- from the f_1 decay and π_2^- is not. Fig. 5.1-5.3 show all the mass distributions for the case when $\eta \to \gamma\gamma$.

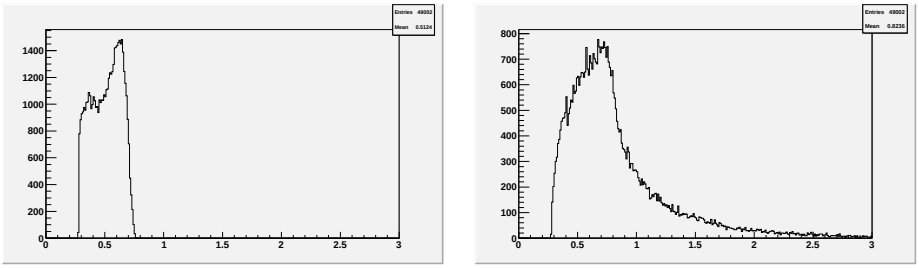

Figure 5.1: Invariant mass of $\pi_1^-\pi^+$(left) and mass of $\pi_2^-\pi^+$(right) after f_1 selection. $\eta \to \gamma\gamma$. The π_1^- is the π^- in f_1.

In the figure 5.1, the left plot is the mass of $\pi_1^-\pi^+$ distributions with the π_1^- from the f_1 decay. It shows peaks at 0.3 and 0.7 GeV. Due to the mass of $\pi^\pm$ (0.139 GeV), the sum of $\pi^-\pi^+$ is around the first peak. The second peak supports these two π may result from the σ or f_0 decay. It means that $\pi_1^-\pi^+\eta$ in the f_1 selection window(see section 4.5) have the $(\pi^-\pi^+)_S\eta$ decay channel, dominantly $(\pi^-\pi^+)_S \approx f_0$ or σ.

The mass distribution of $\pi_1^-\pi^+$ sharply falls down when the mass > 0.7 GeV. The $\pi_1^-\pi^+$ mass distribution depends on f_1 and η mass windows(see section 4.5). The $m_{\pi_1^-\pi^+}$ can not be larger than $m_{f_1} - m_\eta \approx 0.7$ GeV. The right plot is the mass of $\pi_2^-\pi^+$ distributions.

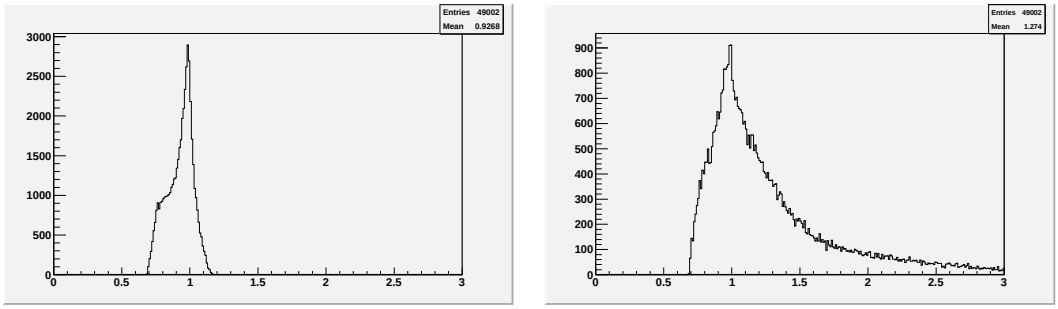

Figure 5.2: Invariant mass of $\pi_1^-\eta$(left) and mass of $\pi_2^-\eta$(right) after f_1 selection. $\eta \to \gamma\gamma$.

Fig. 5.2 show that the both the $\pi_1^-\eta$ and $\pi_2^-\eta$ have a peak around 1.0 GeV, which may correspond to the $a_0(980)$. The right one has more background because the $\pi_1^-\pi^+\eta$ with the limit of f_1 selection but $\pi_2^-\pi^+\eta$ without any selection. It means after the f_1 event selection we reduce the combinatorial background.

The a_0 in $\pi_1^-\eta$ is expected, known from previous measurement, (see Dalitz plot page 50) and the a_0 for π_2^- with the η may be due to the background under f_1.

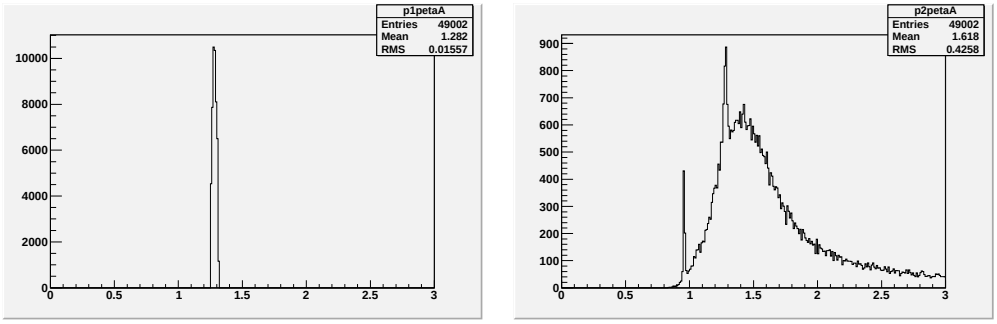

Figure 5.3: Invariant mass of $\pi_1^-\pi^+\eta$(left) and mass of $\pi_2^-\pi^+\eta$(right) after f_1 selection. $\eta \to \gamma\gamma$.

From figure 5.3, we can learn that the f_1 selection cut the mass window of $\pi_1^-\pi^+\eta$(see section 4.5) but do not cut the $\pi_2^-\pi^+\eta$. Comparing the right plots($\pi_2^-\pi^+\eta$ distributions after f_1 selection) with the $\pi^-\pi^+\eta$ distributions without f_1 selection(fig. 4.6 in section 4.5.1), we can see the $\pi_2\pi^+\eta$ mass distributions have more background. It make sense, because before we do the f_1 selection the distributions includes either π_1^- or π_2^- but after we cut the mass of $\pi_1\pi^+\eta$ with f_1 window, the suitable π^- take as π_1^- by the program and another π^- take as the π_2^-. But anyway the $\pi_2^-\pi^+\eta$ still have the peaks at the $\eta^{'}$ and f_1 which is supported by the $\pi^-\pi^+\eta$ distributions in section 4.5.1. The number of events in this peak f_1 is ≈ 500(see figure 5.3), thus for $1\%(\approx 500/49002)$ of the events, both $\pi^-\pi^+\eta$ combinations yield the f_1, which are the ambiguous events.

In the case of $\pi^- f_1$ decay when $\eta \to \pi^-\pi^+\pi^0$ we have 3 π^- and 2 π^+, So we have $\binom{2}{3}\binom{1}{2} = 6$ cases of $\pi^-\pi^+$ combinations. In order to analyse the procession, we decide to compare the 6 cases. The mass distribution of $\pi^-\pi^+$, $\pi^-\pi^+\pi^0$ and $\pi^-\pi^+\pi^-\pi^+\pi^0$ with all kinds of combinations will be shown in appendix A.

5.2 t distributions

The $t^{'}$ is defined as:

$$t^{'} = |t| - |t_{min}|, |t_{min}| \approx \frac{(m_{Out}^2 - m_{Beam}^2)^2}{4|\vec{P}_{Beam}|^2} \tag{5.1}$$

where the t has been defined as in section 1.3. The m_{Out} and m_{Beam} are the mass of outgoing system X and incoming π^-. The $\vec{P}_{Beam}$ is the momentum of

the incoming π^-.

Here we show the t distribution when the mass range of the $\pi^- f_1$ is 1.50-2.0 GeV and fits of two possible t functions which are usually applied in the PWA(from[64]). Other t distributions will be presented in the appendix B.

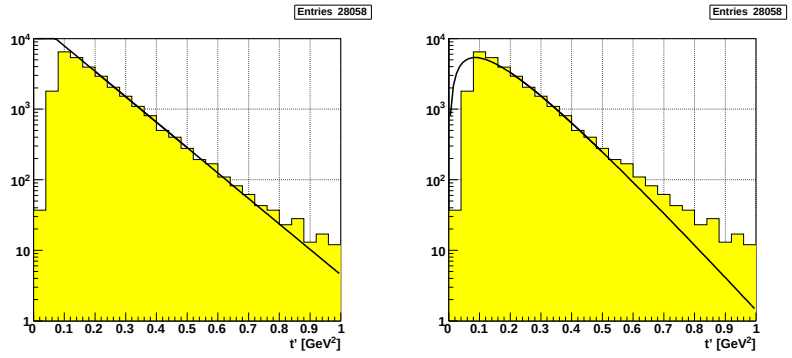

Figure 5.4: The fit $A\exp(-bt')$ vs $At'\exp(-bt')$: $1.50 < m(\pi^- f_1) < 2.00$[64]

The fit $A\exp(-bt')$ is used when the projection of the spin J of X is M=0 and $At'\exp(-bt')$ is used when the projection is M=$\pm$1 which will be applied in chapter 7.

5.3 Angular distributions

Various reference systems are used for the decay angular distributions. In this section the Gottfried-Jackson frame and the helicity frame will be discussed.

In order to learn more from the $\pi^- f_1$ decay, we divide the mass into 500 MeV intervals. First of all, we define the angle θ and ϕ in the Gottfride-Jackcen frame and helicity frame. Then the angular distribution of $X \to \pi^- + f_1$ are shown.

5.3.1 Gottfried-Jackson frame

The Gottfried-Jackson frame has relation to the t-channel conservation which implies that the spin of $\pi^- f_1$ is aligned along the direction of the beam. In the Gottfried-Jackson frame, which is presented in the following picture, the

quantization axis(z axis) is defined as the direction of the beam after boost into X = $\pi^- f_1$ rest system. The direction of the decay particle f_1 defines the polar angle θ_G with the z axis.

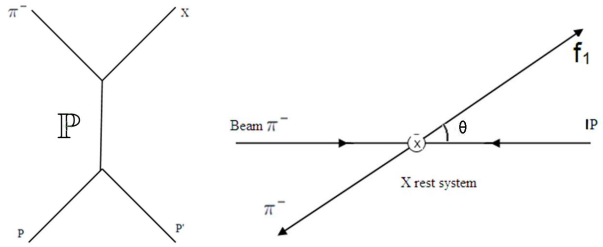

Figure 5.5: The definition of θ_G in G-J frame. $\mathbb{P}$ is the symbol for the exchanged particle supposedly a pomeron.

Here the $\vec{\mathbb{P}} = \vec{p}_{in} - \vec{p}_{rec}$ is the momentum of the exchange particle, $\vec{p}_{in}$ and $\vec{p}_{rec}$ are the momenta of the incoming proton and recoil proton. The θ distribution is obtained in this way: first rotate all the momenta $\vec{p}_{\pi^-}$(incoming π^-), $\vec{p}_{in}$, $\vec{p}_{rec}$ and $\vec{p}_X$ around the laboratory beam axis, so that they are in the x-z plane with the X pointing in the direction of positive x. This defines the production plane. Then we boost all the momenta $\vec{p}_{\pi^-}$, $\vec{p}_{in}$, $\vec{p}_{rec}$ and $\vec{p}_{f_1}$ into the X rest system, with the z axis defined as the direction of beam. The direction of y axis was defined vertical to the production plane.

The azimuthal angle ϕ is defined by the production plane and f_1 momentum in X rest system. The θ and ϕ defined as this section will be used as θ_G and ϕ_G in the chapter 7.

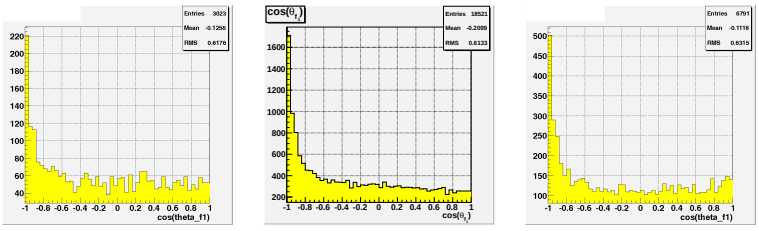

Figure 5.6: G-J frame: the $\cos\theta_G$ distributions in X rest system

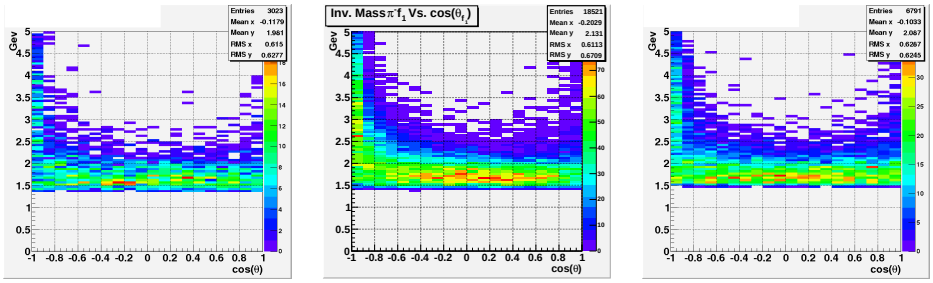

Figure 5.7: The mass of X vs $\cos\theta_G$ distributions in X rest system

From the figure 5.7 we can learn that most of the events are within the mass range from 1.5GeV to 3.0GeV. With increasing mass of X more events have $\cos\theta_G$ close to -1. In order to see the angular distribution in different mass ranges more clearly, now we divide the mass into intervals of 200 MeV. Here we present the mass range from 1.5 to 1.8 GeV, more results will be listed in the appendix C.

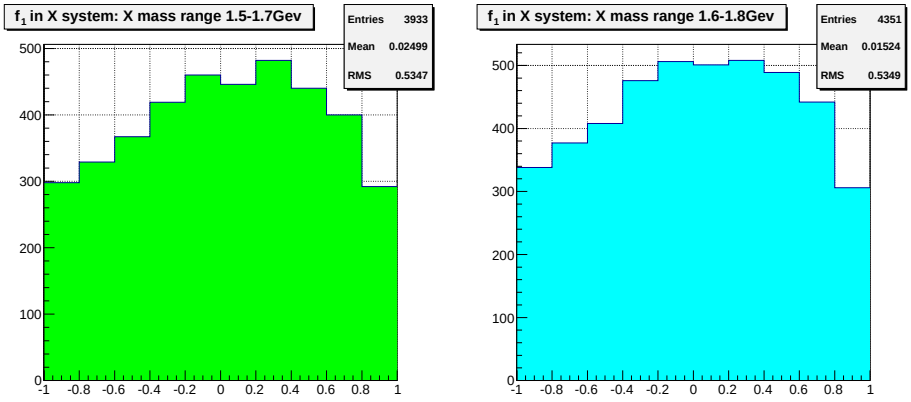

Figure 5.8: $cos\theta_G$ distribution in X rest system:1.5-1.8. The left plot is for the mass range [1.5, 1.7] GeV and the right plot is for the mass range [1.6, 1.8] GeV.

Figure 5.8 support that in the mass range [1.5, 1.8] GeV the $\cos\theta_G$ distribution has a maximum but not symmetrical around 0.

Since the f_1 has high background($\approx 50\%$, see figure 5.6), we want to know how many contributions are from the background in every X mass bin. We assumed the sum of left side-bin and right side-bin distributions are similar as the background in the central bin. The left side-bin with 1.205 GeV $\leq m_{\pi^-\pi^+\eta} \leq$

1.235 GeV; the central bin with 1.255 GeV $\leq m_{\pi^-\pi^+\eta} \leq$ 1.315 GeV; the right side-bin with 1.335 GeV $\leq m_{\pi^-\pi^+\eta} \leq$ 1.365 GeV. It can be seen that after background subtraction the angular distribution shall be more symmetrical around $\cos\theta_G$=0.

Here we show the results again for the X mass range from 1.5 to 1.8 GeV. More plots are shown in appendix C.

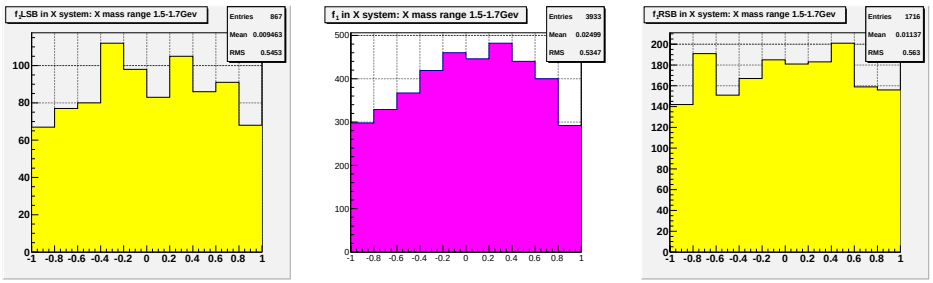

Figure 5.9: The $\cos\theta_G$ distribution in X rest system:1.5-1.7. The left one is the left side-bin; the middle one is the central bin; the right one is the right side-bin.

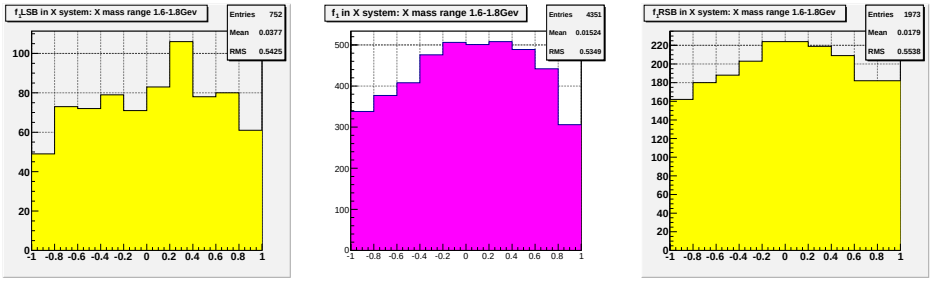

Figure 5.10: The $\cos\theta_G$ distribution in X rest system:1.6-1.8. The left one is the left side-bin; the middle one is the central bin; the right one is the right side-bin.

Here we show the ϕ_G distributions of X=$\pi^- f_1$ system in G-J frame where $\eta \to \gamma\gamma$.

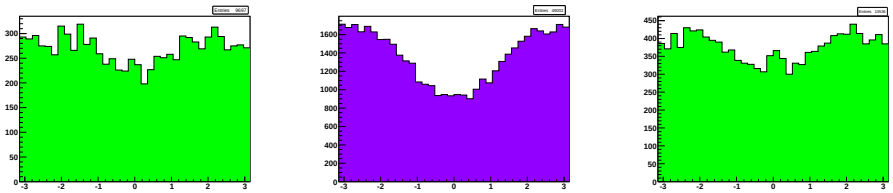

Figure 5.11: The ϕ_G distribution in the X rest system(G-J). The left one is the left side-bin; the middle one is the central bin; the right one is the right side-bin.

In order to learn more about ϕ distributions, we compare ϕ_G distributions in G-J to ϕ_H distributions of the HL frame where $\eta \to \gamma\gamma$.

5.3.2 Helicity frame

The Helicity frame is related to the s-channel helicity conservation which is examined in the helicity frame. In the helicity frame of X system the quantization axis (z) points into the direction opposite to the recoil proton in the CMS of π^-proton, respectively.

Here the θ_H definition is done as this way: first boost into the total CMS. In this system boost the recoil proton into total CMS, then boost π^-, f_1 into the X rest system. The definition of the z axis is the opposite direction of recoil proton and defines the y axis vertical to the production plane(see section 5.3.1).The direction of the decay-particle f_1 defines the polar angle θ_H with the z axis. The azimutal angle ϕ_H is defined by the production plane and f_1 momentum in X rest system.

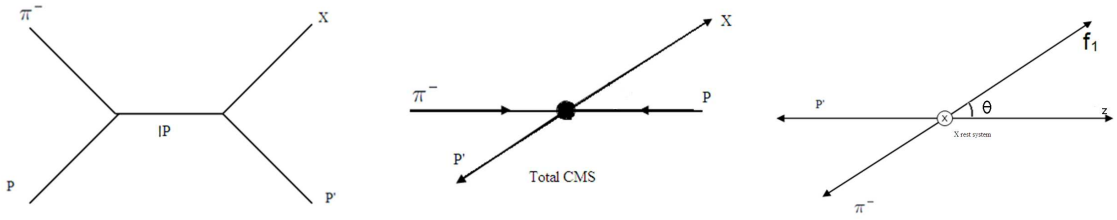

Figure 5.12: The definition of θ_H in the Helicity frame

Here we show the ϕ_H distributions of X=$\pi^- f_1$ system in HL frame where $\eta \to \gamma\gamma$.

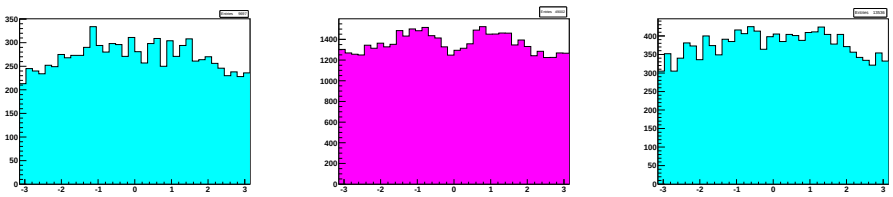

Figure 5.13: The ϕ_H distribution in X rest system(HL) where $\eta \to \gamma\gamma$. The left one is the left side-bin; the middle one is the central bin; the right one is the right side-bin.

Chapter 6

Monte Carlo simulation

In this chapter the Monte Carlo(MC) simulation will be described. A presentation of the MC simulation for the exclusive $\pi^- f_1$ production will be given. The full MC using the COMGEANT in order to simulate all details of the spectrometer and, last but not the least, the fast MC will be introduced in section 6.1. In section 6.2 and 6.3 the mass distribution and angle distribution are shown with 1 million events generated and accepted. In section 6.4 we show the acceptance of mass and angular distribution.

6.1 Full MC

The Monte Carlo simulation is the tool to calculate acceptance corrections. It is generally divided into three steps, which form the so called Monte Carlo chain[19]:
1) The generation of events: this is obtained using a computer program which creates artificial events. A list of particles together with their 4-vector momenta, randomly generated satisfying some predefined kinematic distribution characteristic of the reaction under investigation[19].
2) The output of the event generation is read by a second program, which simulates the physical processes which take place during the interaction of the generated particles with the material of the detector components.[54] At the end of this process, the position of hits in the tracking detectors, together with time information, showers simulation in the electromagnetic and hadronic calorimeters, radiation in the Cherenkov detectors, the bending of charged particles trajectories in the magnetic fields present, all these processes are simulated and quantitatively determined[19].
3) From the information obtained so far, the same reconstruction program

used for real data is used to reconstruct the MC events and store them in files ready for analysis[19].

6.1.1 COMGEANT

In COMPASS we use COMGEANT to do the Monte Carlo simulation. Before we disscus the COMGEANT, we should know GEANT which is a system of detector description and simulation tools that help physicists in more and more fields[25]. The GEANT program describes the passage of elementary particles through the matter. Originally designed for the High Energy Physics experiments, it has today found applications also outside this domain in the areas of medical and biological sciencies, radioprotection and astronautics[25]. The principal applications of GEANT in High Energy Physics are: 1. the tracking of particles through an experimental setup for simulation of detector response. 2. the graphical representation of the setup and of the particle trajectories. COMGEANT is derived from a frozen version of the GEANT3 simulation tool, developed during the last decades at CERN.

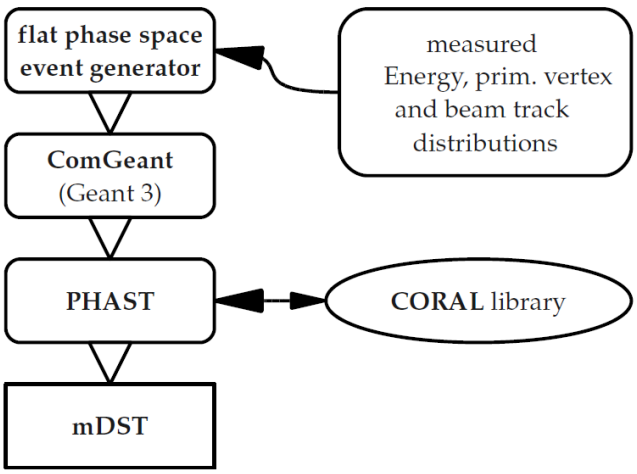

Figure 6.1: A MC chain illustrating the typical simulation flow for COMPASS analysis[63]

Figure 6.1 shows a typical COMPASS Monte Carlo (MC) software chain as it was set up to simulate the acceptance of exclusive diffractive processes. Events, produced by generator, were propagated through the spectrometer by

the COMPASS GEANT (COMGEANT) software[63]. The COMPASS Reconstruction Library (CORAL) package was simulating most of the detector responses for final user event selection and analysis.

At COMPASS, MC data are written in the same format(mDST files) as real data. At this point, the same routines written by the user to analyse the real data are employed to analyze the reconstructed MC data[19]. A quantitative comparison of the generated and reconstructed MC data puts in evidence the cumulative effect of geometric acceptance, detector and event reconstruction efficiency, which all contribute to the distortions of the various spectra characteristic of real data. After the Monte Carlo acceptance calculations, real data may be corrected and results of physical interest gained from the analysis[19].

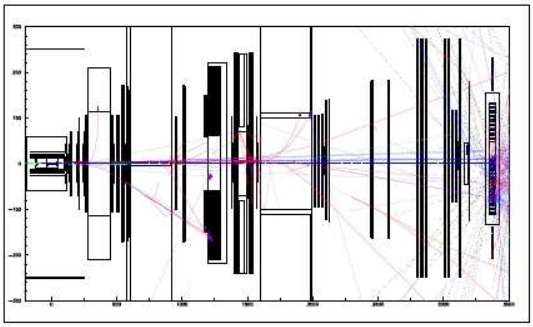

Figure 6.2: Event display for a simulated $\pi^- p$ interaction with COMGEANT.

A graphical representation of simulated $\pi^- p$ interactions and subsequent decays as seen by COMGEANT can be viewed in the figure 6.2, where a section of the detector layout and the tracks and calorimeter showers are shown (the various colors correspond to different particle types).

6.1.2 Reconstruction using CORAL

After we obtain the randomly generated events in the first step, we need to reconstruct the events. In order to reconstruct the interaction of particles in a generated event with the detector, the CORAL program is used by the COMPASS Collaboration.

Specifying in an option file the various configuration parameters, like the detector geometry and so on, which depends on the year of data taking and

physics program conducted, the number of events reconstruction, the list of physical process that a charged or neutral particle undergoes travelling through the spectrometer, depending on the particle nature and energy, all these informations result in a so called ZEBRA file[6], which contains the raw data, like position of the hits in tracking detectors, time characteristic of the signals, energy deposit of the hadronic and electromagnetic shower in the calorimeters, Cherenkov radiation in the RICH, and so on[53]. These raw data are subsequently elaborated by the event reconstruction program CORAL, and the reconstructed events are finally stored in mDST files, in analogy to real data[6].

In order to use CORAL, we need to specify in an option file what kind of detector configuration has been used by COMGEANT. To speed up the simulation, a second possibility forseen by the programs was employed: simulated detector information was not written in the ZEBRA files, instead a so called pipe, based on a $FIFO_5$ mechanism, sent the COMGEANT output for the single event directly to CORAL for reconstruction. This method had the advantage of saving time and space on computer storage system without loss of precision in the MC simulation[42]. The resulting mDSTs with the reconstructed events at the end of the MC chain, were ready for use in the analysis of the MC data, performed with the same routines already written for real data analysis[6]. The binary file from the event generator containing the event description on an event-by-event basis constitutes the input for COMGEANT[19].

In order to reconstruct Monte Carlo simulations with same CORAL version as for real data and same material maps, the detectors.dat which include radiation length for detectors outside material maps, per plane efficiencies and detector position should be known[6]. We can get the vertex information, position, time and track information from the homepage of COMGEANT. As for the particle type, in this thesis $\eta, \pi^-, \pi^+, \pi^0$ will be cared about.

6.1.3 The full MC and fast MC

The only detection elements in the COMPASS experiment implemented in the photon acceptance Monte Carlo selection, sometimes also referred to as "Fast Monte Carlo", are the two electromagnetic calorimeters ECAL1 and ECAL2 and the 3.14m long steel tube of the RICH detector that plays a major role in the acceptance of events with photons (more details see[10]).

The ECALs are implemented as simple plane areas perpendicular to the

beam line and located at the center of the calorimeters(see section 2.6). An event is accepted when both photons hit any of the two planes.

With the known 3-momentum of the gammas from the generator one can easily calculate their hit points in the ECAL planes according to formula 6.1, with $\vec{r}_h$ as the position vector of the hit point, $\vec{r}_v$ the generated vertex position, $\vec{p}_r/|\vec{p}_r|$ the direction of the photon's momentum and κ the distance between the vertex and the hit point.

$$\vec{r}_h = \begin{pmatrix} r_x \\ r_y \\ r_z \end{pmatrix} = \kappa \vec{p}_r / |\vec{p}_r| + \vec{r}_v \tag{6.1}$$

To simulate the threshold of the calorimeters an event is neglected if a photon hits ECAL1 and has an energy smaller than 1GeV or if a photon travels in ECAL2 and its energy is less then 4GeV.

6.2 Event Generation

Many different event generators are used within the Collaboration, every of which tuned to a particular channel under investigation, because of the vast physics program of COMPASS[64].
An event generation consists of a ROOT script written in C++, whose task is to write in its output file the particle identity and its 4-momentum for all the particles in an event - on an event by event basis[19]. The processes to simulate are for the subject of the present thesis:
1) The scattering and diffractive excitation of the incoming beam π^- on the proton at rest in the laboratory frame;
2) The production of the X=$\pi^- f_1$ system in a given kinematic range, similar to real data;
3) The decay X $\rightarrow \pi^- + f_1$;
4) The $f_1 \rightarrow \pi^-\pi^+\eta$;
5)The $\eta \rightarrow \gamma\gamma$;

Information about a single event is thus written in the output file describing the reaction in the interaction point. Due to the two subsequent decays $X \rightarrow \pi^- f_1 \rightarrow \pi^-\pi^-\pi^+\eta(\gamma\gamma)$, whose description is best suited in the rest frame of each one of the decaying particles, further complications must be faced. Therefore much attention was paid to the series of rotations and boosts which must be performed going from the rest frames to the laboratory frame, which is the default frame for the further simulation of an event. All these

decay processes were simulated to be isotropic, for a precise determination of the acceptance effect on the reconstructed angular distributions[19].

The first thing that the generator code does is randomly choosing a vertex position. For the z-component a simple random number is uniformly generated in the target area between -70cm and -30cm(see section 2.1). With a routine programmed the resulting position vector for the primary vertex is used to interpolate a possible direction of the beam. The x, y and z component is randomly picked out of a histogram showing the vertex distribution in 2008 COMPASS data.
As for the generation of the vertex, we can see the figure 6.3.

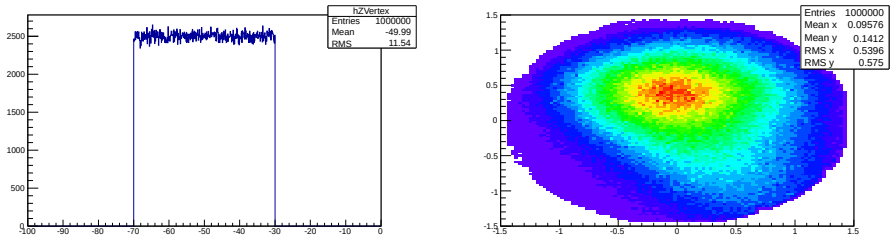

Figure 6.3: Generated vertex distribution: the left one is the z-distribution; the right one is the xy distribution. For the z-component a random number is generated in the target area(-70cm, -30cm).

With the generated 1 million events we get the X($\pi^- f_1$) mass distributions in the mass range [1,3.5] GeV as shown in figure 6.4.

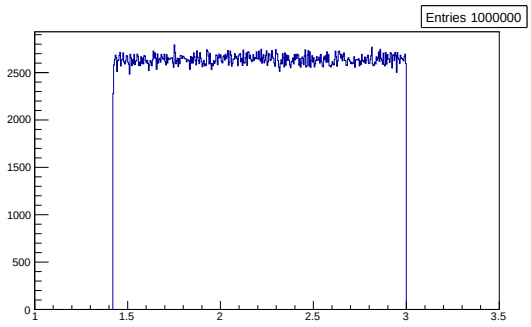

Figure 6.4: The generated of X($\pi^- f_1$) mass distribution in the G-J frame

Here generate the angular distribution of f_1 in the G-J frame with 1 million random events. The figure 6.5 shows the $\cos\theta_G$ distribution with the [-1,1] range. The ϕ_G distribution has the range [-π,π].

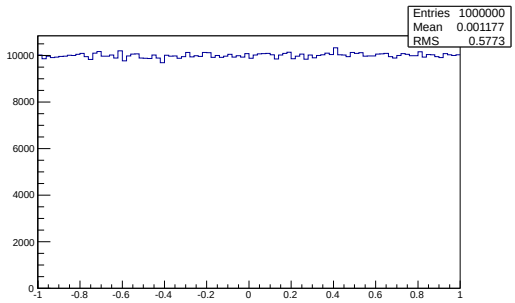

Figure 6.5: The generated $\cos\theta_G$ distribution in the G-J frame.

In figure 6.6 the generated energy vs angle of γ in the X system.

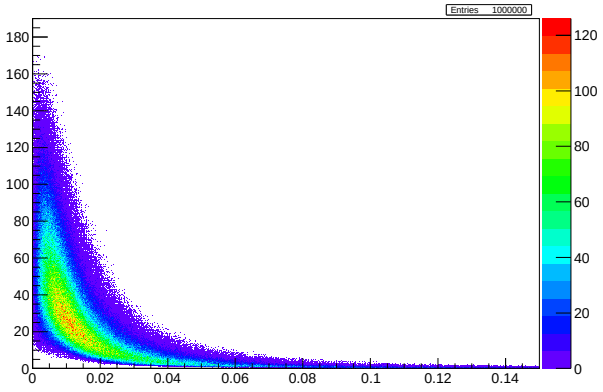

Figure 6.6: The generated energy vs angle of γ.

After generate 1 million events in the X rest system, in order to use COMGEANT and CORAL, we need to rotate and boost the Lorentz vectors into the laboratory system.

6.3 Event accepted by fast MC

Figure 6.7 - 6.11 show the accepted distributions of X=$\pi^- f_1$ where the fast MC was used. In the figure 6.7 we present the $\pi^- f_1$ mass distributions accepte by fast MC.

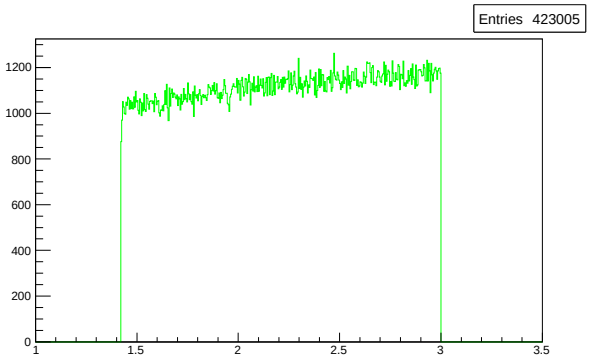

Figure 6.7: The accepted $\pi^- f_1$ mass distribution. The accepted events are 423005. Comparing with the 1 million generated events, the average acceptance is about 42 percent(see section 6.5).

Figure 6.8 is the angular distribution of f_1 in the X=$\pi^- f_1$ system which accepted by fast MC.

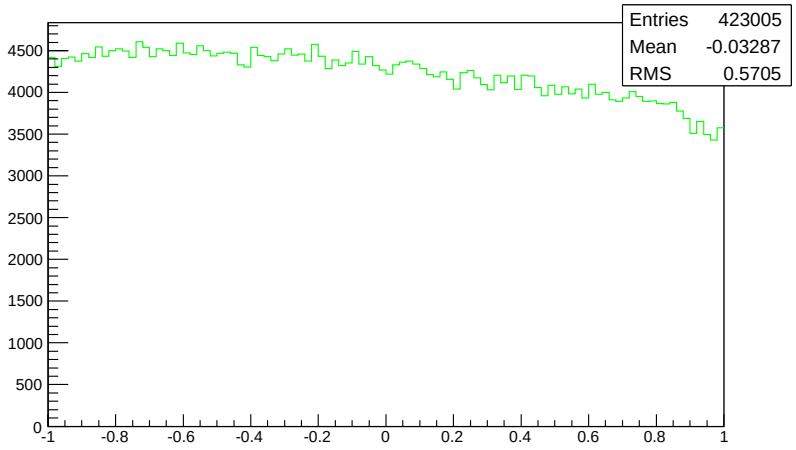

Figure 6.8: The accepted $\cos\theta_G$ distribution in the G-J frame.

Next, we divide the mass of X into 200 MeV/bin from 1.5 to 3.1 GeV.

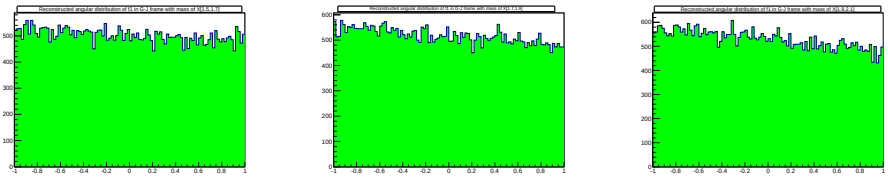

Figure 6.9: The accepted $\cos\theta_G$ distribution of f_1 in the G-J frame. The left plot is in the X mass range from 1.5 to 1.7 GeV; the middle one is in the X mass range from 1.7 to 1.9 GeV; the right one is in the X mass range from 1.9 to 2.1 GeV.

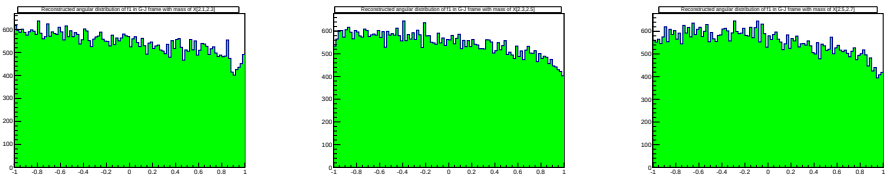

Figure 6.10: The accepted $\cos\theta_G$ distribution of f_1 in the G-J frame. The left plot is in the X mass range from 2.1 to 2.3 GeV; the middle one is in the X mass range from 2.3 to 2.5 GeV; the right one is in the X mass range from 2.5 to 2.7 GeV.

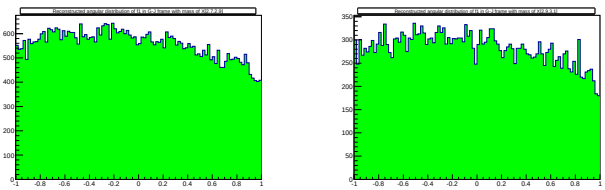

Figure 6.11: The accepted $\cos\theta_G$ distribution of f_1 in the G-J frame. The left plot is in the X mass range from 2.7 to 2.9 GeV; the right one is in the X mass range from 2.9 to 3.1 GeV.

With the MC accepted, we can see in the figure 6.12 where the enery vs angle of γ is plotted that we lose many events at the small angle.

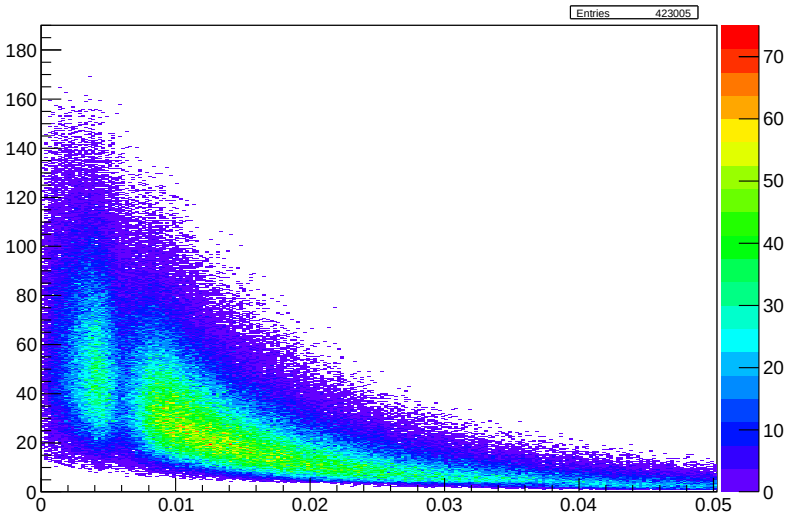

Figure 6.12: The distribution of accepted events as a function of energy vs angle of γ.

From the figure 6.12 we can learn that due to the small ECAL1 gap we lost events(γs) at the angle 0.005 rad, in additional, the RICH pipe contributes to the loss of events with the fast MC.

6.4 Acceptance of fast MC

For every bin i of mass distributions and angular distributions, the acceptance is defined as:

$$A_i = \frac{N_i^{reco}}{N_i^{gen}} \tag{6.2}$$

Here the N_i^{reco} is the bin content for accepted MC data, N_i^{gen} is the MC generated data, A_i is the MC acceptance. N_i^{reco} and N_i^{gen} have the same bins.

The acceptance as a function of the $\pi^- f_1$ mass is shown in figure 6.13.

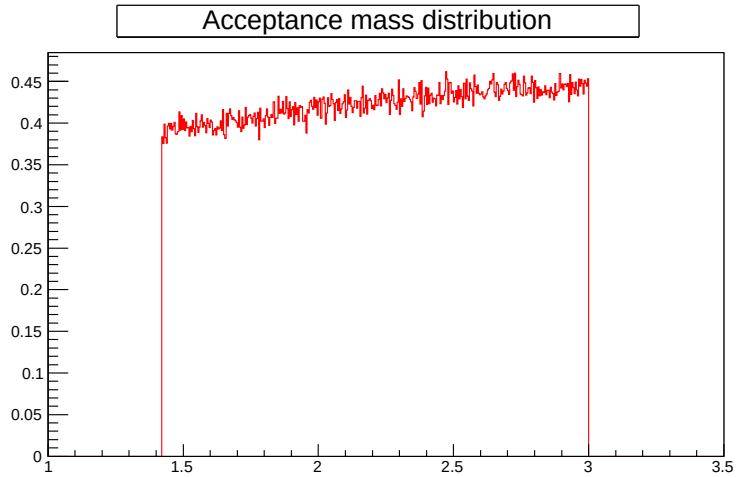

Figure 6.13: The acceptance as a function of $\pi^- f_1$ mass.

Particular attention was paid to the acceptance for the angle θ_G. Figure 6.13 are the angular distribution acceptance of f_1 in the G-J frame of X rest system.

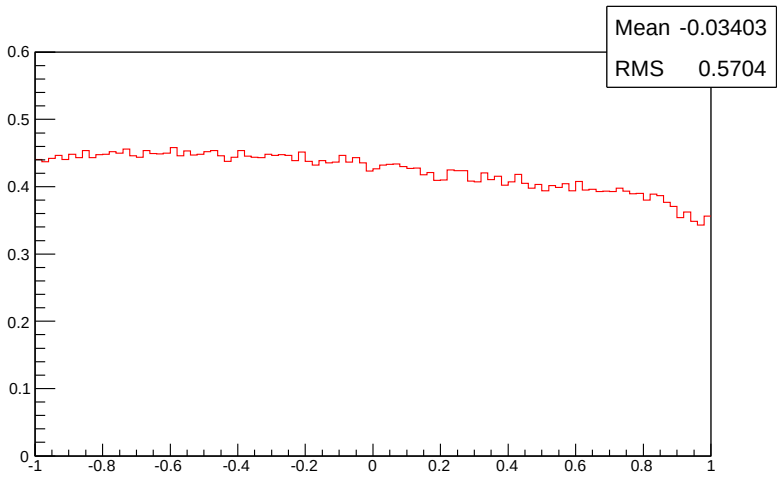

Figure 6.14: The acceptance as a function of $\cos\theta_G$. The acceptance is highest when $\cos\theta$ =-1; and the acceptance is lowest when $\cos\theta$ =1.

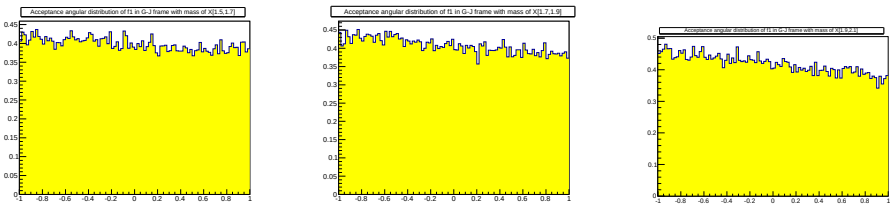

Figure 6.15: The acceptance as a function of $\cos\theta_G$, in different bins of the mass of X. The left plot is in the X mass range from 1.5 to 1.7 GeV; the middle one is in the X mass range from 1.7 to 1.9 GeV; the right one is in the X mass range from 1.9 to 2.1 GeV.

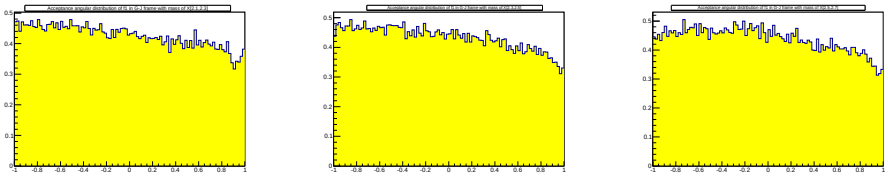

Figure 6.16: The acceptance as a function of $\cos\theta_G$. The left plot is in the X mass range from 2.1 to 2.3 GeV; the middle one is in the X mass range from 2.3 to 2.5 GeV; the right one is in the X mass range from 2.5 to 2.7 GeV.

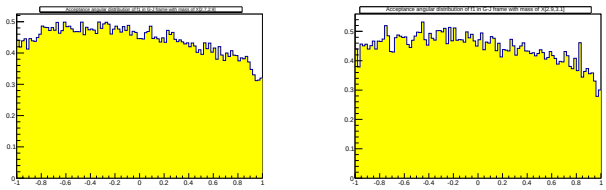

Figure 6.17: The acceptance as a function of $\cos\theta_G$. The left plot is in the X mass range from 2.7 to 2.9 GeV; the right one is in the X mass range from 2.9 to 3.1 GeV.

Comparing these plots we can learn that at higher mass, the angular distribution of f_1 in G-J frame of X system will have lower acceptance when $\cos\theta = 1$. From the formula of Lorentz Boost we can calculate the momentum of π^- and f_1 in the lab system. If the f_1 goes forwards, the momentum of π^- is very low and outside spectrometer acceptance.

Chapter 7

Partial wave analysis

The partial Wave Analysis (PWA) is a technique used in hadron spectroscopy to extract information about the spin-parity and decay properties of resonances produced in hadronic interactions[9]. Typically, these resonances are produced at accelerator experiments by a variety of production mechanisms[9]. At the same time it is one of the best ways to do the search for spin-exotic states[9]. With this technique, a given data set containing final state decay products of some resonances can be exploited and the resonance parameters be determined. Those include the mass, the width(Γ) and the J^{PC} quantum numbers as they have been introduced in chapter 1. In order to identify the spin properties, an evaluation of the angular distributions of the final state particles is the key. The PWA furthermore takes interferences between different, in their masses overlapping, states into account. In fact it is often solely this interference behavior, which leads to the believable discovery of a new resonance.

Depending on the particular production mechanism and reaction chain, different PWA implementations are usually employed. This can be due to computing performance reasons, but also principle physics arguments can play a role[1].

Generally PWA begins with some physics assumptions concerning the reaction process. First of all I will summarize them for the analysis presented in this work and also point out their implications. Furthermore, a PWA is always based on the spin formalism, which employs certain reference frames and decides on the concrete representation of spin states and angular distributions. Therefore I will briefly introduce a very common approach. The computational techniques of the performed PWA[1], namely a mass-independent extended maximum likelihood fit followed by a mass-dependent fit, are de-

tailed at last. All output parameters obtained from the fits are explained and the quality assurance of the whole procedure is discussed.

In this chapter we concentrate on the PWA of $\pi^- f_1$ and subsequent decays. The case of $\pi^- f_1$ to $\pi^-\pi^-\pi^+\eta$ is described here. The purpose is a quantitative determination of the different possible spin-parity contributions J^{PC} for the observed structure.

In this chapter we proceed along these ways. First of all we describe the physics assumptions and implications. Secondly, we present the decay amplitude and production amplitude. Thirdly, we disscus the angular distribution fit. Then we divide mass bin of X into every $50 MeV/c^2$ in order to get the mass-independent partial wave analysis. Last but not the least we present a mass dependent fit.

7.1 Assumptions and Implications

The performed PWA relies on physics assumptions, which are described in this section. They lead to a parametrization of the reaction cross section and are therefore crucial for the whole procedure. Some of the assumptions are connected to the production process and are therefore very specific to the diffractive dissociation case[63]. The one-Reggeon exchange is an example for this. Others like the isobar model are very common and used in most PWA nowadays. As far as possible, the actual impact of each assumption is addressed, whereas some of the technical points have to be resumed later in this chapter again after more details about the analysis have been explained. To provide a basis for the following discussions, figure 7.1 illustrates in a simplified way the diffractive resonance production, isobar model assumed as described in section 1.3.3, focussing on the features relevant for the PWA. In particular all involved quantum numbers and notations are introduced.

In order to be able to exploit the angular distributions of an event in the PWA fit, it is of course a prerequisite that all final state particles have been measured by the experiment. In the most general case this includes not only the resonance decay products but also the recoil particle. However, in the case of diffractive dissociation at high beam energies the recoil can be regarded as completely separated (large rapidity gap)[63]. The π^- projectile only grazes the target and the resonance X is purely produced from the upper vertex. Thus

its properties can in fact be studied from the knowledge of the 4-momenta of the decay products only. In other words, it is assumed that the total reaction cross-section factorizes in products corresponding to a projectile/resonance and a target/recoil vertex without any further final state interactions. The target just acts as a strong interaction partner and provides momentum and angular momentum transfer to the beam projectile[63]. Neither it breaks up nor it is excited and its mass stays therefore the same throughout the whole reaction. Momentum conservation require that the recoil proton is opposite to the X in CMS. This is verified in the data selection and part of exclusively cuts.

Before it is possible to write down a decay amplitude using a particular spin formalism, it has to be defined how the final state particles are grouped to construct the decay chain. The most popular approach, which is followed also by the employed PWA program, is the so-called isobar model(see section 1.3).

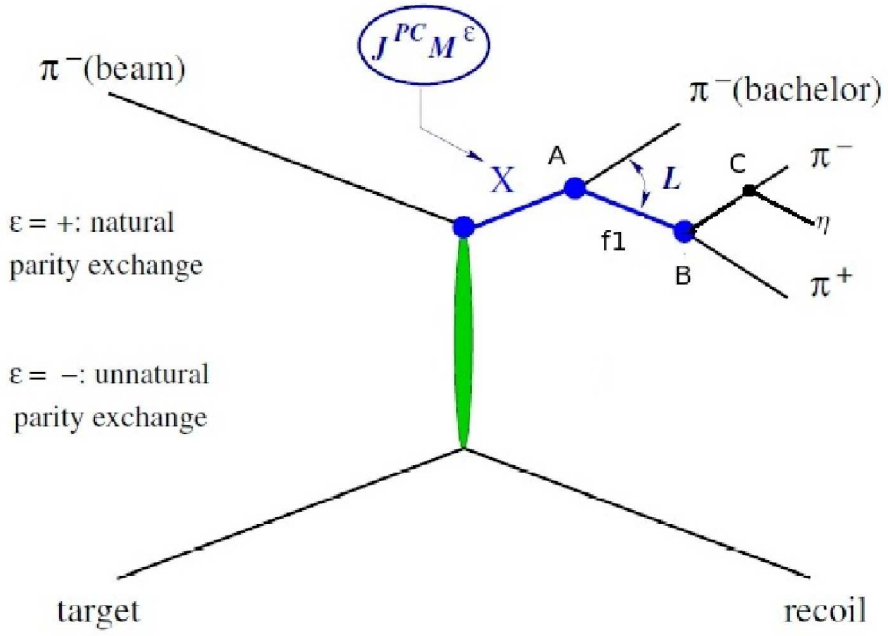

Figure 7.1: Production and decay of the chain $\pi p \to Xp$, $X \to \pi^- f_1$, $f_1 \to a_0\pi$, $a_0 \to \pi\eta$ in the isobar model.

The state X is characterized by $J^{PC}M^{\epsilon}$, where J, P and C are the total spin, parity and charge conjugation. M is the spin projection along the z axis

and ϵ represents symmetry of $\pi^- f_1$ system under reflection in the production plane. Viewed in the terms of some exchange mechanism $\epsilon = +$ corresponds to natural parity exchange and $\epsilon = -$ corresponds to unnatural parity exchange. The natural parity means $\epsilon = P_{ex}(-1)^{J_{ex}}$=1. Here the P_{ex} and J_{ex} are the spin and parity of the exchange trajectory. At high energy the particle which dominates among the exchanged Regge-trajectories("Reggeons") is the flavourless "Pomeron"[56]. The S is the spin of f_1 and L is the orbital angular momentum between π^-(bachelor) and f_1.

The decay at point A is described in the Gottfried-Jackson frame(see section 5.3) which is the rest frame of the $\pi^- f_1$ with the beam direction defining the z-axis and the normal to the production plane defining the y-axis. In this frame the angles of the f_1 (or opposite direction of bachelor pion) are denoted by θ_G and ϕ_G. The decay at point B is described in the helicity frame, the rest frame of the $\pi^-\pi^+\eta$ system with the boost direction to that frame defining the z-axis. The decay of $f_1 \to \pi^+\pi^-\eta$ is a three-body decay. Again in the isobar model this three-body decay is described by subsequent two-body decays $f_1 \to \pi^\pm + a_0^\mp$ or $f_1 \to (\pi^-\pi^+)_S\eta$ and finally $a_0^\mp \to \pi^\mp\eta$ and $(\pi^-\pi^+)_S \to \pi^-\pi^+$.

As already mentioned in terms of exchange reactions, as discussed above, the Pomeron is the most prominent exchange trajectory. It carries angular momentum and helicity and thus the beam pions with $J^P = 0^-$ may be excited to different J^P states X[44]. No isospin or electric charge is transferred from the target to the projectile. It should be emphasized at this point that the performed PWA does not directly take the quantum numbers of the target (recoil) into account. The inserted waves refer only to the state X and its decay. The fact that the (unpolarized) target might have spin (nucleon case) or not (lead case) is only reflected in the number of fit parameters, more precisely in the rank of the spin density matrix[8].

In strong interactions parity is conserved[7]. This is in particular true for the diffractive meson production, and therefore the PWA has to take it into account. It has been a common practice to describe the production characteristics X (see fig. 7.1) in terms of the reflectivity $\epsilon = \mp 1$ quantum number, limiting at the same time the spin projection to values M $\geq$0. This turns out to be a very convenient description, since parity conservation can be translated into the fundamental constraint that waves with opposite ϵ are not allowed to interfere.

A second important, although again not trivial topic connected to the re-

flectivity is its correspondence to the exchanged naturality(see page 75). Since diffractive reactions are dominated by a Pomeron exchange, only ϵ= +1 waves are expected to contribute significantly to the PWA fit[7]. Therefore, from the beginning on, much less ϵ = -1 waves compared to ϵ = +1 waves are considered.

7.2 Wave selection

In the following we discuss the possible properties (quantum number combinations) of the states X which are produced by the diffractive dissociation (excitation) of an incoming beam pion to a resonance X on a proton target, with an elastically recoiling proton. Apart from the mass, these states X are characterized by the spin and parity J_X^P and by the z-projection M_X and the reflectivity ϵ, defined in the Gottfried-Jackson reference system(In order to do not mix with the J_I and J_F, in this section we use J_X and M_X replace the J and M.).In other words, we provide a list of production selection rules imposed by the quantum numbers of the incoming particles, pion and proton, and the particular kinematics and choice of description: $2 \to 2$ reaction: $\pi^- p \to Xp$ at low momentum transfer t, with abs(t) between 0.1 and 1.0 GeV^2 and invariant masses of X below $3GeV^2$. For the choice of a particular final state, i.e. a specific decay of the resonance X, decay selection rules to be derived from the quantum numbers of the final state particles provid further constraints of the possible quantum number combinations for the resonances X. Both, production and decay selection rules help to limit the number of amplitudes to be considered in a partial amplitude analysis.

First we consider the incoming and outgoing system in the cm reference frame (see figure 5.5) under the assumption that we can add all spins and angular momenta in a non-relativistic way. For simplicity and intuitive reasons it is assumed that the orbital angular momentum between π^- and p in the incoming state and between X and p in the outgoing state are larger than the spins of p and X. For peripheral reactions this assumption appears justified.

The projections of both orbital angular momenta to the axes of incoming and outgoing particles which almost coincide at this large energy are zero. For the measurements in 2008/2009 an unpolarized proton target was used. Hence the p spin projection along the chosen z axis is +1/2 or -1/2. Two cases will be considered, one without a spin-flip and the other one with the spin flip of the proton.

The total angular momenta J_I and J_F of all particles in the initial and in the final state are given by the vector sums of the spins of the particles (S_p and $S_{rp} = 1/2$ for the initial and final, recoil proton, $S_{\pi^-} = 0$ for the pion and J_X for the system X) and the orbital angular momenta between the two incoming and the two outgoing particles, L_I and L_F and total angular momenta are conserved ($\vec{J_I} = \vec{J_F}$).

$$\vec{J_I} = \vec{L_I} + \vec{S_{\pi^-}} + \vec{S_p} = \vec{L_F} + \vec{J_X} + \vec{S_{rp}} = \vec{J_F} \tag{7.1}$$

Under the above assumption of large orbital angular momenta this leads to the following relation between the quantum numbers of the involved angular momenta:

$$|L_I \pm S_{\pi^-} \pm S_p| = |L_F \pm S_{rp} + JM_X| \tag{7.2}$$

where JM_X may take all values from $-J_X, -J_X + 1, ...0, ... + J_X$. (Strictly speaking, not all values are allowed. If the spin projections are all zero, some combinations are excluded, due to symmetries and the resulting fact that the Clebsch-Gordan coefficients involved in the sum of spins are = zero, as will be discussed below).

The equations for the total parity, a conserved quantum number as well, of initial and final state are:

$$P_I = P_{\pi^-} P_p (-1)^{L_I} = P_X P_{rp} (-1)^{L_F} = P_F \tag{7.3}$$

Here, P_I and P_F are the parities of the incoming and outgoing state. P_{π^-} and P_p are the parities of π^- and proton. P_X and P_{rp} are the parities of X and recoil proton. Parity is a multiplicative number and the fact has been used that the parity of an orbital angular momentum L is $(-1)^L$.

For completeness, the equations for the spin projections are given here as well, although we will not use it for this first considerations relevant to the production selection rules:

$$M_I = M_{LI} + M_p = M_{LF} + M_X + M_{rp} = M_F \tag{7.4}$$

Here, M_{LI} is the projection of the orbital angular momentum of the incoming state. M_X is the spin projection of the resonance X($\pi^- f_1$) with spin J_X. And M_p and M_{rp} refer to the spin projections of the incoming and recoil proton. M_{LF} is the projection of L_F. M_I and M_F are the total spin projection of incoming and outgoing states.

Consider the case J_X=0 as an example. Since S_{π^-} is 0 one obtains $L_I \pm S_p = L_F \pm S_{rp}$ from formula 7.2. Now, for the case that S_p and S_{rp} have the same sign, which we call non-flip case, we get $L_I - L_F$=0. This has an implication on the intrinsic parity of the produced system X. Using the equations 7.2 for the parities, it is obvious that for this example J_X=0, the parity of X must be -1, since P_{π^-} = -1 and the parity of the proton cancels in the equation. When one considers the spin-flip case (i.e opposite signs of S_p and S_{rp}) one can get $L_I - L_F$=1. So with the formula 7.2 one can also obtain P_X= 1.

As a result of these considerations, the states which are allowed for the production are presented in the table 7.1.

Overlap	J_X	P_X
no-flip	0	-1
no-flip	1	+1
no-flip	2	-1
no-flip	3	+1
flip	0	+1
flip	1	$\pm$1
flip	2	$\pm$1
flip	3	$\pm$1

Table 7.1: Quantum number combinations of the system X which are allowed for the production for the two cases spin-flip and no-flip of the proton. The J_X and P_X are the total spin and parity of X. The J_I and P_I are the total spin and parity of the incoming state.

In the following considerations we wish to include two more quantum numbers: the reflectivity ϵ and the spin projection M_X of the resonance in the Gottfried-Jackson reference system. According to the sometimes very old literature (from the years 1960-1975) the reflectivity is connected with the naturality of the exchanged particle in the reaction as already mentioned above:

$$\epsilon = P_{ex}(-1)^{J_{ex}} \tag{7.5}$$

where P_{ex} is the parity an J_{ex} is spin of the exchanged particle. The proof is easy in the case where all projections of involved angular momenta are zero[2] but difficult for the case where they are not.

Reflectivity is the quantum number of the reflection operator. Reflection of coordinates wrt the production plane (x-z plane) corresponds to the product

of the inversion (parity operator) and a rotation by 180 degrees around the y axis (vertical to the production plane). The reflectivity eigenstates are as follows:

$$| J_X M_X \epsilon\rangle = | J_X M_X\rangle - \epsilon P_X (-1)^{J_X - M_X} | J_X - M_X\rangle \tag{7.6}$$

The variable M_X on the left side of this equation together with ϵ is always ≥ 0.

When M_X=0 then, obviously, $| J_X M_X\rangle = | J_X - M_X\rangle$. Thus, if the product $\epsilon P(-1)^{J-M}$ =+1, the corresponding reflectivity eigenstate is 0. In other words, for the positive reflectivity eigenstates, with ϵ=+1, only quantum number combinations with $P_X(-1)^{J_X}$ =-1 are allowed. Thus the state 1^- for example cannot be produced with M_X=0 and positive reflectivity.

This result can be derived in an intuitive way making use of the exchange diagram shown as: [2]. This diagram (compare fig. 7.1) is some kinds of short notation of the figure underlying equations 7.6 used above. It corresponds to the picture used to illustrate the Gottfried-Jackson system, however with an additional boost along the z direction such that the exchange particle is at rest. With the spin and parity of the exchange particle J_{ex} and P_{ex} and the orbital angular momentum L between the incoming π and the outgoing system X and the $J_X^{p_X}$ of X, we obtain the simple equation for the resulting spin of X:

$$\vec{J_X} = \vec{L} + \vec{J_{ex}} \tag{7.7}$$

since the spin of the pion is zero. For the parity, one gets:

$$P_X = P_{\pi^-}(-1)^L P_{ex} = (-1)^{L+1} P_{ex} \tag{7.8}$$

Note that in this reference system the projection of L can only be zero. Thus any spin projection can only come from the exchanged particle. Now assuming M_{ex} =0 and that the exchanged particle has positive naturality, i.e. $P_{ex}(-1)^{J_{ex}}$ = +1, one can derive the possible values of $J_X^{p_X}$. This has been done for values $J_X^{p_X}$: 0^+, 1^-, and 2^+, and allowing for all possible values of L.

In these combinations of spin of the exchange particle and the orbital angular momenta, the symmetry properties of the Clebsch Gordan coefficients enter since we have to consider the sum of two spins (orbital angular momentum L and J_{ex}. For instance, combining a $J_{ex} = 1$ with an L=1 the relevant Clebsch-Gordan coefficient is zero. This excludes the possibility of producing an X

with $J^p_X = 1^-$ with $M_X = 0$. The result is shown in Table 7.2: For $M_X = 0$ only states X with unnatural spin parity combination can be produced, in agreement with the considerations above, for the case of non-spin-flip.

For $M_{ex} = 1$ almost all states except $J^{p_X}_X = 0^+$ are allowed, again in agreement with the results from the simple considerations involving spin flip. It is therefore suggestive to associate spin flip with an M_{ex}= 1 of the exchange particle.

J^P_X	ϵ	M_X
$0^-, 1^+, 2^-, 3^+...$	+1	0
$1^+, 2^-, 3^+, 4^-...$	+1	1
1^-,$2^+, 3^-, 4^+...$	+1	1

Table 7.2: The $J^P_X M^\epsilon_X$ states of the wave selection. These 1^-, 2^+, 3^- states require M_X =1 for the natural parity exchange.

So far we have shown that with the simplifying considerations for the case M_X =0 and assuming the exchange of particles with a natural spin-parity combination only states X with an unnatural spin parity can be produced if only reflectivity eigenstates with positive ϵ contribute. Thus, these arguments justify our choice of (production) allowed quantum numbers for the state X for the cases of M_X =0.

Former data analyses have shown that the partial waves with negative reflectivity ϵ and/or spin projection $M_X > 1$ are much suppressed and, as mentioned, it has been shown that the production of negative reflectivity eigenstates is associated with the exchange of an unnatural spin parity combination. In other words, it make sense to justify the neglect of partial amplitudes with negative reflectivity and M_X =1[63]. Therefore, only states with $\epsilon = +1$ are taken into account.

In summary, the series of quantum numbers $J^P = 1^+, 2^-, 3^+, 4^-$ and so on is consistent with both $M_X = 0$ and = 1. For 0^-, since the projection M_X is always $\leq J$ the spin, only $M_X = 0$ is possible. States with $J^P = 1^-$, $2^+, 3^-, 4^+$ and so on require $M_X = 1$ if at the same time $\epsilon = +1$. This is independent from the fact that 1^- and 3^- are spin-exotic in the sense that they can not come from a $q\overline{q}$ system.

Next, the decay selection rules imposed by the quantum numbers of the two particles in the final state are derived. The final state of this thesis, X= $\pi^- f_1$, has isospin I = 1, from the π^-. The isospin of the f_1 is zero. This state X is not an eigenstate of C(the charge conjugation eigenvalue). When we quote C, it is the C-parity of the corresponding neutral final state, for example the state $\pi^0 f_1$, which is indeed an eigenstate of C, since both f_1 and π_0 are eigenstates of C. The C parity and G parity are related by the relation C = G$(-1)^I$, where I is the isospin of the system we transform. G applied to pions is -1, G applied to f_1 is +1. So G of the final state $\pi^- f_1$ is -1, because the total G parity is multiplicative. Since C = $G(-1)^I$ and I = 1 of the $\pi^- f_1$ state, the total isospin must be 1 and the C of the neutral final state is +1. Thus all of the possible states X will carry the label C=+1.

For the decay of X into $\pi^- f_1$, the following formulas for the relations between spin J_X and parity P_X of X and of $\pi^- f_1$ apply, corresponding to the equations 7.9 and 7.10 for the decay of the exchange particle into beam pion and X:

$$|L-1| \leq J_{\pi^- f_1} = |S_{\pi^-} \pm S_{f_1} \pm LM| \leq L+1 \tag{7.9}$$

and

$$P_{\pi^- f_1} = P_{\pi^-} P_{f_1} (-1)^L = (-1)^{L+1} \tag{7.10}$$

where LM takes all values from -L to +L. Thus, we can get the table 7.3.

L	J_X^{PC}
0	1^{-+}
1	0^{++}, 1^{++}, 2^{++}
2	1^{-+}, 2^{-+}, 3^{-+}
3	2^{++}, 3^{++}, 4^{++}

Table 7.3: The possible J_X^{PC} combinations of X allowed from the decay of into $\pi^- f_1$ with the different orbital angular momentum L. The J_X^{PC} list with the different orbital angular momentum L. The J_X, P and C are the total spin, parity and charge conjugation of the resonance X($\pi^- f_1$).

Applying both, the production and decay selection rules derived above, we can get the final wave selection as shown in table 7.4.

$J_X^{PC} M_X^{\epsilon}$	Wave	L
$1^{-+}1^{+}$	S	0
$1^{++}0^{+}$	P	1
$2^{++}1^{+}$	P	1
$1^{-+}1^{+}$	D	2
$2^{-+}0^{+}$	D	2
$3^{-+}1^{+}$	D	2
$2^{++}1^{+}$	F	3
$3^{++}0^{+}$	F	3
$4^{++}1^{+}$	F	3

Table 7.4: The selected waves for the partial wave analysis. Allowed J_X^{PC} for the states of X decaying into the $\pi^- f_1$ channel. Here, L is the orbital angular momentum between π^- and f_1 in the X decay. The J_X, P and C are total spin, parity and charge conjugation of the resonance X($\pi^- f_1$). The M_X is the projection of J_X in the Gottfried-Jackson system.

7.3 Decay Amplitudes and Production Amplitude

Remember the decay amplitude (formula 1.23):

$$A_X = (2L+1)^{1/2} \sum_{\lambda} D^{J_X *}_{M_X \lambda}(\Omega_G)(L0s\lambda|J_X\lambda)(s_{\pi^-}\lambda_{\pi^-}s_{f_1} - \lambda_{f_1}|s\lambda)F_L(p)a_{Ls}A_{\pi^-}A_{f_1} \tag{7.11}$$

We consider a state X with mass $m_{\pi^- f_1}$ which has spin J=J_X with z projection M=M_X. This state X decays to π^- and f_1. Here x_1 =π^-, hence (s_1, λ_1)=(s_{π^-}, λ_{π^-}) and x_2 =f_1, hence (s_2, λ_2) = (s_{f_1}, λ_{f_1}). In the rest system of X the π^- and f_1 have a breakup momentum $\vec{p}$ and relative orbital angular momentum L.

For the list of possible J^{PC} values as shown in the table 7.4, we can calculate the factors $(L0s\lambda|J\lambda)$ for the three possible spin projections λ(in helicity) of X. Here we just list five J^{PC} states with J < 3.

L	J^{PC}	$\lambda=-1$	$\lambda=0$	$\lambda=1$
0	1^{-+}	1	1	1
1	1^{++}	$\sqrt{1/2}$	0	$\sqrt{1/2}$
1	2^{++}	$\sqrt{1/2}$	$\sqrt{2/3}$	$\sqrt{1/2}$
2	1^{-+}	$\sqrt{1/10}$	-$\sqrt{2/5}$	$\sqrt{1/10}$
2	2^{-+}	$\sqrt{1/2}$	1	-$\sqrt{1/2}$

Table 7.5: The possible value of the factor $(L0s\lambda|J\lambda)$ when we set different L and J ,P for the three possible helicities λ of X.

The amplitude for the 1^{++} case, as an example, is therefore(see page 17) if we take M=0 according to table 7.4.

$$A_X(1^{++}) = \sqrt{3}[\sqrt{1/2}D^1_{0-1}F_L(p)a_{Ls}A_{\pi^-}A_{f_1} + \sqrt{1/2}D^1_{01}F_L(p)a_{Ls}A_{\pi^-}A_{f_1}] \tag{7.12}$$

Here the production factor a_{Ls} only depends on the mass of X. As for the f_1 decay, the amplitude $A_{f_1}(\tau)$ is for both branches, the decay via πa_0 and the decay via $(\pi^-\pi^+)_S\eta$:

$$A_{f_1}(\tau) = \sqrt{2+1}\sum_{\lambda'=0}^{0} D^{J*}_{\lambda\lambda'}(\Omega_H)(1000|10)(0000|00)F_L(p_{f_1})a_{10}BW(m_{f_1})A_{x_1}A_{x_2} \tag{7.13}$$

$$= \sqrt{3}D^{1*}_{\lambda 0}(\Omega_H)F_L(p_{f_1})a_{10}BW(m_{f_1})A_{x_1}A_{x_2} \tag{7.14}$$

$$\propto D^{1*}_{\lambda 0}(\Omega_H) \tag{7.15}$$

Where x_1 and x_2 are either $a_0^\pm$ and $\pi^\mp$ or $(\pi^-\pi^+)_S$ and η and a_{10} is a constant production factor. The mass dependence of the production amplitude is in the Breit-Wigner amplitude $BW(m_{f_1})$ and the $D^{1*}_{\lambda 0}(\Omega_H)$ function where Ω_H = (θ_H, ϕ_H, 0). Here the $\lambda^{'}$ is the sum projections of two child particles of f_1 decay in helicity frame which just can be 0. All the child particles from the f_1 decay into the $\pi^\pm a_0^\mp$ or $(\pi\pi)_s\eta$ are spinless. So the decay amplitudes of two child isobars are constants with respect to angles.

The contribution of resonances with $J^{PC}M^\epsilon$ are listed in table 7.6.

L	$J^{PC}M^{\epsilon}$	Amp($\sum_{\lambda=-1}^{1} D^{J*}_{M,\lambda}(\Omega_G)D^{1}_{\lambda,0}(\Omega_H)$)
0	$1^{-+}1^{+}$	$\sum_{\lambda=-1}^{1} D^{1*}_{1\lambda}D^{1*}_{\lambda 0}C_{\lambda}(J^{PC})$
1	$1^{++}0^{+}$	$\sum_{\lambda=-1}^{1} D^{1*}_{0\lambda}D^{1*}_{\lambda 0}C_{\lambda}(J^{PC})$
1	$2^{++}1^{+}$	$\sum_{\lambda=-1}^{1} D^{2*}_{1\lambda}D^{1*}_{\lambda 0}C_{\lambda}(J^{PC})$
2	$1^{-+}1^{+}$	$\sum_{\lambda=-1}^{1} D^{1*}_{1\lambda}D^{1*}_{\lambda 0}C_{\lambda}(J^{PC})$
2	$2^{-+}0^{+}$	$\sum_{\lambda=-1}^{1} D^{2*}_{0\lambda}D^{1*}_{\lambda 0}C_{\lambda}(J^{PC})$
3	$3^{++}0^{+}$	$\sum_{\lambda=-1}^{1} D^{3*}_{0\lambda}D^{1*}_{\lambda 0}C_{\lambda}(J^{PC})$
3	$4^{++}1^{+}$	$\sum_{\lambda=-1}^{1} D^{4*}_{1\lambda}D^{1*}_{\lambda 0}C_{\lambda}(J^{PC})$

Table 7.6: The connection between the decay amplitude of $X(J^{PC}M^{\epsilon})$ and D functions when we set different L, J ,P and M. In this table M is the projection of X in the G-J frame, λ is the sum projections of f_1 and π^- in the G-J frame. $C_{\lambda}(J^{PC})$ are the parameters which have different values according to the J^{PC}, λ and the masses of X, f_1, a_0, $(\pi\pi)_S$.

Assuming for simplicity and didactic reasons that the decay chain of X to the final state proceeds through steps where all isobar are uniquely defined, for instance $X \to f_1\pi^- \to (\pi\pi)_S\eta\pi^-$, all the angles Φ_G and Φ_H are uniquely defined, then equation 7.11 can be written as 7.16-7.18 where constants like $\sqrt{2L+1}$, a_{Ls} and A_{π} have been contributed into the constants a_1, a_2, a_3. From the above analysis we know that when λ=-1, 0 and 1. We can get the decay amplitude $A_X(J^PM,\tau)$ as:

$$A_X(J^PML,\tau) = a_1 D^{J*}_{M-1}(\Omega_G)D^{1*}_{-10}(\Omega_H)(L0s-1|J-1)F_L(p) \quad (7.16)$$
$$+ a_2 D^{J*}_{M0}(\Omega_G)D^{1*}_{00}(\Omega_H)(L0s0|J0)F_L(p) \quad (7.17)$$
$$+ a_3 D^{J*}_{M1}(\Omega_G)D^{1*}_{10}(\Omega_H)(L0s1|J1)F_L(p) \quad (7.18)$$

Using the relation between D-functions and spherical harmonics:

$$D^{\ell}_{m0}(\alpha,\beta,0) = \sqrt{\frac{4\pi}{2\ell+1}}Y^{m*}_{\ell}(\beta,\alpha), \quad (7.19)$$

the three D-functions for the different λ can be calculated as:

$$D^{1*}_{-10}(\Omega_H) = \sqrt{\frac{4\pi}{2+1}}Y^{-1}_{1} \propto \sin\theta_H e^{-i\phi_H} \quad (7.20)$$

$$D^{1*}_{00}(\Omega_H) = \sqrt{\frac{4\pi}{2+1}}Y^{0}_{1} \propto \cos\theta_H \quad (7.21)$$

$$D^{1*}_{10}(\Omega_H) = \sqrt{\frac{4\pi}{2+1}} Y^1_1 \propto \sin\theta_H e^{i\phi_H} \tag{7.22}$$

Therefore, the amplitude $A_X(J^{PC}M, \tau)$ for the decay amplitude of X becomes:

$$A_X(J^P M, \tau) = T_1 D^{J*}_{M-1}(\Omega_G) \sin\theta_H e^{-i\phi_H} + T_2 D^{J*}_{M0}(\Omega_G) \cos\theta_H + T_3 D^{J*}_{M1}(\Omega_G) \sin\theta_H e^{i\phi_H} \tag{7.23}$$

The Ω_G are the angles (θ_G, ϕ_G) in the G-J frame and ϕ_H and θ_H are the angles which describe the f_1 decay in the helicity frame. The M is the spin projection of X in the G-J frame and J is the total spin of X. T_1, T_2, T_3 are production of constants and the production parameters. The latter have to be determined by the PWA-fits to the data.

Now changing to the reflectivity basis:

$$A^{\epsilon}_X(J^P ML, \tau) = \eta(M) \left[A_X(J^P ML, \tau) - \epsilon P (-1)^{J-M} A_X(J^P(-M)L, \tau) \right] \tag{7.24}$$

where P is the parity of resonance X, L is the orbital angular momentum. $\eta(M=0)$=1/2, $\eta(M>0)$=$\sqrt{\frac{1}{2}}$, $\eta(M<0)$= 0.

Let us take the S wave (L=0 for the X-decay, see table 7.4) for example. The $J^{PC}M^{\epsilon}$ of this wave is $1^{-+}1^+$, then with ϵ=1, $\epsilon P(-1)^{J-M}$=-1, so we get the amplitude $A_X(1^{-+}1^+, \tau)$ as:

$$A^{\epsilon}_X(1^{-+}1^+, \tau) = A_X(1^{-+}1, \tau) + A_X(1^{-+}(-1), \tau) \tag{7.25}$$

$$= T_1 D^{1*}_{1-1}(\Omega_G) \sin\theta_H e^{-i\phi_H} + T_2 D^{1*}_{10}(\Omega_G) \cos\theta_H + T_3 D^{1*}_{11}(\Omega_G) \sin\theta_H e^{i\phi_H} \tag{7.26}$$

$$+ T_1 D^{1*}_{-1-1}(\Omega_G) \sin\theta_H e^{-i\phi_H} + T_2 D^{1*}_{-10}(\Omega_G) \cos\theta_H + T_3 D^{1*}_{-11}(\Omega_G) \sin\theta_H e^{i\phi_H} \tag{7.27}$$

$$= T'_1(\cos\phi_G - \cos\theta_G \sin\phi_G) \sin\theta_H e^{-i\phi_H} + T'_2 \sin\theta_G \cos\theta_H \sin\phi_G \tag{7.28}$$

$$+ T'_3(\cos\phi_G - \cos\theta_G \sin\phi_G) \sin\theta_H e^{i\phi_H} \tag{7.29}$$

$$= [0](\cos\phi_G - \cos\theta_G \sin\phi_G) \sin\theta_H \cos\phi_H + [1] \sin\theta_G \sin\phi_G \cos\theta_H \tag{7.30}$$

Here we assumed that the $T'_1 = T'_3$, because the projection should have the same probability for -1 and 1.

We can know from the function 7.30, the decay amplitude as a function of $\cos\phi_H$ when we integrate over θ_G, ϕ_G, θ_H. The result($\sim \pm\cos\phi_H$) agrees

with the ϕ distribution of f_1 in helicity frame(see fig. 5.11). For the general case, the observed differential intensity as a function of m_X and $J^{PC}M^{\epsilon}$ is then written in terms of reflectivity basis as[59]:

$$I(m_X, \tau) = \eta(\tau) \sum_{\epsilon} |\sum_{JML} a_X(J^P M^{\epsilon}, m_X) A_X(J^P M^{\epsilon}, \tau)|^2 \tag{7.31}$$

where $a_X(J^P M^{\epsilon}, m_X)$ is the production amplitude, $A_X(J^P, M^{\epsilon}, \tau)$ is the decay amplitude and $\tau = (\theta_G, \phi_G.\theta_H, \phi_H, m_{f_1})$ is the set of kinematic variables describing the decay of the resonance and isobar. The $\eta(\tau)$ is the acceptance function. In order to account for detector acceptance, Monte Carlo simulations were used to find the acceptance function $\eta(\tau)$ (see chapter 6).

The goal of the PWA is to extract the production amplitudes as a function of m_X by fitting the theoretical intensity (see formula 7.31) to the data, with free parameters $a_X(J^P M^{\epsilon}, m_x)$ to be determined from the fit. For the mass independent fit we divide m_X into 50 MeV/c^2 mass bin which are named m_{X_i}. The $a_{X_i}(J^P M^{\epsilon}, m_X)$ are the possible production amplitudes of X in every 50 MeV/c^2 mass bin. The $A_{X_i}(J^P, M^{\epsilon}, \tau)$ are the possible decay amplitudes of X in every 50 MeV/c^2 mass bin. $I_i(\tau)$ is the intensity of X in every 50 MeV/c^2 mass bin. So we can get the total intensity in every mass bin as:

$$I_i(m_{X_i}\tau) = \eta(\tau) \sum_{\epsilon} |\sum_{JML} (a_{X_i} A_{X_i})|^2 \tag{7.32}$$

After fitting to the data, the resulting complex production parameters of fitting can described by

$$a_{X_i}(J^P M^{\epsilon}, m_{X_i}) = |a_{X_i}(J^P M^{\epsilon}, m_{X_i})| e^{i\phi_i(J^P M^{\epsilon}, m_{X_i})} \tag{7.33}$$

Here the $\phi_i(J^P M^{\epsilon}, m_{X_i})$ is the phase. When we set two waves, we can get the phase motion. In section 7.6 and 7.7 some figures about the intensity and phase will be present.

7.4 Cross section and coherence

So far, it has been neglected that the intensity also depends on the t' variable. And it was assumed that all amplitudes for a given ϵ and coherently, see formula 7.31 and 7.32. The t dependence will be described by a function f_i^{ϵ} where the index i now is a short name for $J^P M$. To introduce a possible incoherence between amplitudes a sum of rank r is introduced. Moreover, each decay amplitude is normalized with the integral of the intensity(amplitude

square) over phase space =1. In a reasonably narrow m bin and $t^{'}$ range, the mass-independent differential intensity after MC accepted can be expressed as:

$$I(\tau, t^{'}) = \sum_{\epsilon} \sum_{r=1}^{N_r} \left| \sum_{i} f_i^{\epsilon}(t^{'}) a_{ir}^{\epsilon} A_i^{\epsilon}(\tau)/N_i^{\epsilon}(m) \right|^2 , N_i^{\epsilon}(m) = \sqrt{\int |A_i^{\epsilon}(\tau)| d\tau} \tag{7.34}$$

Here the a_i^{ϵ} and A_i^{ϵ} are the production amplitude and decay amplitude. The indices i and ϵ denoting different partial waves, characterized by a set of quantum numbers $J^{PC} M^{\epsilon} L$; M is the absolute value of the spin projection onto the z-axis; ϵ is the reflectivity; L is the orbital angular momentum between the isobar and the bachelor pion(see fig.7.1). The different $t^{'}$(see section 5.2) dependence of the differential intensity for M=0 and M=1 states is taken into account by the different functions: $f_i^{\epsilon}(t^{'}) \propto exp(-bt^{'})$ and $f_i^{\epsilon}(t^{'}) \propto t^{'} exp(-bt^{'})$, here the slope b has been obtained from the data by first making fits in slices of $t^{'}$. The normalization factors $N_i^{\epsilon}(m)$ contain angular-momentum barrier factors and phase space factors[63].

The second summation in equation 7.34 incoherently adds several coherent differential intensity terms, in which the same vectors of decay amplitudes A_i^{ϵ} are multiplied with different independent complex vectors a_{ir}^{ϵ} enumerated by r = 1...N_r. The latter are also referred to as production vectors. By summing over r, the spin density with maximal rank N_r can be introduced (one for each reflectivity ϵ):

$$\rho_{ij}^{\epsilon} = \sum_{r=1}^{N_r} a_{ir}^{\epsilon} a_{jr}^{\epsilon} \tag{7.35}$$

and the intensity I can be rewritten accordingly:

$$I(J^P M^{\epsilon}, m, \tau) = \sum_{\epsilon} \sum_{ij} \rho_{ij}^{\epsilon} \bar{A}_i^{\epsilon} \bar{A}_j^{\epsilon *} \tag{7.36}$$

The interference between two partial waves i and j is defined by the non-diagonal complex spin density matrix element ρ_{ij}^{ϵ}.

$$\rho_{ij}^{\epsilon} = R_{ij}^{\epsilon} e^{i\phi_{ij}^{\epsilon}} \tag{7.37}$$

and

$$Coh_{ij}^{\epsilon} = R_{ij}^{\epsilon} / \sqrt{\rho_{ii}^{\epsilon} \rho_{jj}^{\epsilon}} \tag{7.38}$$

Where Coh_{ij}^{ϵ} is the coherence. For rank 1 the coherence is 1 and for rank 2...N_r the coherence is ≤ 1.

7.5 Angular distribution Fit

From the previous sections of this chapter, it can be seen that, regardless of the special angular distribution, for special J, L and M, the angular distribution can be written in a general form, using spherical harmonic function $Y_l^m(\theta, \phi)$.

$$I(\theta, \phi) = \left| \sum_{0}^{l} \sum_{m=-l}^{l} n_l^m Y_l^m(\theta, \phi) \right|^2 \tag{7.39}$$

Here the parameters n_l^m is independent. And for every parameter n_l^m, it should include the real part and imaginary part. From the table 7.2 we know that the m is =0 or 1. After calculated from above formulas, we can get the following equations. Here the parameters [0], [1] ...just have the real part. It means that we take 20 real parameters replace the 10 complex parameters.
From the wave selection rule of the $\pi - f_1$ channel (see table 7.4) we know that the L is smaller than 4 and m is -1, 0 and 1. We divide the mass of $\pi^- f_1$ into bins, here we take the most important mass bin from 1.6 GeV to 1.8 GeV with the mass range of f_1 from 1.25 GeV to 1.31 GeV. Then we can calculate the angular distribution as follows:

$$I(\theta, \phi) = \left| n_0^0 + \sum_{l=1}^{3} \sum_{m=-1}^{1} n_l^m Y_l^m(\theta, \phi) \right|^2 \tag{7.40}$$

$$\begin{aligned} I(\theta, \phi) &= [0] + [1]\cos\theta + [2]\cos^2\theta + [3]\cos^3\theta + [4]\cos^4\theta \\ &+ [5]\cos^5\theta + [6]\cos^6\theta + [7]\sin\theta\cos\phi + [8]\cos\theta\sin\theta\cos\phi \\ &+ [9]\cos^2\theta\sin\theta\cos\phi + [10]\cos^3\theta\sin\theta\cos\phi + [11]\sin^2\theta \\ &+ [12]\sin^2\theta cos^2\phi + [13]\sin\theta\cos^4\theta\cos\phi + [14]\cos^5\theta\sin\theta\cos\phi \\ &+ [15]\cos\theta\sin^2\theta\cos^2\phi + [16]\cos\theta\sin^2\theta \\ &+ [17]\cos^2\theta\sin^2\theta\cos^2\phi + [18]\cos^3\theta\sin^2\theta\cos^2\phi \\ &+ [19]\cos^4\theta\sin^2\theta\cos^2\phi \end{aligned} \tag{7.41}$$

With this function we can do the fit to the angular distribution in the G-J frame as follows.

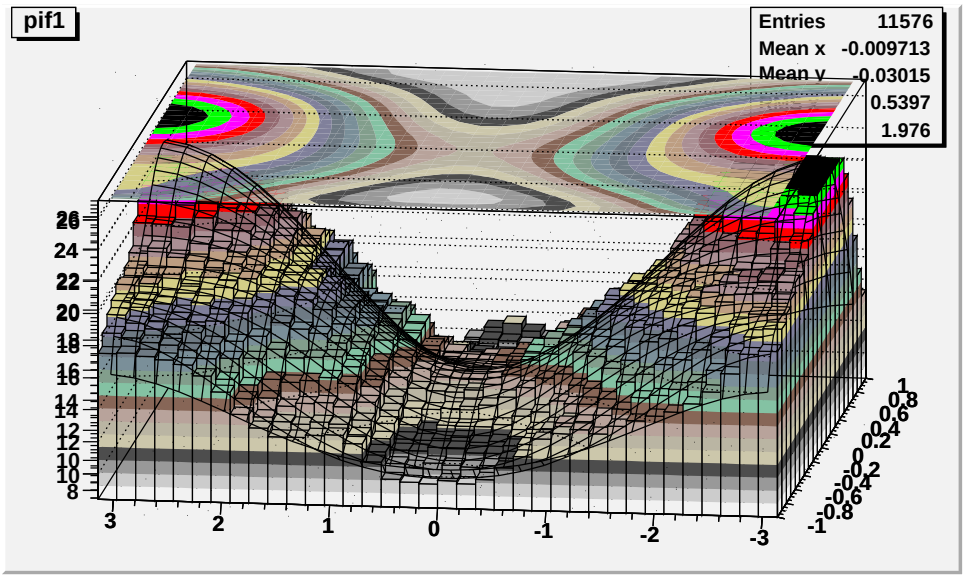

Figure 7.2: The $\cos\theta_G$ vs ϕ_G of f_1 in $\pi^- f_1$ system. The coloured figure is the data for $\pi^- f_1 \to \pi^- + f_1$, the lines correspond to the fit function, the plots is the projection of the fit. A special function as indicated in the figure with x = $\cos\theta_G$ and y = ϕ_G. This angular distribution is in the G-J frame. The mass range of $\pi^- f_1$ is from 1.6GeV to 1.8GeV. The mass range of f_1 is from 1.25GeV to 1.31GeV.

The decay $X \to \pi^- + f_1$ can be seen as a simple two-body decay. From the angular distribution of $X \to \pi^- + f_1$, we can learn about some basic and dominant waves. The fit function of $\cos\theta$ agrees approximately with the function $A - B\cos^2\theta = A - B + B\sin^2\theta$ with the parameters A and B. At the same time, the fit function of ϕ agrees approximately with $(a + b\cos\phi)^2$ with the parameters a and b. Here the a^2 and $(b\cos\phi)^2$ correspond to the wave intensities and $2ab\cos\phi$ corresponds to the interference of two resonances. So the angular distribution dominantly contributed from $\sin^2\theta$(or $\cos^2\theta$) and $\cos^2\phi$. Here θ and ϕ are correspond to θ_G and ϕ_G.

From the formula 7.21, we know $\cos^2\theta$ dominantly corresponds to Y_1^0 and constant mostly corresponds to Y_0^0; from the formulas 7.20 and 7.22, we know $\cos^2\phi$ corresponds to $Y_1^1 + Y_1^{-1}$, $Y_2^1 + Y_2^{-1}$ and $Y_3^1 + Y_3^{-1}$. Taking the table 7.4 into consideration, we can get the simple conclusion that in the $\pi^- f_1$ channel at least $1^{++}0^+$ and $1^{-+}1^+$ waves should be included. More details can been seen from the table 7.7 and 7.8.

Parameter	Value	Error
[0]	1.79354e+01	1.37343e-01
[1]	3.37338e+00	2.21266e-01
[2]	-1.24918e+01	2.77865e-01
[3]	-1.25824e+01	3.24546e-01
[4]	1.37482e+01	3.66095e-01
[5]	8.98647e+00	4.04670e-01
[6]	-1.06210e+01	4.41500e-01
[7]	-5.74683e+00	2.42373e-01
[8]	-5.88497e+00	5.08695e-01
[9]	-5.50260e+00	7.53024e-01
[10]	9.12403e+00	9.86817e-01
[11]	-1.54467e-01	6.55349e-02
[12]	-1.54470e-01	2.81197e-01
[13]	3.88421e+00	1.21234e+00
[14]	1.03144e+00	1.43052e+00
[15]	1.90746e+00	7.04575e-01
[16]	-2.49308e+00	1.41421e+00
[17]	-7.33980e+00	1.18469e+00
[18]	-2.49313e+00	1.72189e+00
[19]	1.61800e+01	2.30945e+00

Table 7.7: The value and error for 20 parameters of the angular distribution(G-J frame) fit for f_1 in the $\pi^- f_1$ system.

From the value and error of table 7.7, we can get the ratio of error to value.

Y_L^m	Function	Value	Error	Error ratio(%)	Parameter
Y_0^0	constant	1.79354e+01	1.37343e-01	0.76	[0]
Y_1^0	$(\cos\theta)^2$	-1.24918e+01	2.77865e-01	2.23	[2]
Y_1^1	$(\cos\theta\sin\phi)^2$	-2.49308e+00	1.41421e+00	56.6	[16]
Y_2^1	$(\cos\theta\sin\theta\cos\phi)^2$	-7.33980e+00	1.18469e+00	16.0	[17]
Y_2^0	$(\cos\theta)^4$	1.37482e+01	3.66095e-01	2.67	[4]
Y_3^1	$(\cos^2\theta\sin\theta\cos\phi)^2$	1.61800e+01	2.30945e+00	14.2	[19]

Table 7.8: The value and Error of the angular distribution(G-J frame) fit, f_1 in $\pi^- f_1$ system.

With the result of table 7.8, which show the value of parameters [0], [2] and [4] are with very low error ratio. They correspond to the harmonic are Y_1^0, Y_2^1 and Y_3^1[27]. We also see that the error which corresponds to Y_1^1 is high in the table 7.7. As for the Y_0^0(S wave), the function is a constant, from the table 7.7, the constant parameter is with a low error ratio, which means we also should include a good S wave in the $\pi^- f_1$ decay.

As for the f_1 decay, we also use the parameters as $X \to \pi^- f_1$ decay. Now we do the fit to the angular distributions of f_1 decay, we can set the parameters as following.

$$I(\theta,\phi) = \frac{\mathrm{d}N}{\mathrm{d}cos\theta \mathrm{d}\phi} = \left| \sum_{l=0}^{1} \sum_{m=-L}^{L} n_L^m Y_L^m \right|^2 \tag{7.42}$$

$$= [0] + [1]\cos\theta + [2](\cos\theta)^2 + [3]\sin\theta\cos\phi \tag{7.43}$$

$$+ [4]\sin\theta\cos\theta\cos\phi + [5](\sin\theta)^2\cos^2\phi \tag{7.44}$$

$$\tag{7.45}$$

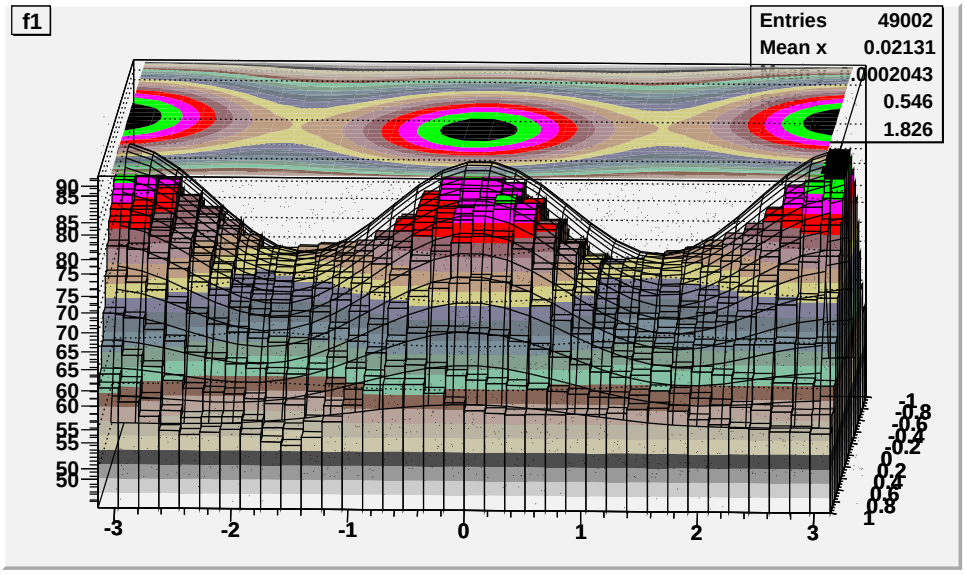

Figure 7.3: The $\cos\theta_H$ vs ϕ_H of a_0 in f_1 system.

The coloured figure is the data for f_1 decay, the lines correspond to the fit function, the plots is the projection of the fit. A special function as indicated in the figure with x = $\cos\theta_H$ and y = ϕ_H. This angular distribution is under the helicity frame. The mass range of f_1 is from 1.25GeV to 1.31GeV.

From the figure 7.3, the fit function of $\cos\theta$ agree with the function $1-\cos^2\theta = \sin^2\theta$(similar as X decay), But the fit function of ϕ agree with $\cos\phi$. According to the formula 7.20-7.22, we can get the function consistent with the sum of Y_1^1 and Y_1^0. Due to the $J_{f_1} = 1 =$ L+0, the L should be 1 which agree with the analysis.

Parameter	Value	Error
[0]	1.25719e+01	1.24042e+00
[1]	3.32216e+00	5.02747e-01
[2]	-1.98068e+01	1.16300e+00
[3]	6.09054e+00	1.16707e+00
[4]	-7.25271e-01	5.52166e-01
[5]	5.05157e+01	3.65217e-01

Table 7.9: The value and error for the parameters of the angular distribution(HL) fit parameters relevant to the decay of a_0 in the f_1 rest system.

7.6 Mass Independent PWA

This section we will show some plots of the mass-independent PWA. It involves a partitioning of the data in bins of the invariant mass m_X of the produced system $X(\pi^- f_1)$. For the analysis of this thesis a bin width of 50 MeV/c^2 have been chosen. For each mass bin one individual extended maximum likelihood fit is then performed using several stages of computational processing. Here we take advantage of the analysis performed by D. Ryabchikov[58] based on data selected by H. Wöhrmann using the fast MC simulation for the acceptance correction.

7.6.1 Intensities

Out of the waves in table 7.4, we present the intensity and phase motion for a selection of waves. All results will be shown in the appendix D. The parameterization of the observed intensity have been shown in section 7.3 with the production amplitudes $a_X(J^P M^\epsilon m_X)$ and decay amplitudes $A_X(J^P M^\epsilon m_X)$. The results of the fit are the complex production amplitudes a_{X_i} in mass bins m_{X_i}(see equ. 7.33). In the following some of the partial intensity $|a_X(J^P, M^\epsilon, m_x)|^2$ $= a_X^*(J^P, M^\epsilon, m_x) a_X(J^P, M^\epsilon, m_x)$ are shown as a function of m_{X_i} and in the next section we will show the relative phase motions which integral t and with

rank 4. The mass-independent PWA has been carried out in 50 MeV/c^2 mass bins and from 1.0 to 3.0 GeV/c^2.

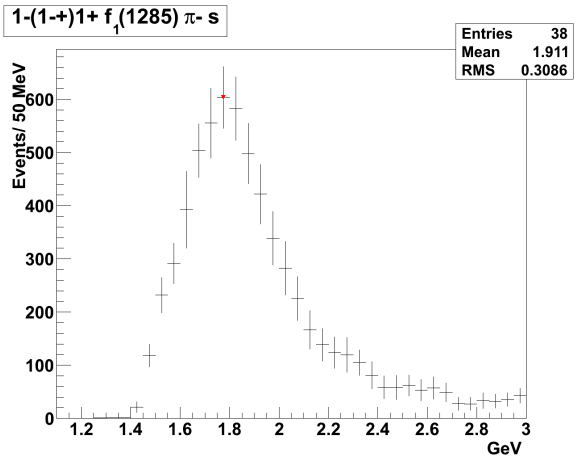

Figure 7.4: The intensity of $1^{-+}1^{+}$ S wave as a function of m_X.

The mass independent fitted intensity distribution for the 1^{-+} S wave is shown in figure 7.4 where the state $I^G J^{PC} M^\epsilon$ of X is $1^-1^{-+}1^+$ with the orbit angle momentum L = 0 (S wave). A peak around the mass 1.76 GeV is clearly seen.

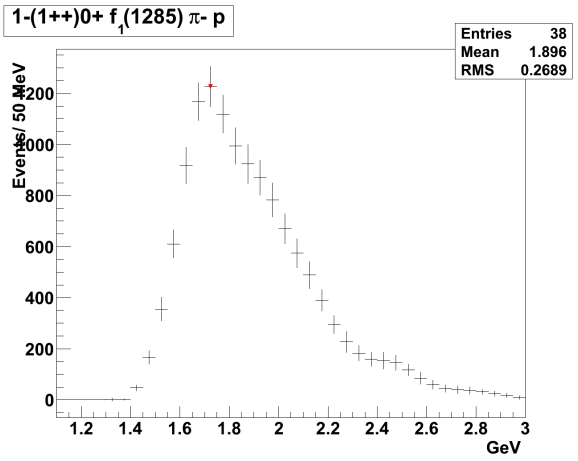

Figure 7.5: The intensity of 1^{++} P wave as a function of m_x.

Figure 7.5 presents the 1^{++} partial wave intensity distribution when the orbital angular momentum is 1. The peak around the 1.7 GeV suggest that

we see a well-known resonance which should be $a_1(1640)$(see PDG). At the same time we can see the amount of a_1 signal is stronger than the π_1 S wave. When compared with other waves, we can know that the a_1 is dominant in this $\pi^- f_1$ channel. From the phase motion which will be discussed in the next section we can support this again.

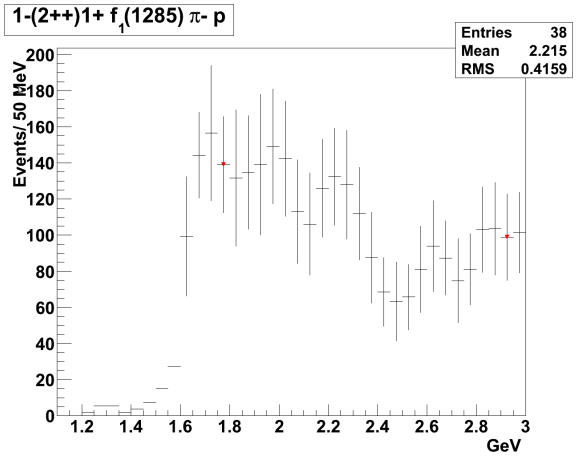

Figure 7.6: The intensity of 2^{++} P wave as a function of m_x.

Figure 7.6 gives the partial intensity distribution of the 2^{++} wave. The result of this wave is so suppressed that we barely support the resonance which was detected in the 2008 data, even if we expect there should be the $a_2(1700)$.

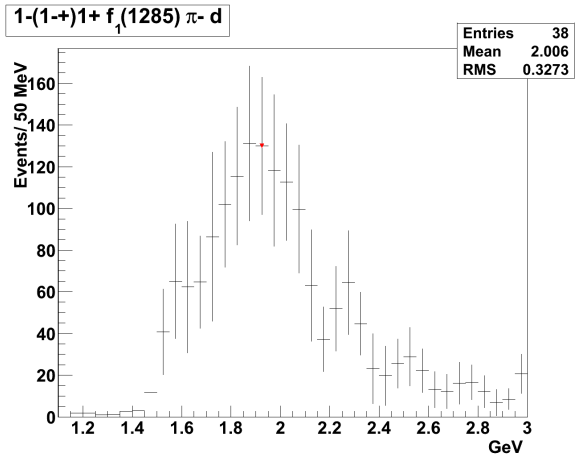

Figure 7.7: The intensity of 1^{-+} D wave as a function of m_x.

Figure 7.7 presents the the 1^{-+} D wave(The orbital angular momentum L is 2) intensity distribution. The error bar is so large that it is not sure this a good signal even if there is a nice peak.

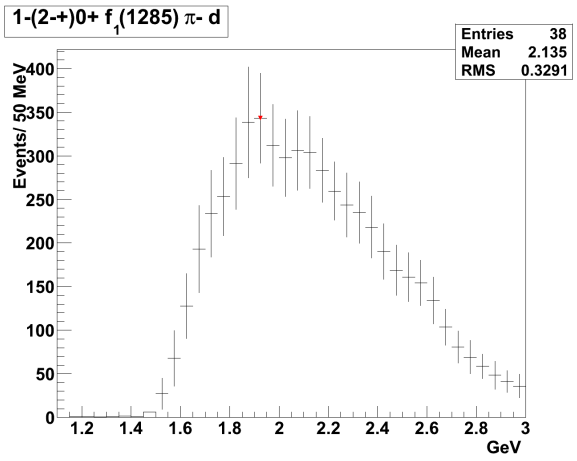

Figure 7.8: The intensity of 2^{-+} D wave as a function of m_x.

The intensity of 2^{-+} D wave is shown in figure 7.8. This partial wave intensity distribution again suggest a resonance. The peak is at 1.9 GeV and the error bars are not large. From the PDG we know this could be $\pi_2(1880)$.

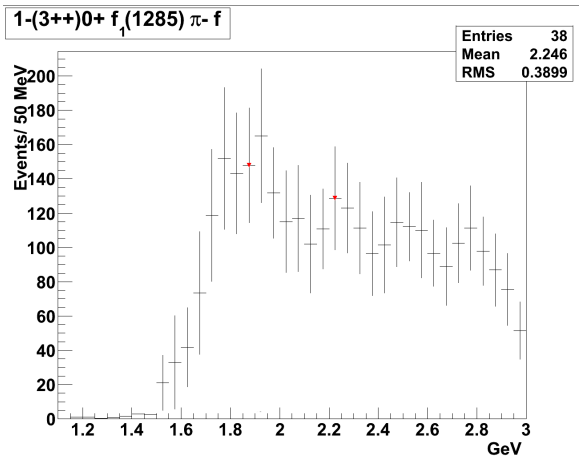

Figure 7.9: The intensity of 3^{++} F wave. F wave is the orbital angular momentum L =3.

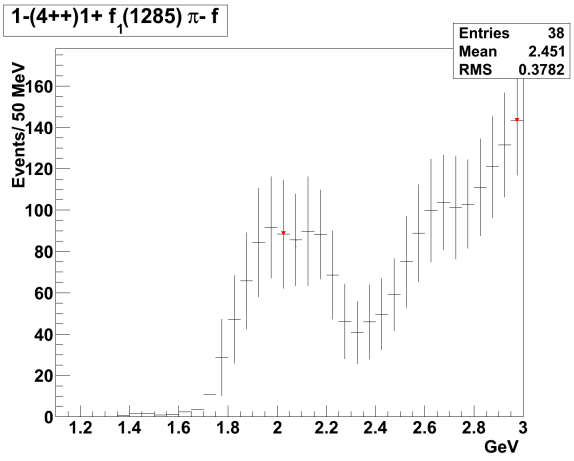

Figure 7.10: The intensity of 4^{++} F wave. A peak around a mass of [1.8, 2.4] GeV can be observed and a significant rise on from 2.4 GeV, suggesting resonance at even higher masses.

7.6.2 Phase motions

These motions describe the relation phase between two amplitude as a function of the mass. From the formula 7.33 we can write:

$$i\phi_i(J^P, M^\epsilon, m_x) = ln\frac{a_{x_i}(J^P, M^\epsilon, m_x)}{|a_{x_i}(J^P, M^\epsilon, m_x)|} \tag{7.46}$$

and for the phase difference between the amplitudes i and j,

$$\Delta\phi_{ij}(m_x) = \phi_j(m_X) - \phi_i(m_X) \tag{7.47}$$

The following figures show the combined terms in the total intensity and phase motion between $I^G J^{PC} M^\epsilon L = 1^-1^{-+}1^+$ S wave and $1^-1^{++}0^+$ P wave, $1^-1^{-+}1^+$ S wave and $1^-2^{-+}1^+$ D wave, $1^-1^{++}0^+$ P wave and $1^-2^{-+}0^+$ D wave. More combined terms and phase motion will be shown in the appendix D. The left-top is the real part of $a_i^* a_j$; the right-top is the imaginary part of the $a_i^* a_j$; the a_i^* is the conjugate of production amplitude a_i; the left-bottom is the phase motion and the right-bottom is the coherence which have been defined in section 7.4(see formula 7.38)[63]. Here the a_i is the $\sum_{r=1}^{4} a_{ir}$.

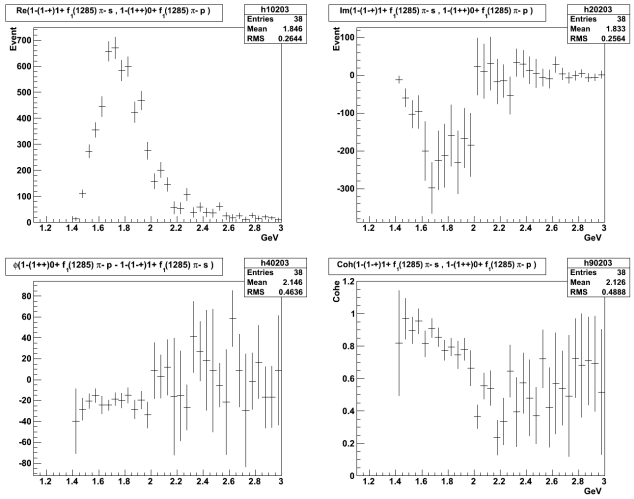

Figure 7.11: The combined terms and phase motion between $1^-1^{-+}1^+$ S wave and $1^-1^{++}0^+$ P wave. The left-top is the real part of $a^*(1^{-+}1^+)a(1^{++}0^+)$ and the right-top is the imaginary part of $a^*(1^{-+}1^+)a(1^{++}0^+)$. The vertical axis is in units of events in the chosen mass bin of 50 MeV/c^2. The left-bottom is the phase motion in the units of degrees from -90° to +90° and the right-bottom is the coherence as defined in formula 7.38. All quantities are plotted as a function of m_x.

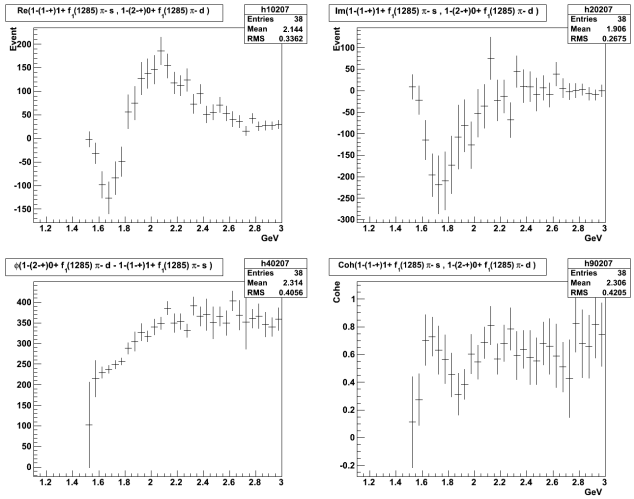

Figure 7.12: The combined terms and phase motion between $1^-1^{-+}1^+$ S wave and $1^-2^{-+}0^+$ D wave. The definition are similar to figure 7.11.

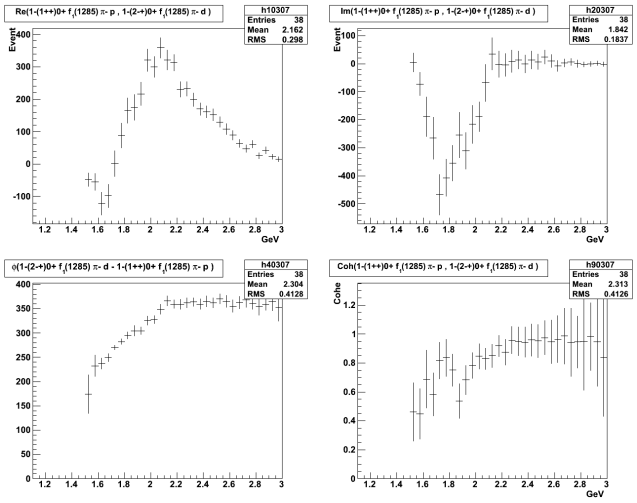

Figure 7.13: The combined terms and phase motion between $1^-1^{++}0^+$ P wave and $1^-2^{-+}0^+$ D wave. The definition are similar to figure 7.11.

7.7 Mass dependent fit

The second step of the partial wave analysis used at this thesis is the mass-dependent fit which is performed by employing the χ^2-method[63].

The mass-dependent fit is based on the outcome of the mass-independent PWA. From the known complex production amplitudes in each mass bin a global model has to be established, which describes the mass-dependence of the spin density matrix.

The global model is usually based on the simple assumption that the systems X with various J^P are the resonances. In more recent years additional non-resonant production have been allowed, like Deck-effect. Resonances are described on the level of amplitudes by Breit-Wigner amplitudes. Thus we do the fit with BW function in order to get the mass and width of the resonances, if they are observed.

The mass and width are used in the BW function(see section 1.2.2). There(in section 1.2.2) the BW intensity fit function has been given which is the square of BW amplitude with fixed width Γ_0.

$$BW^2(m) = BW(m)BW^*(m) = k/((m^2 - M_0^2)^2 + M_0^2\Gamma_0^2). \quad (7.48)$$

Here m is the m_X and k is a constant.. M_0 and Γ_0 are the mass and width of the resonances.

The assumed amplitudes have to describe the summmed intensity, thus not only the individual intensity have to be described correctly by the assumed resonances, but also all the interference term, i.e. relative combined terms and phase motion.

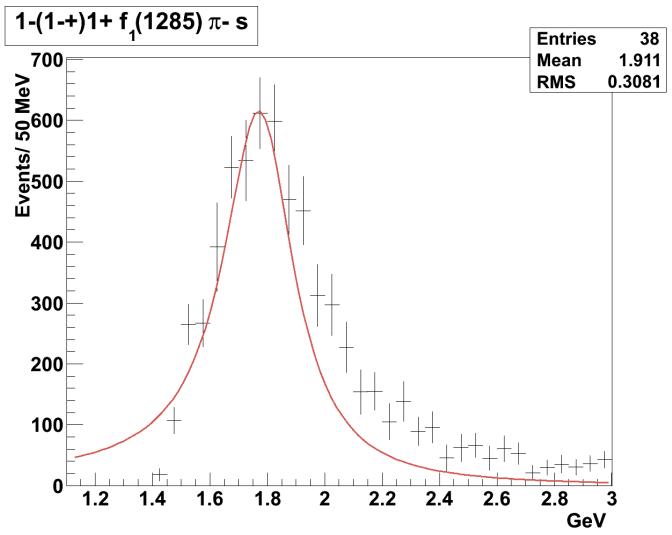

Figure 7.14: The intensity fit of 1^{-+} S wave as a function of m_X. With the fit function of BW, we can see the fit agrees with the mass-independent PWA very well. At the point below 1.4 GeV, little differences come from the phase space. The peak is around 1.76 GeV/c^2. The width is about $300MeV/c^2$.

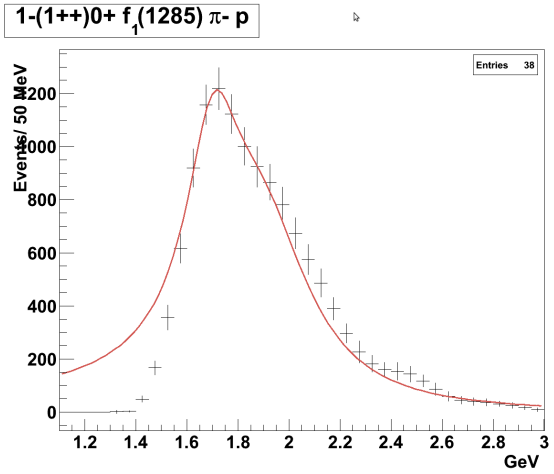

Figure 7.15: The intensity fit of 1^{++} P wave as a function of m_X. With the fit of two BW functions, we can see the fit agrees with the mass-independent PWA mostly, the difference below 1.5 GeV is due to the threshold (phase space factor) are from the phase space. The peaks are around 1.7 and 1.9 GeV/c^2. The widths are about 250 MeV/c^2 and 350 MeV/c^2. From the PDG we can know these agree with the $a_1(1640)$ and $a_1(1930)$.

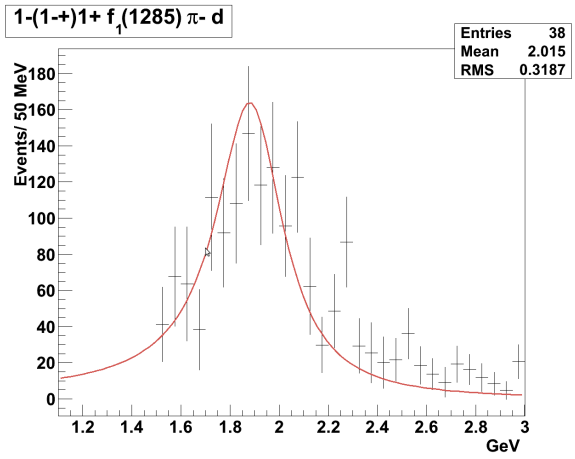

Figure 7.16: The intensity fit of 1^{-+} D wave as a function of m_x. For this 1^{-+} D wave the error bars are so large but the BW fit agrees with the PDG value, the mass peak is around 1.9 GeV, and the width is about 316 MeV.

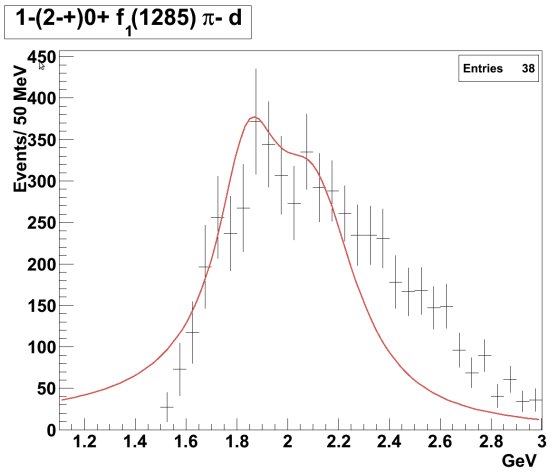

Figure 7.17: The intensity fit of 2^{-+} D wave as a function of m_X. In this BW fit function we have assumed three resonances. The masses are 1.72, 1.84 and 2.1 GeV/c^2 and the widths are 0.25, 0.32 and 0.43 GeV/c^2. From the PDG we know these resonances are $\pi_2(1670)$, $\pi_2(1880)$ and $\pi_2(2100)$. There are some more resonances at higher mass 2.4 and 2.8 GeV. The phase space also bring some differences.

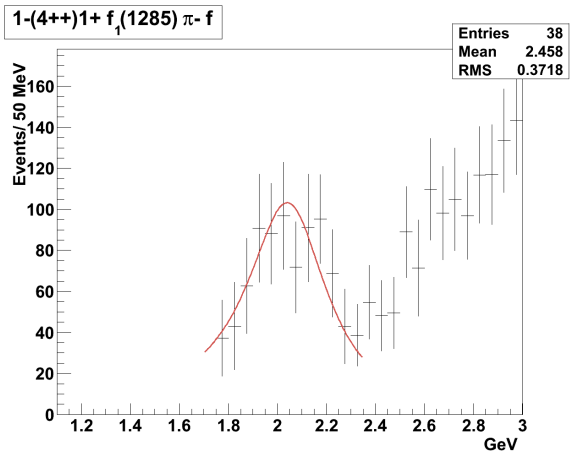

Figure 7.18: The intensity fit of 4^{++} F wave as a function of m_X. Inside the mass range of [1.8, 2.4] GeV, the peak of mass is very cleary which is around 2.0 GeV. From the PDG, we know this agrees with the a_4 which has the mass 2.04 GeV and width 400 MeV.

7.8 Extraction of results from the PWA

From the pictures shown in section 7.6 and 7.7, some results can be extracted. First of all from the distribution of intensity and phase motion in the $\pi^- f_1$ decay, we observed several particles which will be discussed in section 7.8.1. Then we can determine the branching ratios of $\pi^- f_1$ decay which will be present in section 7.8.2.

7.8.1 The mass and width of resonances

waves	Mass(GeV)	Width(MeV)	Possible resonances
$1^{-+}S$	1.76	300	$\pi_1(1600)$
$1^{++}P$	1.70,1.90	250,350	$a_1(1640), a_1(1930)$
$2^{++}P$	1.77	250	$a_2(1700)$
$1^{-+}D$	2.01	330	$\pi_1(2015)$
$2^{-+}D$	1.70,1.88,2.10	250,320,430	$\pi_2(1670), \pi_2(1880), \pi_2(2005)$
$4^{++}F$	2.04	400	$a_4(2040)$

Table 7.10: The mass and width of of possible observed resonances.

As for $1^-1^{++}0^+\pi^- f_1$ P and $1^-2^{++}1^+\pi^- f_1$ P waves, these are well-known measons $a_1(1640)$ and $a_2(1700)$. The $1^-1^{-+}1^+\pi^- f_1$ S should be $\pi_1(1600)$ and $1^-1^{-+}1^+\pi^- f_1$ D waves may be $\pi_1(2015)$. We get the $2^{-+}0^+\pi^- f_1 D$ wave corresponds to $\pi_2(1880)$ and $1^-4^{++}1^+\pi^- f_1 F$ wave corresponds to $a_4(2040)$.

As for the $2^{++}1^+P$ wave, from the intensity and phase motion, we are not sure that we have observed it. The $1^{-+}1^+$ S wave has a clear peak around the mass 1.76 GeV/c^2 and from the phase motion which always have the 180 degree shift, which means we observed the exotic resonance $\pi_1(1600)$. As for the $1^{++}0^+$ P wave, from the intensity, the sharp peak prove this resonance have the mass around the 1.7 GeV, we know this resonance should be $a_1(1640)$ from PDG. Some more resonances as $a_1(1930)$, $\pi_2(2005)$ and $a_4(2040)$ are still need more analysis.

7.8.2 Estimate of relative decay branching ratio

The exotic meson $\pi_1(1600)$ has been in the focus of COMPASS for many years. In the first PWA published by COMPASS the observation of $\pi_1(1600)$ through

its decay into $\rho\pi$ has been reported. Here we want to provide quantitative information on other decays of $\pi_1(1600)$, namely into πf_1, relative to the decay into $\rho\pi$, i.e. on relative branching ratios. We shall use unknown but assumed equal production and well-known branching ratios of $a_2(1320)$ as reference.

First of all we give a didactic introductory remark. Consider the observation of a resonance X in a given final state ab by diffractive pion excitation on nucleons: $\pi N \to XN$ with $X \to$ ab. The observed number of events is given by the product as:

$$N(X \to ab) = \sigma(X) \cdot L \cdot BR(X \to ab) \cdot acc(X \to ab) \tag{7.49}$$

where $\sigma(X)$ is the cross section for the production, L is the integrated luminosity and $BR(X \to ab)$ is the branching ratio for the decay of X into ab and acc$(X \to ab)$ is the spectrometer acceptance for the detection of resonance X in the final state ab. Since in general L is not measured in COMPASS and we want to determine the product $\sigma(X)$ BR$(X \to ab)$ from the PWA we use $\sigma(X)$ BR$(X \to ab)$ of a known resonance (here X is a_2), with known branching ratios BR$(X \to ab)$ as reference. Branching ratios of $a_2(1320)$ taken from PDG:

BR$(a_2(1320) \to 3\pi\ ) = 70$ % (3π contains $\rho(770)\pi$, $f_2\pi$ and $\rho(1450)\pi$)

With upper limit from PDG:
BR$(a_2 \to f_2\pi$ and $\rho(1450)\pi)$/ BR$(a_2 \to \rho(770)\pi) < 0.12$.

Thus we estimate the BR$(a_2 \to \rho(770)\pi) = (63 \pm 3)\%$

From PDG we also get the branching ratio: BR$(a2 \to \eta^{'}\pi) = (0.54 \pm 0.10)\%$

The branching ratio: BR$(a_2 \to \eta\pi) = (14.5 \pm 2.0)\%$ can be used as a cross check by comparing for the same data set the a_2 decaying to $\eta^{'}\pi$ and to $\eta\pi$.

Measured ratios of intensities from $\pi^-(1600) \to \rho\pi$ and $a_2 \to \rho\pi$ can be gotten from COMPASS exotic 3π publication PRL 104(2010)241803: Observation of an exotic 1^{-+} resonance in diffractive dissociation of $190 GeV/c$ $\pi^- p \to 3\pi p$, taken from tables in publication[59]. Analysis was based on 2004 data with unknown integrated luminosity. The target was not a proton target but nucleons in lead. If pomeron exchange dominates, the production cross sections for the same resonances can be assumed to be equal with the proton

target. Of course, if data from the 2008 run are available they should preferably be used.

Intensity of $1^{-+} \to \rho(770)\pi : (1.7 \pm 0.2)\%$

Intensity of $a_2(1320) \to \rho(770)\pi : (19.2 \pm 0.6)\%$

Using the BR($a_2 \to \rho(770)\pi$)= 63% we can estimate the relative intensity $a_2(1320) \to$all:$(19.2 \pm 0.6)\%/(0.63 \pm 0.3) = (30.5 \pm 1.5)\%$

Hence we obtain for the ratio R_1 of the products of production strength times decay BRs from the published data $\pi^- p \to \pi^-\pi^+\pi^- p$ of COMPASS

$$R_1 = (production(1^{-+})BR(1^{-+} \to \rho\pi))/(production(a_2)BR(a_2 \to all)) \tag{7.50}$$

$$= (1.7 \pm 0.2)\%/(30.5 \pm 1.5)\% = 0.06 \pm 0.01 \tag{7.51}$$

Here production stands either for the cross section $\sigma(X)$ or the product of cross section times integrated luminosity L. Of course, for PWA results from the same data sample, L is assumed to be equal for different resonances.

For the ratio obtained in the new $\eta^{'}\pi$ analysis from new 2009 data of COMPASS[60]:

$$R_2 = (production(1^{-+})BR(1^{-+} \to \eta^{'}\pi))/(production(a_2)BR(a_2 \to all)) \tag{7.52}$$

$$\approx 0.021 \pm 0.006 \tag{7.53}$$

The production cross sections are equal in the new and old data. Thus the first estimate of the ratios of decay branching ratios for the exotic 1^{-+} yields, based on the normalisation with $a_2(1320)$, using R_1/R_2 with an error of 20%.

$$BR(1^{-+} \to \eta^{'}\pi)/BR(1^{-+} \to \rho(770)\pi) = 0.02/0.06 = 1/3 \tag{7.54}$$

In the case of ab=$\pi^- f_1$ PWA results, there are no obvious known resonances in this final state. So we has to use the fact that this data sample has the same integrated luminosity as the final state ab = $\pi\eta^{'}$ and normalize as well to X= $a_2 \to \pi\eta^{'}$.

As for the BR($1^{-+} \to f_1\pi$) / BR ($1^{-+} \to \eta^{'}\pi$):

$$\frac{BR(1^{-+} \to \pi^- f_1)}{BR(1^{-+} \to \pi^- \eta^{'})} = \frac{N(1^{-+} \to \pi^- f_1) acc(X \to \pi^- \eta^{'})}{N(1^{-+} \to \pi^- \eta^{'}) acc(X \to \pi^- f_1)} \tag{7.55}$$

if the numbers of events N are extracted from the same data sample i.e. have the same integrated luminosity L.

A realistic comparison of acceptances is needed, by a realistic MC. Here we take the acceptance of mass and correct with an acceptance ratio $acc(M_{\pi^- f_1})/acc(M_{\pi^- \eta^{'}})$.

In order to estimate of the ratios of decay branching ratios for the exotic 1^{-+} yields, we present the intensity of 1^{-+} in in $\pi^- \eta^{'}$ channel. From the intensity plots of $1^{-+} \to \pi^- f_1$ and $1^{-+} \to \pi^- \eta^{'}$, we can know the events of these two decays.

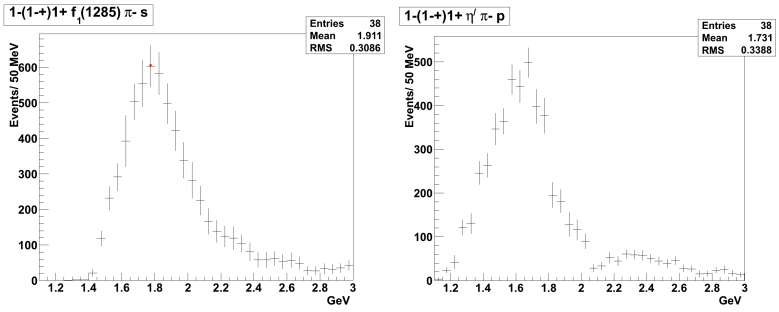

Figure 7.19: The left one is the intensity of 1^{-+} in $\pi^- f_1$ channel and The right one is the intensity of 1^{-+} in $\pi^- \eta^{'}$ channel. The peak is very clearly and mostly have the same mass peak as 1^{-+} wave in $\pi^- f_1$ channel, acceptance corrected with the fast MC.

After integrated the differential intensities of $\pi^- \eta^{'}$ and $\pi^- f_1$ in the figure 7.22, the events number of $\pi^- \eta^{'}$ is ≈ 5000 and $\pi^- f_1$ is ≈ 6000.

According the MC acceptance in section 6.3, we can learn that the acceptance of fast MC and full MC for $\pi^- f_1$ channel is about 43% and 8.9%[60]. The acceptance of fast MC and full MC for $\pi^- \eta^{'}$ channel is about 72% and 15%[10]. So the ratio of full MC acceptance between $\pi^- f_1$ and $\pi^- \eta^{'}$ is about:

$$\frac{8.9\%}{15.0\%} \approx 0.59 \pm 0.02 \tag{7.56}$$

and the ratio of fast MC acceptance between $\pi^- f_1$ and $\pi^- \eta^{'}$ is about:

$$\frac{43.0\%}{72.0\%} \approx 0.60 \pm 0.02 \tag{7.57}$$

Where the errors have been conservatively estimated, thus the acceptance ratios agree well. This is due to the decay of the final states are both $\pi^-\pi^+\eta$.

With the acceptances ratio of Full MC $\approx$ the acceptances ratio of Fast MC, we can estimate the BR of these two decays.

$$\frac{N(1^{-+} \to \pi^- f_1) acc(X \to \pi^- \eta^{'})}{N(1^{-+} \to \pi^- \eta^{'}) acc(X \to \pi^- f_1)} \approx \frac{6000}{5000 * 0.6} = 2 \pm 0.5 \tag{7.58}$$

Additionally, the BR between $1^{-+} \to \pi^- f_1$ and $1^{-+} \to \pi^- \rho(770)$ is:

$$\frac{N(1^{-+} \to \pi^- \rho(770)) acc(X \to \pi^- f_1)}{N(1^{-+} \to \pi^- f_1) acc(X \to \pi^- \rho(770))} \approx 3/2 = 1.5 \pm 0.3 \tag{7.59}$$

In summary we have obtained

$$BR(1^{-+} \to \rho\pi) : BR(1^{-+} \to \eta^{'}\pi) : BR(1^{-+} \to f_1\pi) = 3 : 1 : 2 \tag{7.60}$$

Chapter 8

Conclusion

Sometimes it is not so easy to understand the experiment. We should use some tools to analyse the data from the experiment. For example the PHAST,the root. The experiment provides the key for physics analysis and the more we understand it the more we can learn from it. Therefore, this thesis analyses a final state of $\pi^- p$ interactions and describes partial wave analysis of the channel $\pi^- p \to (\pi^- f_1)p$.

The thesis presents the results of the analysis on final states with neutral mesons (η , f_1). The reactions $\pi^- p \to Xp$, $X \to \pi^- f_1$, $f_1 \to \pi^-\pi^+\eta$, $\eta \to \pi^-\pi^+\pi^0$, $\pi^0 \to \gamma\gamma$ and $\eta \to \gamma\gamma$ with an incoming π^- beam of 190 GeV/c were studied. The analysis was performed on a part of 2008 data. The event selection was explained in detail with the goal to select favoured events and minimize background events by applying cuts.

In the scope of this thesis, a partial wave analysis (PWA) of $\pi^-\pi^-\pi^+\eta$ final state events from diffractive pion dissociation at COMPASS has been carried out. In the regime of high momentum transfer ($0.1 < t^{'} < 1.0 GeV^2/c^2$) more than $4.5{*}10^6$ events have been studied, employing a set of 35 partial waves in a mass-independent PWA. The particular final state $\pi^- f_1$ is a subset of the various 2-body intermediate state leading to $\pi^-\pi^-\pi^+\eta$. This subset has been described by 7 partial waves. A subsequent mass-dependent fit has been performed for 3 waves. The particles $a_1(1640)$, $\pi_1(1600)$ and $\pi_2(1670)/(1880)$ are resolved with good quality, confirming the Particle Data Group (PDG) average values for mass and width. In addition, the $a_1(1930)$, $\pi_2(2005)$, $a_4(2040)$ mesons are included in the data. An emphasis of the analysis certainly is the spin-exotic $1^{-+}1^+(\pi^- f_1)$ wave obtained with the mass-dependent fit. Due to its exotic quantum numbers, this state cannot be a conventional $q\bar{q}$ meson

and is a hot candidate for a $q\bar{q}g$ hybrid. Several theory models predict a 1^{-+} hybrid in the light-quark sector with a mass between 1.5 and 2.0 GeV/c^2[63]. The relative branching ratios have been estimated for the decays of the exotic meson $\pi_1(1600)$. A first attempt has been made to extract the branching ratio $1^{-+} \to \pi^- f_1$ relative to that of $1^{-+} \to \pi^- \eta'$, BR($1^{-+} \to \pi^- f_1$)/BR($1^{-+} \to \pi^- \eta'$) $\approx 2 \pm 0.5$. This is lower than the value 3.8± 0.8 in the 2010 PDG[27]. Moreover, the branching ratio of $1^{-+} \to \pi^- \rho(770)$ relative to that of $1^{-+} \to \pi^- f_1$ has been estimated, BR($1^{-+} \to \pi^- \rho(770)$)/BR($1^{-+} \to \pi^- f_1$) $\approx 1.5 \pm$ 0.3. Thus it has been found that BR($1^{-+} \to \pi^- \rho(770)$): BR($1^{-+} \to \pi^- \eta'$): BR($1^{-+} \to \pi^- f_1$)= 3:1:2.

At the end of this work, we can make some suggestions for a further improvement in the analysis of the $\pi^- f_1$ channel at COMPASS, dictated from the experience gained. In particular, we consider the following important points:
1) The t dependent partial wave analysis of $\pi^- f_1$ final state events from diffractive pion dissociation should be carried out.
2) With increased statistics the analysis can be extended to higher masses and higher orbit angular momentum L and projection M.
3) More attention should be paid to extract the partial wave analysis with the unnatural ϵ= -1.
4) A detailed mass dependent analysis has still to be performed.
5) The fast Monte Carlo similation should be replaced by a more realistic full Monte Carlo simulation.
6) A systematic study of the contribution of more waves, at least up to 9 waves (L=3) should be performed.

Appendix A

Mass distributions

We show mass distributions with all kinds of selections where $\eta \to \pi^-\pi^+\pi^0$. The X=$\pi^- f_1 \to \pi^-\pi^+\eta$ channel has $\binom{1}{3}\binom{1}{2} = 6$ kinds of combinations.

A.1 Mass distribution of $\pi^-\pi^+$

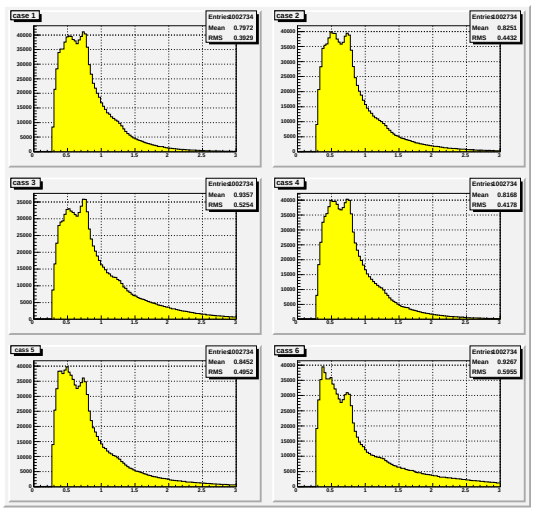

Figure A.1: The 6 cases of $\pi^-\pi^+$ mass distribution after π^0 selection without η and $_1$ selection. We can see the $\pi^-\pi^+$ can be $\rho(770)$ which is especially obvious in the case 3. From the case 6 we can see the peak around 300MeV. We know the mass of π^- and π^+ is 139.57MeV. The sum is 280MeV.

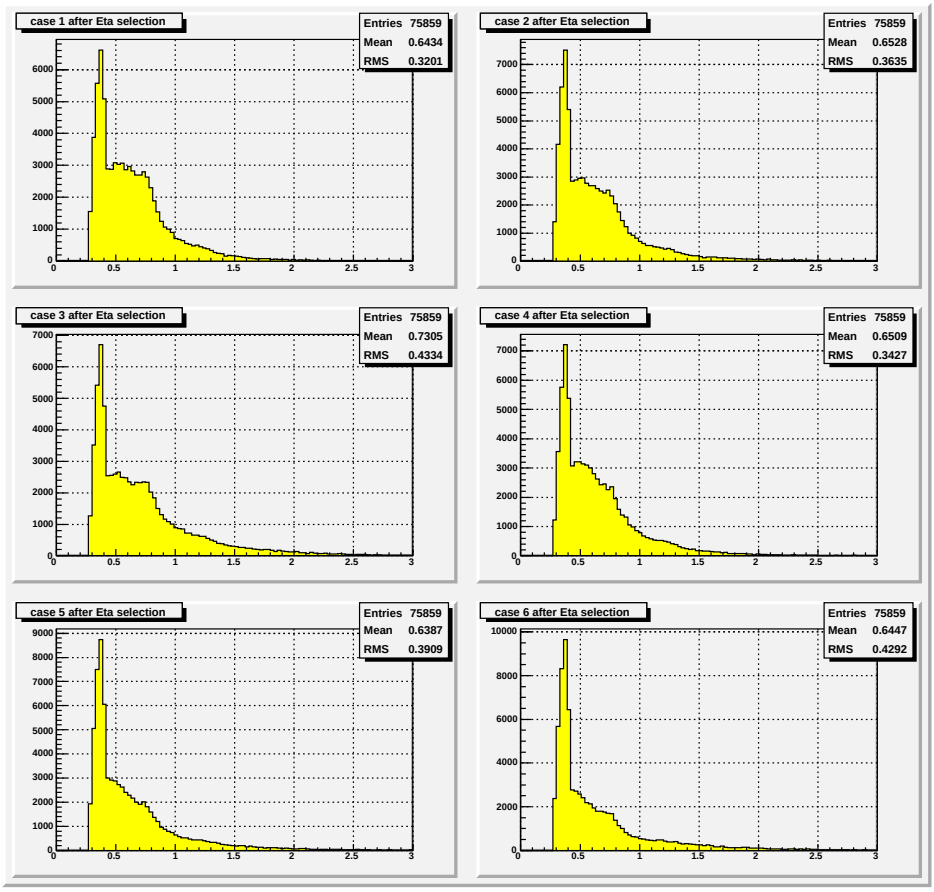

Figure A.2: The 6 cases of $\pi^-\pi^+$ mass distribution after η We can see that $\pi^-\pi^+$ after η selection, the peak of $\rho(770)$ mostly disappear. This is easy to understand, just because we select the η is decay to $\pi^-\pi^+\pi^0$, The mass of $\pi^-\pi^+$ should be smaller than (770) Which is especially clear in the figure 6.1. Though the compare, we also can see the background is different. Some of the difference is caused by the combinatorial background. In this way we can understand the difference between case 1 and case 6.

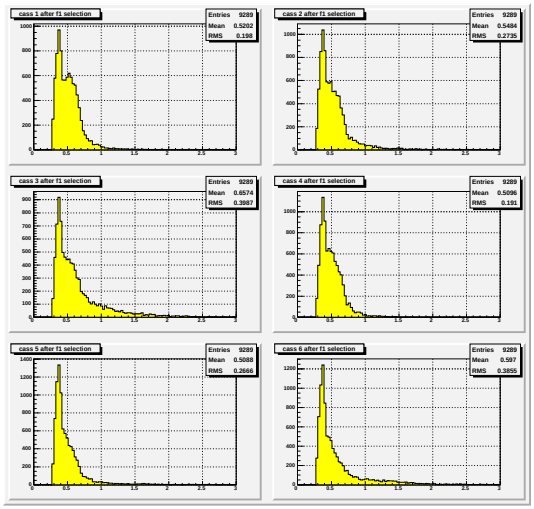

Figure A.3: The 6 cases of $\pi^-\pi^+$ mass distribution after f_1 cut.

A.2 Mass distribution of $\pi^-\pi^+\pi^0$

Next figures show the mass distribution of $\pi^-\pi^+\pi^0$.

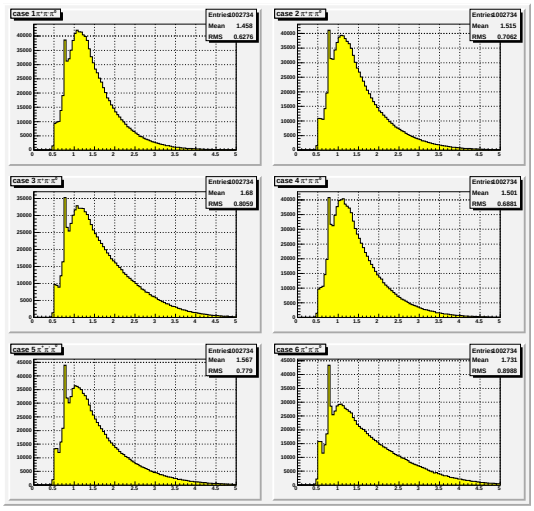

Figure A.4: Cases of $\pi^-\pi^+\pi^0$ mass distribution after π^0 cut

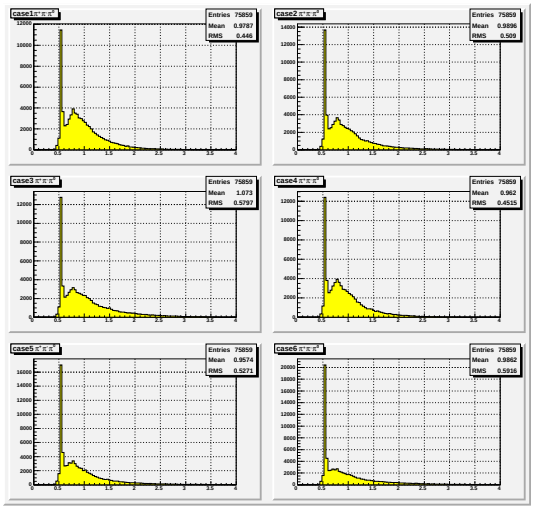

Figure A.5: The 6 cases of $\pi^-\pi^+\pi^0$ mass distribution after η cut

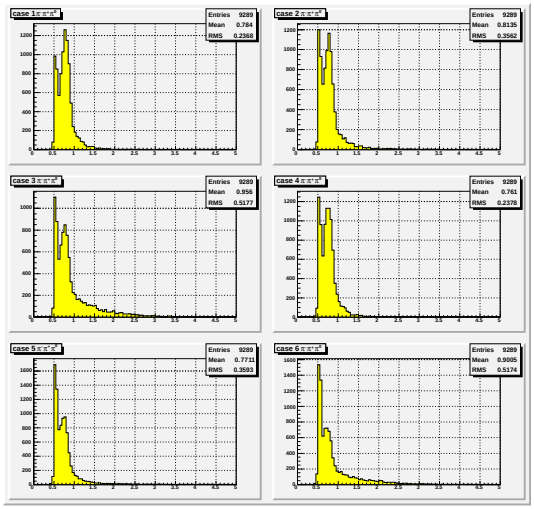

Figure A.6: The 6 cases of $\pi^-\pi^+\pi^0$ mass distribution after f_1 cut

A.3 Mass distribution of $\pi^-\pi^+\pi^-\pi^+\pi^0$

Because the $\pi^-\pi^+\pi^-\pi^+\pi^0$ include two π^+, the combinations should be calculate as C_3^1. That is not the same as just one π^- and one π^+ distribution which have six cases. Here we show three cases mass distribution of $\pi^-\pi^+\pi^-\pi^+\pi^0$.

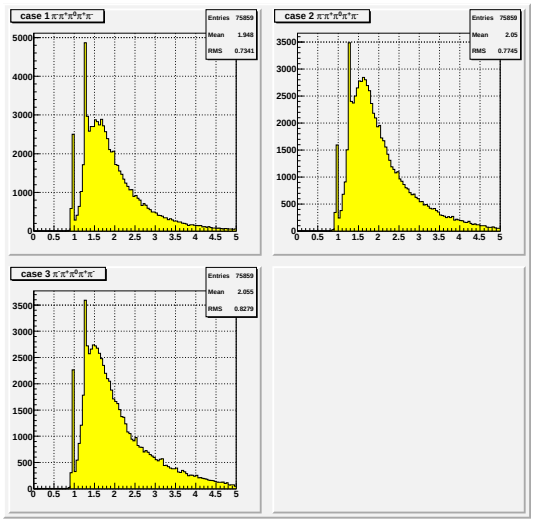

Figure A.7: The 3 cases of $\pi^-\pi^+\pi^0\pi^-\pi^+$ mass distribution after η cut. Here we have two π^+, so we just have 3 cases of $\pi^-\pi^+\pi^-\pi^+\pi^0$.

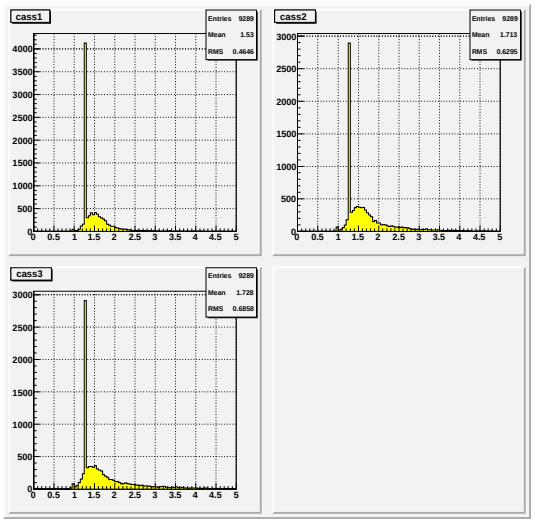

Figure A.8: The 3 cases of $\pi^-\pi^+\pi^0\pi^-\pi^+$ mass distribution after f_1 cut

Appendix B

t distributions

Here we compare two kinds of t distributions $A\exp(-bt')$ and $At'\exp(-bt')$ in every 500 MeV mass bin(from[64]).

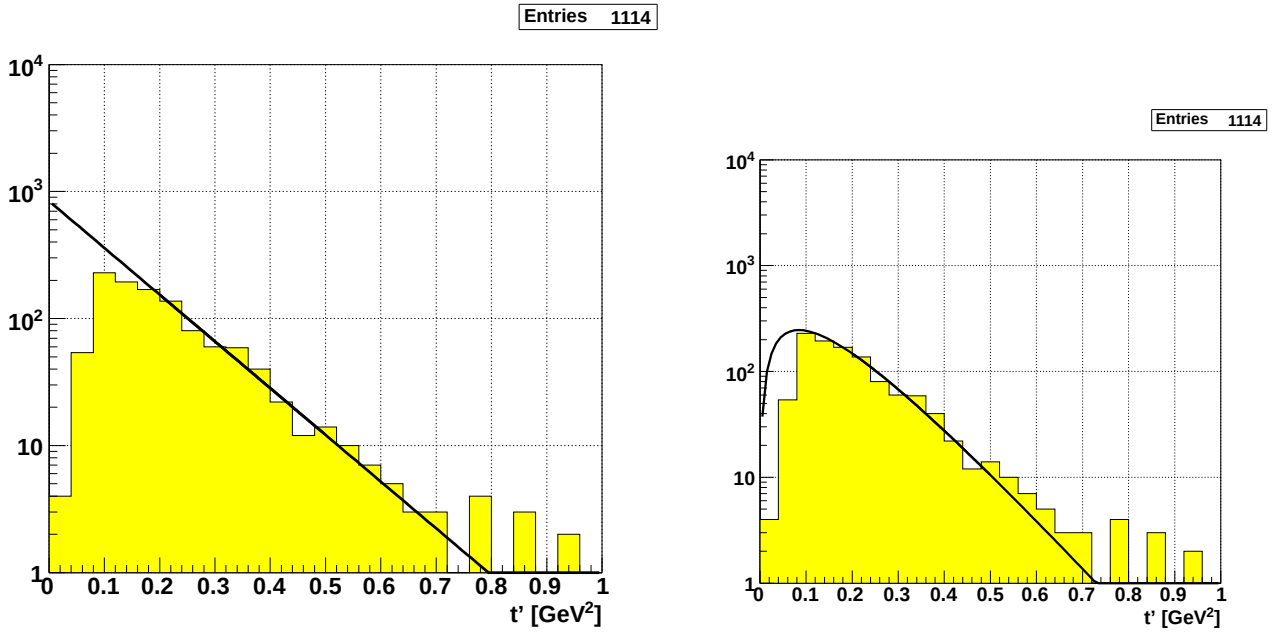

Figure B.1: The fit $A\exp(-bt')$ vs $At'\exp(-bt')$: $1.00 < m(\pi^- f_1) < 1.50$

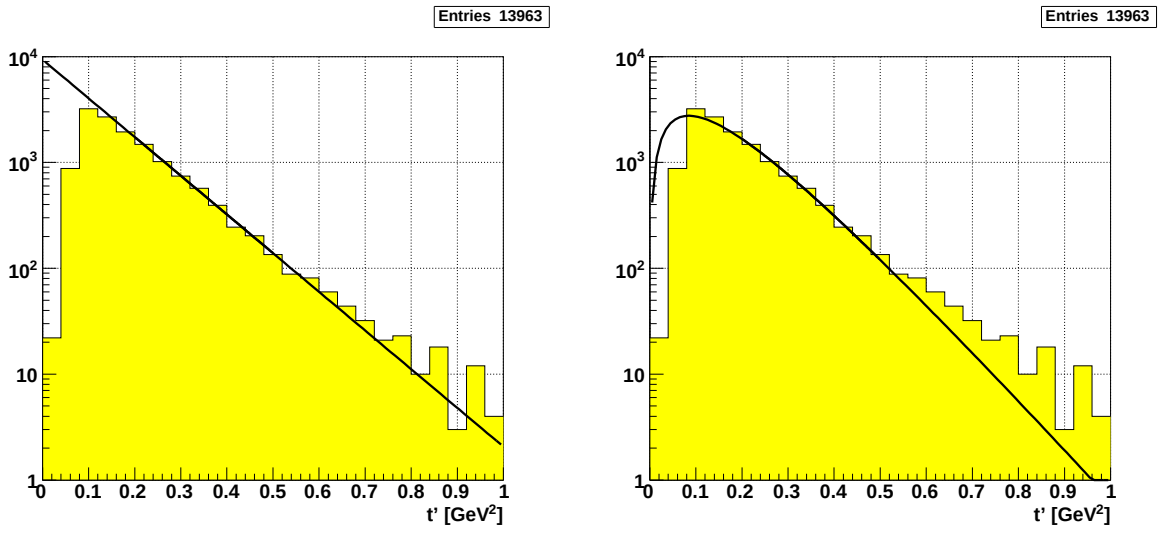

Figure B.2: The fit $A\exp(-bt')$ vs $At'\exp(-bt')$: $1.25 < m(\pi^- f_1) < 1.75$

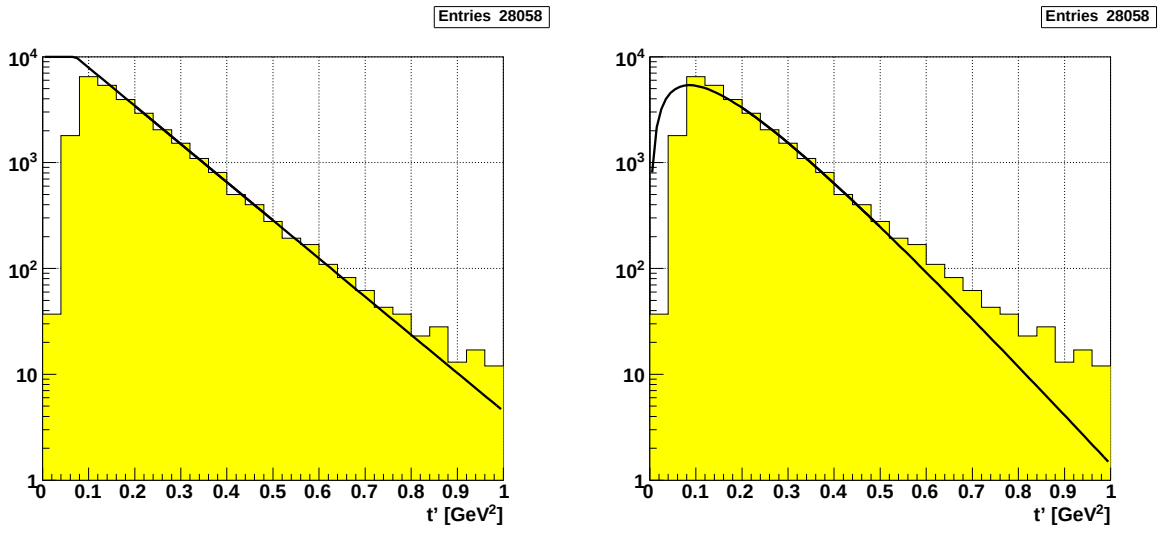

Figure B.3: The fit $A\exp(-bt')$ vs $At'\exp(-bt')$: $1.50 < m(\pi^- f_1) < 2.00$

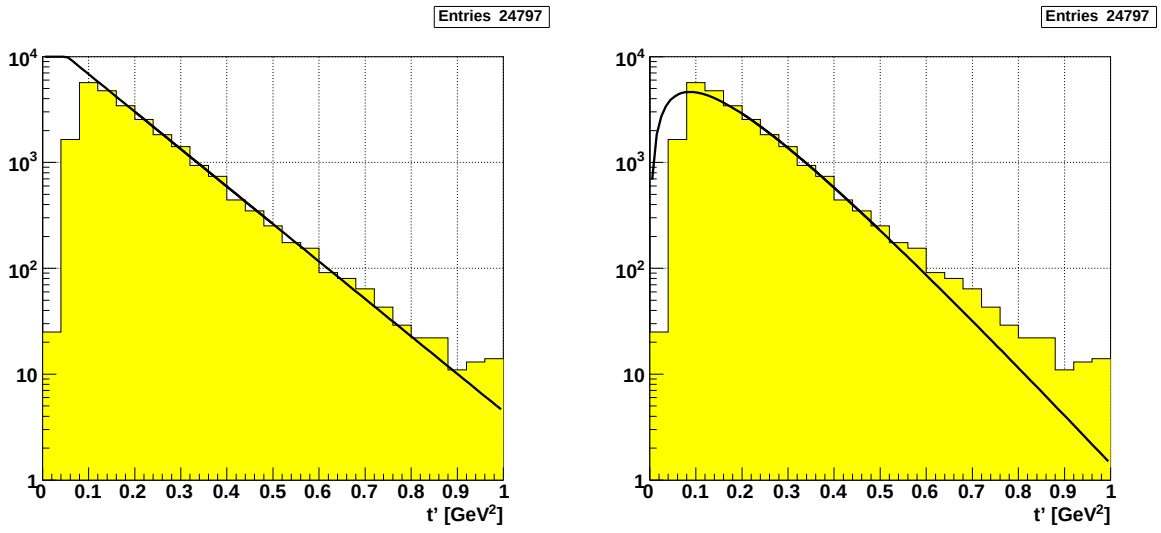

Figure B.4: The fit $A\exp(-bt')$ vs $At'\exp(-bt')$: $1.75 < m(\pi^- f_1) < 2.25$

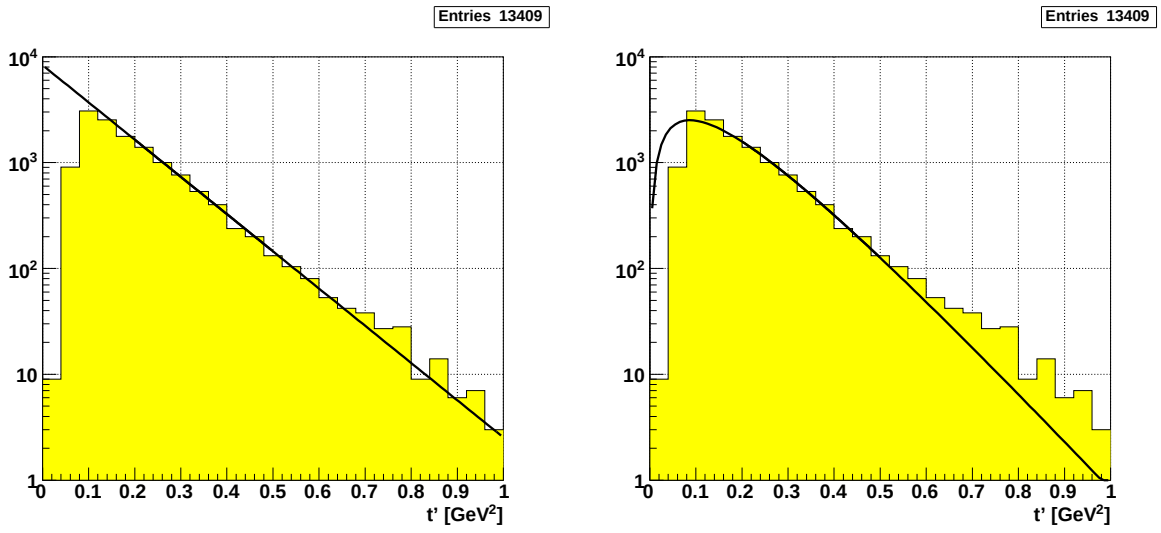

Figure B.5: The fit $A\exp(-bt')$ vs $At'\exp(-bt')$: $2.00 < m(\pi^- f_1) < 2.50$

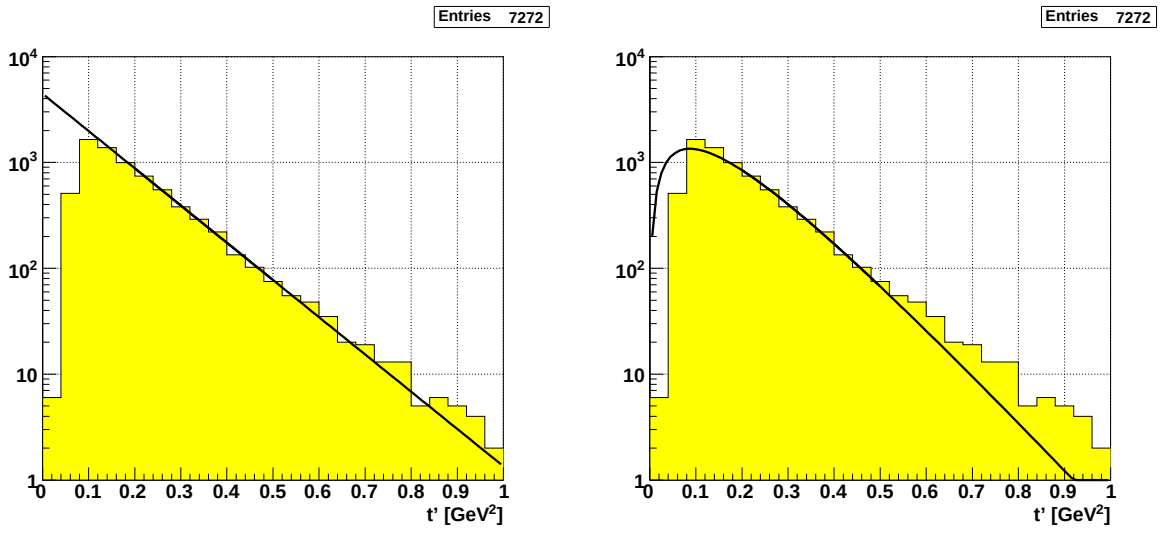

Figure B.6: The fit $A\exp(-bt')$ vs $At'\exp(-bt')$: $2.25 < m(\pi^- f_1) < 2.75$

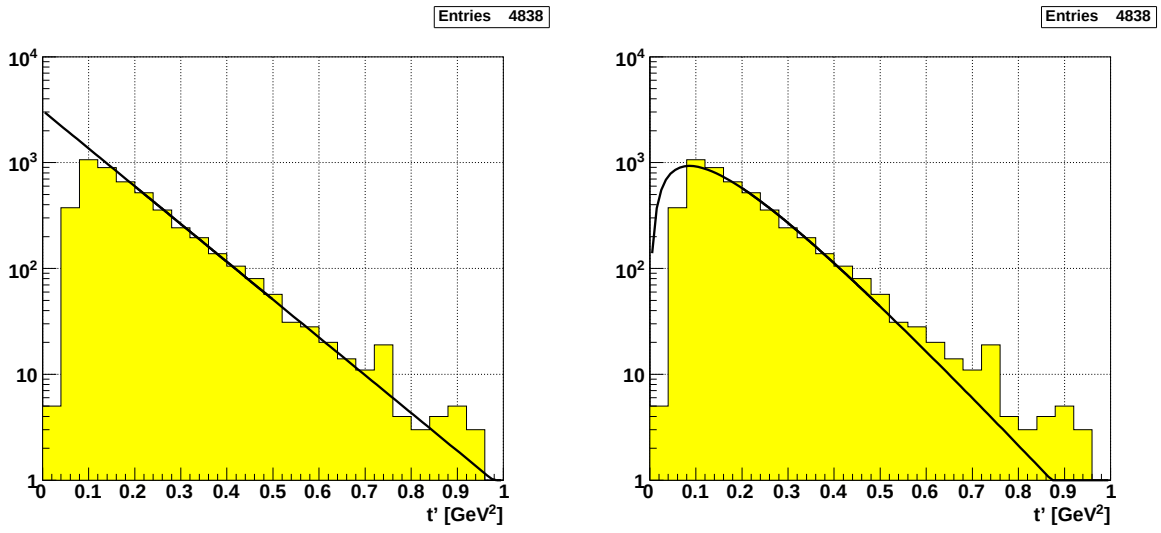

Figure B.7: The fit $A\exp(-bt')$ vs $At'\exp(-bt')$: $2.50 < m(\pi^- f_1) < 3.00$

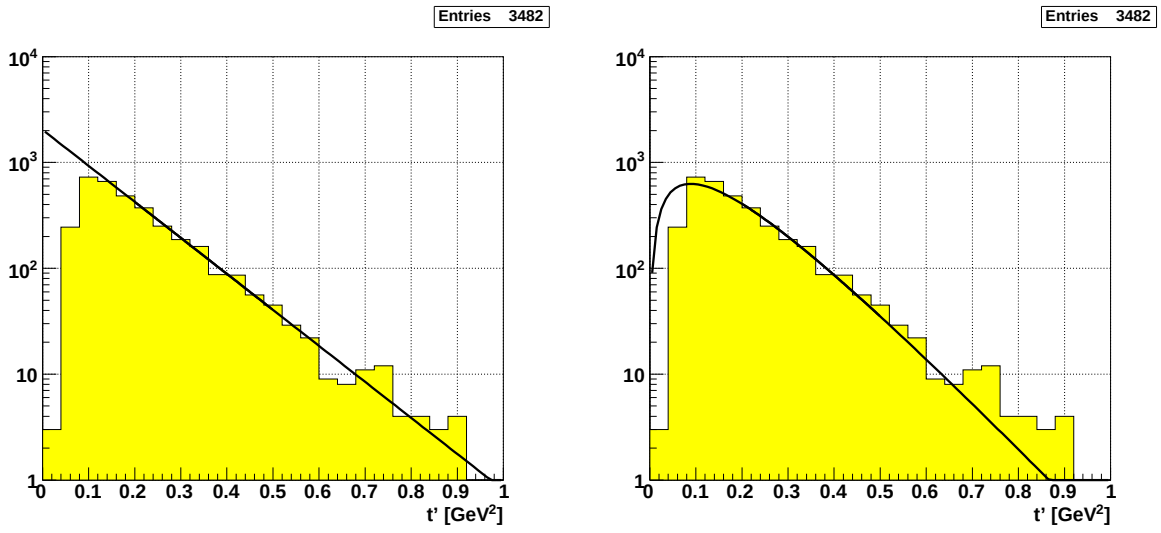

Figure B.8: The fit $A\exp(-bt')$ vs $At'\exp(-bt')$: $2.75 < m(\pi^- f_1) < 3.25$

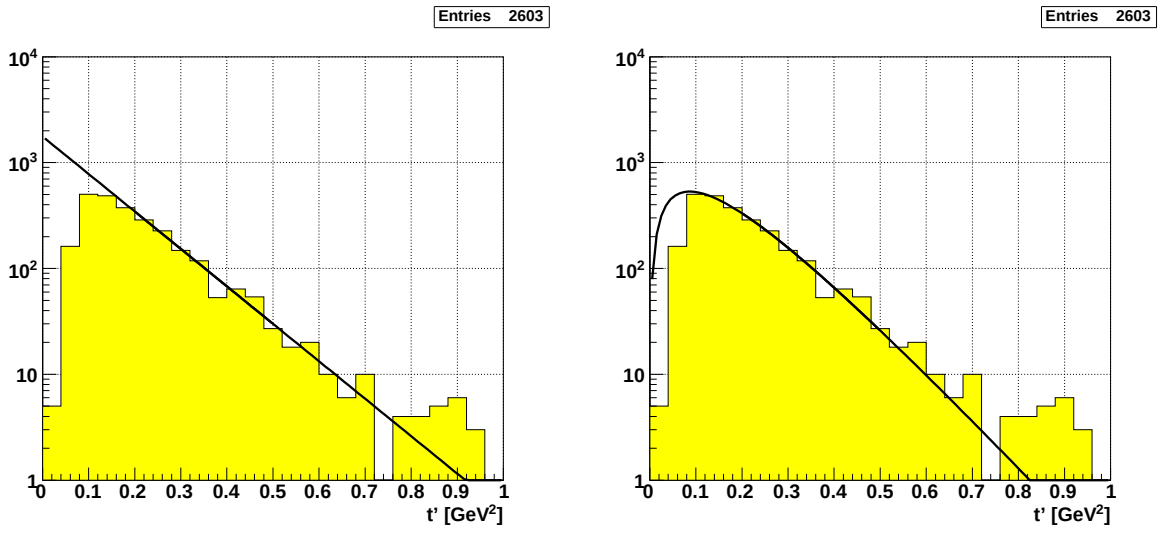

Figure B.9: The fit $A\exp(-bt')$ vs $At'\exp(-bt')$: $3.00 < m(\pi^- f_1) < 3.50$

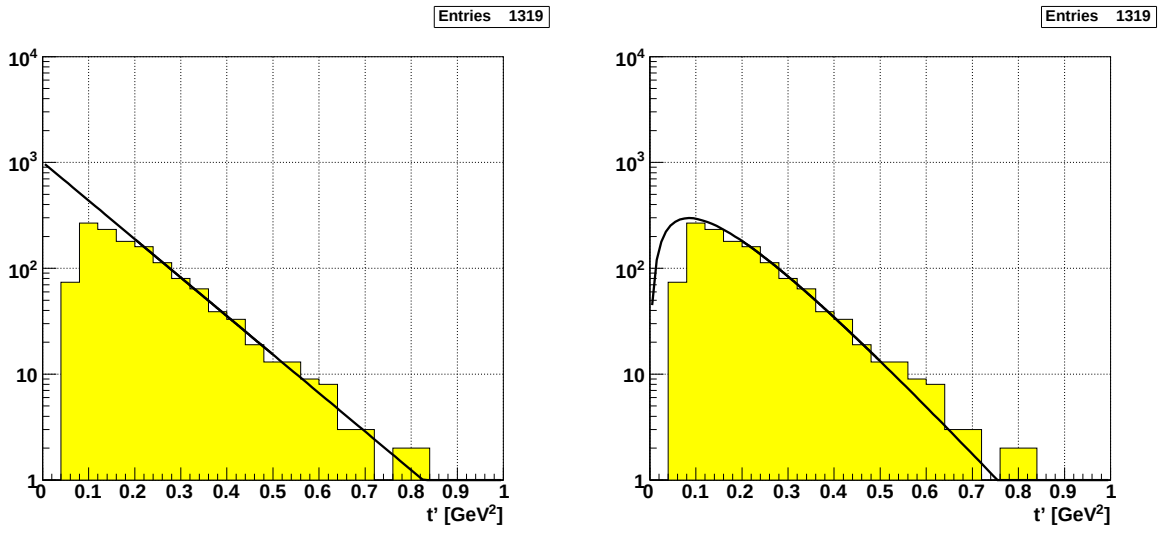

Figure B.10: The fit $A\exp(-bt')$ vs $At'\exp(-bt')$: $3.75 < m(\pi^- f_1) < 4.25$

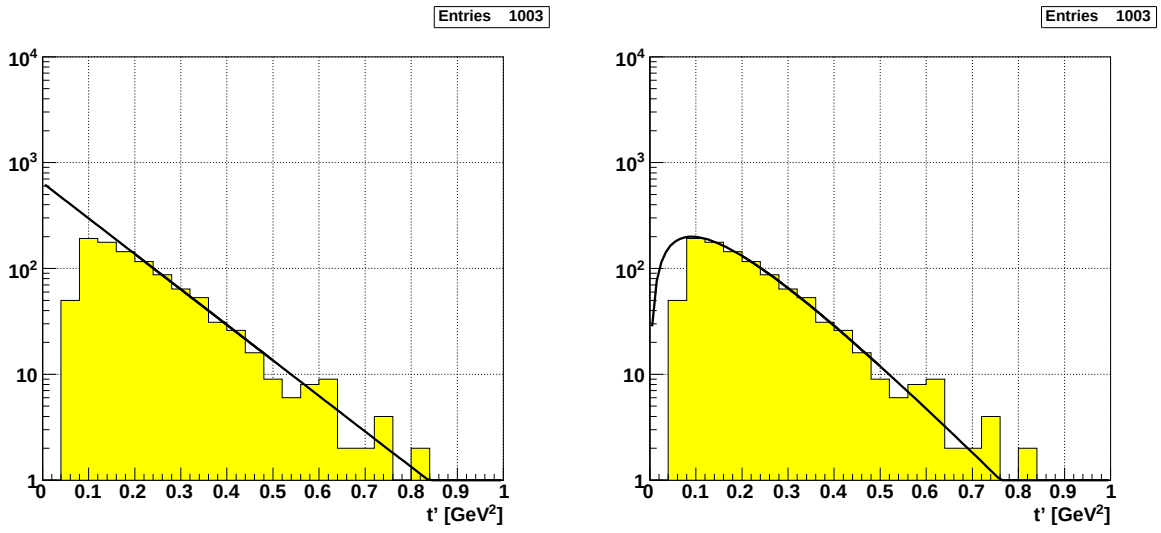

Figure B.11: The fit $A\exp(-bt')$ vs $At'\exp(-bt')$: $4.00 < m(\pi^- f_1) < 4.50$

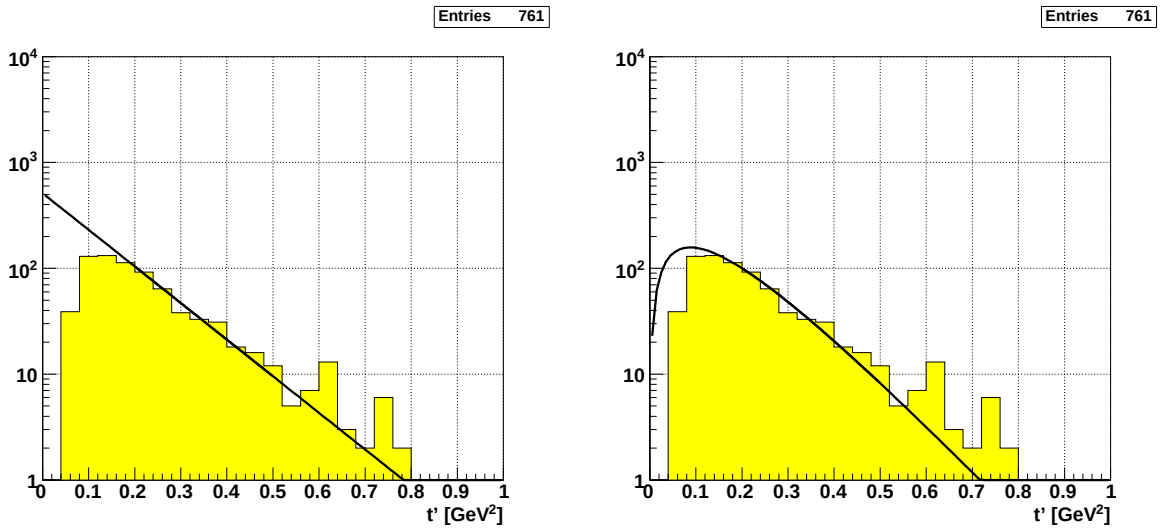

Figure B.12: The fit $A\exp(-bt')$ vs $At'\exp(-bt')$: $4.25 < m(\pi^- f_1) < 4.75$

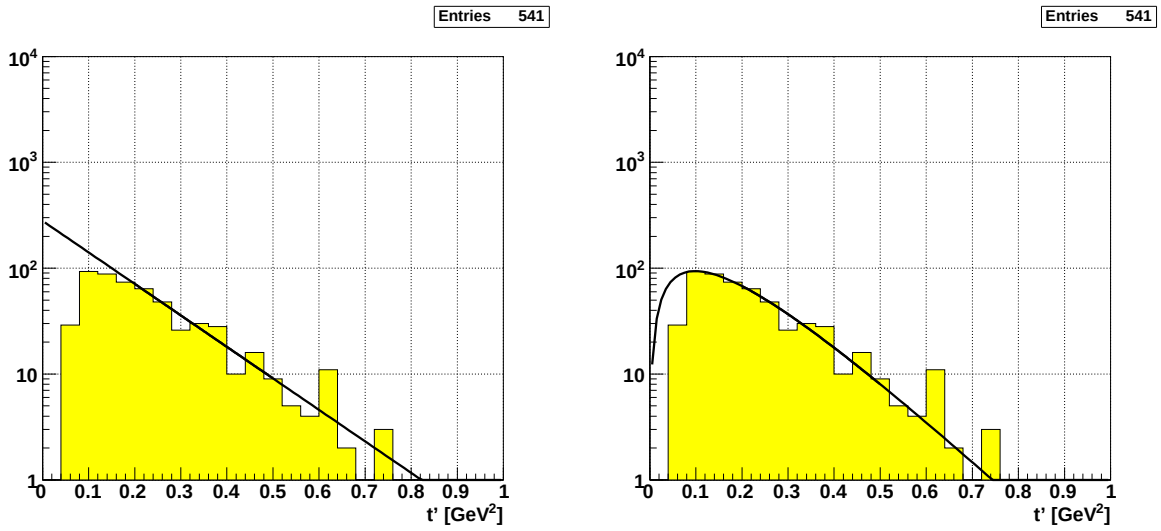

Figure B.13: The fit $A\exp(-bt')$ vs $At'\exp(-bt')$: $4.50 < m(\pi^- f_1) < 5.00$

Appendix C

Angular distributions

C.1 The angular distribution in Gottfried-Jackson frame

Here we present $\cos\theta_G$ distribution with the mass range from 1.7 to 3.0 GeV after divided the mass into intervals of 200 MeV where the $\eta \to \pi^-\pi^+\pi^0$.

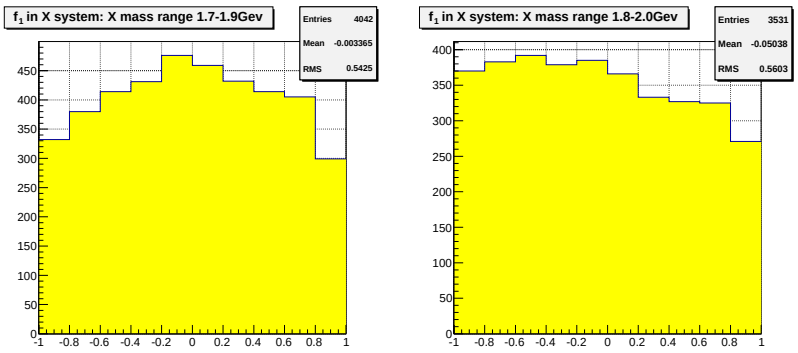

Figure C.1: $\cos\theta_G$ in X rest system:1.7-2.0 GeV. Here $\eta \to \pi^-\pi^+\pi^0$.

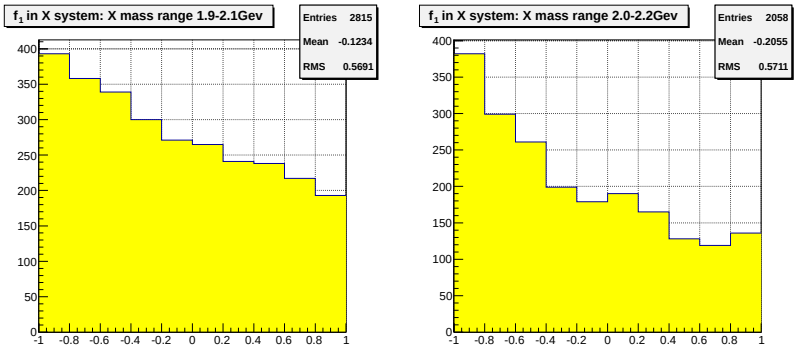

Figure C.2: $\cos\theta_G$ in X rest system:1.9-2.2 GeV. Here $\eta \to \pi^-\pi^+\pi^0$.

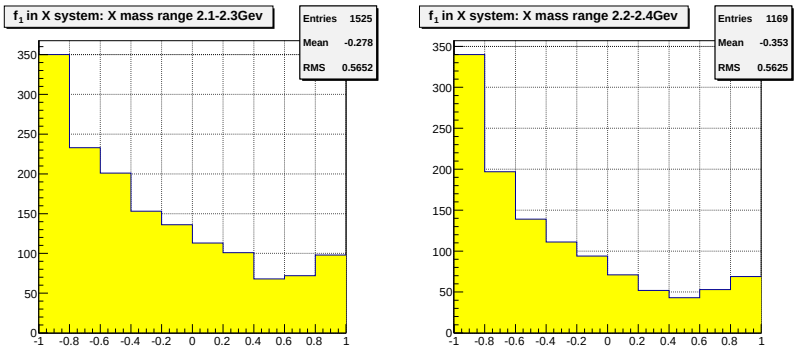

Figure C.3: $\cos\theta_G$ in X rest system:2.1-2.4 GeV. Here $\eta \to \pi^-\pi^+\pi^0$.

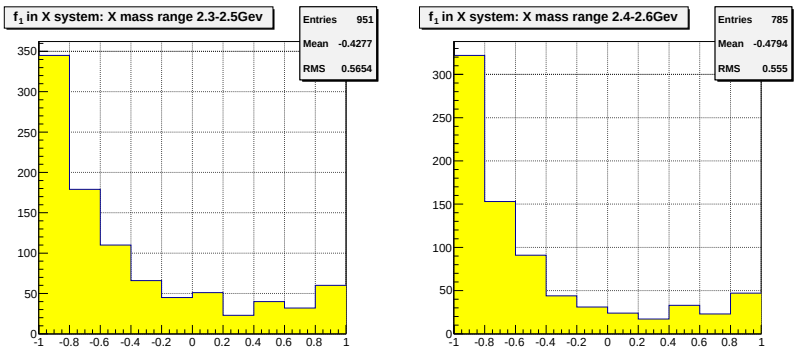

Figure C.4: $\cos\theta_G$ in X rest system:2.3-2.6 GeV. Here $\eta \to \pi^-\pi^+\pi^0$.

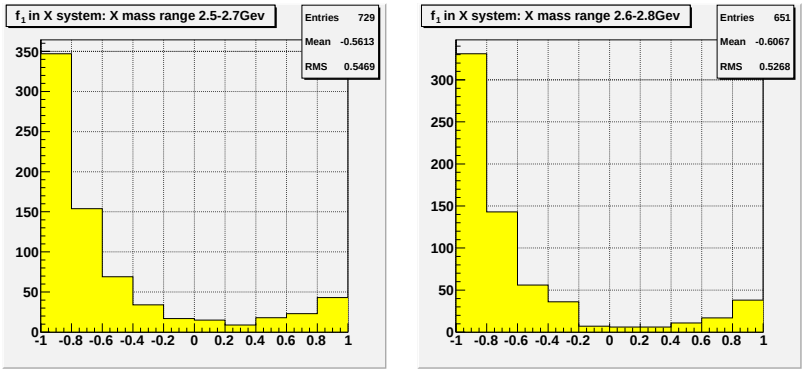

Figure C.5: $\cos\theta_G$ in X rest system:2.5-2.8 GeV. Here $\eta \to \pi^-\pi^+\pi^0$.

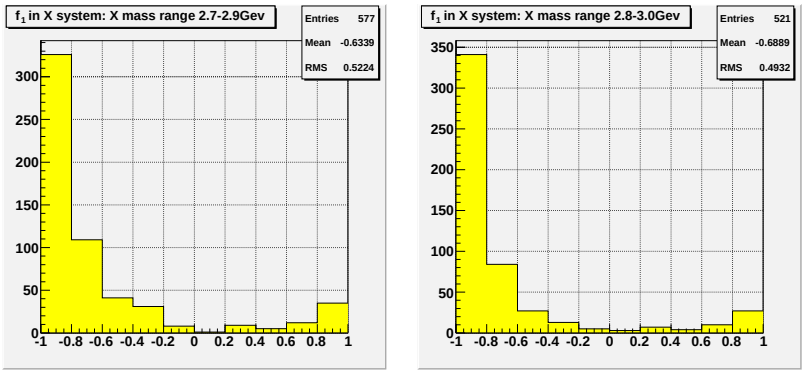

Figure C.6: $\cos\theta_G$ in X rest system:2.7-3.0 GeV. Here $\eta \to \pi^-\pi^+\pi^0$.

C.2 The background of f_1 in angular distribution

Here we present $\cos\theta$ distribution in left side bin, right side bin and central bin where $\eta \to \pi^-\pi^+\pi^0$.

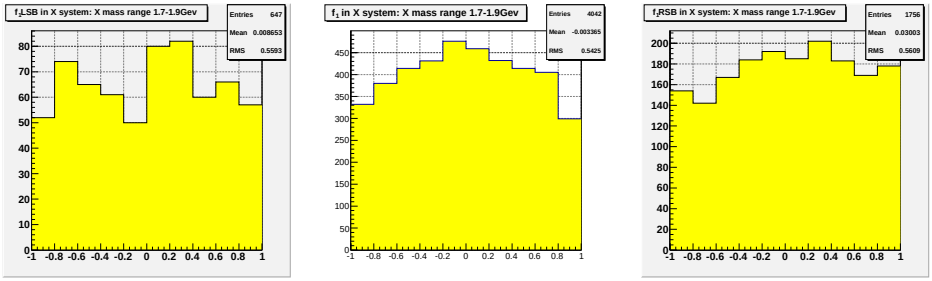

Figure C.7: $\cos\theta_G$ in X rest system:1.7-1.9. The left one is the left side-bin; the middle one is the central bin; the right one is the right side-bin.

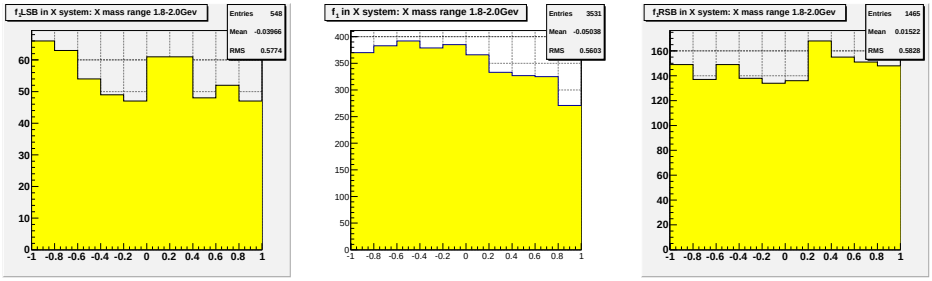

Figure C.8: Like figure C.7, mass:1.8-2.0.

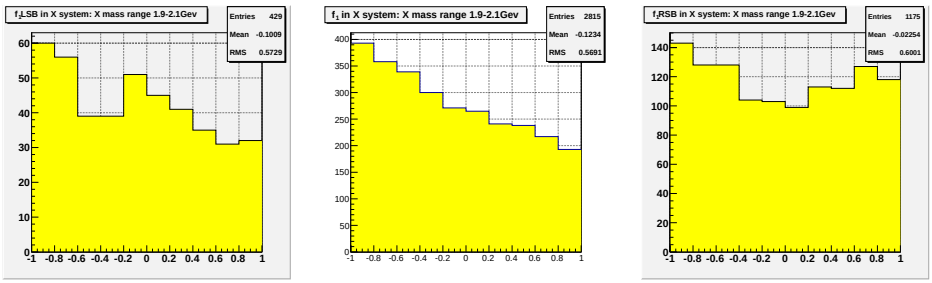

Figure C.9: Like figure C.7, mass:1.9-2.1.

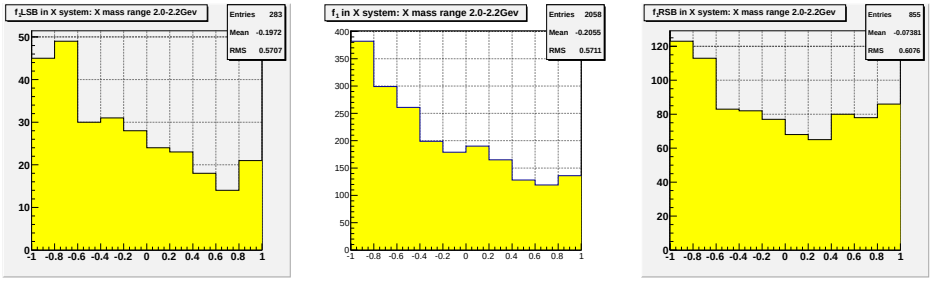

Figure C.10: Like figure C.7, mass:2.0-2.2.

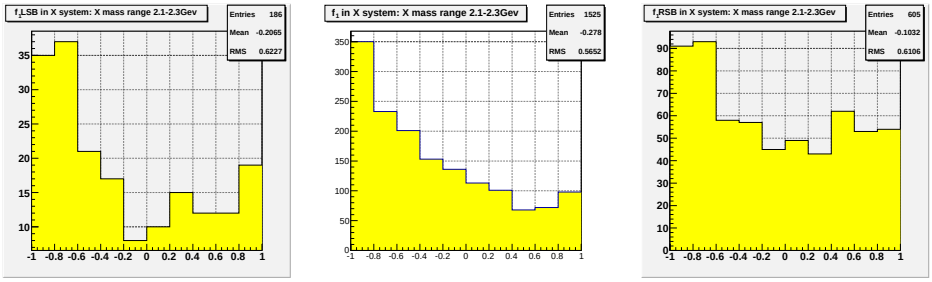

Figure C.11: Like figure C.7, mass:2.1-2.3.

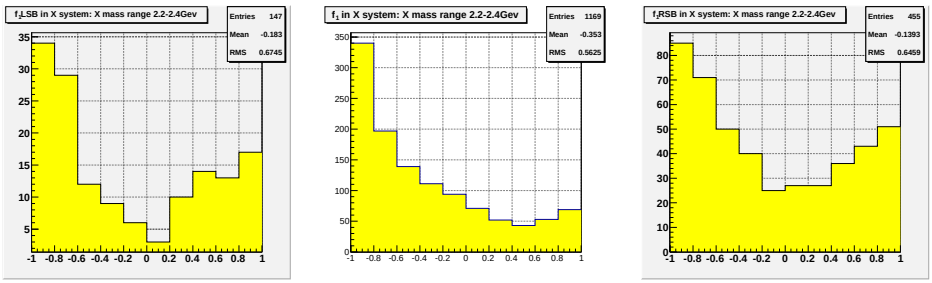

Figure C.12: Like figure C.7, mass:2.2-2.4.

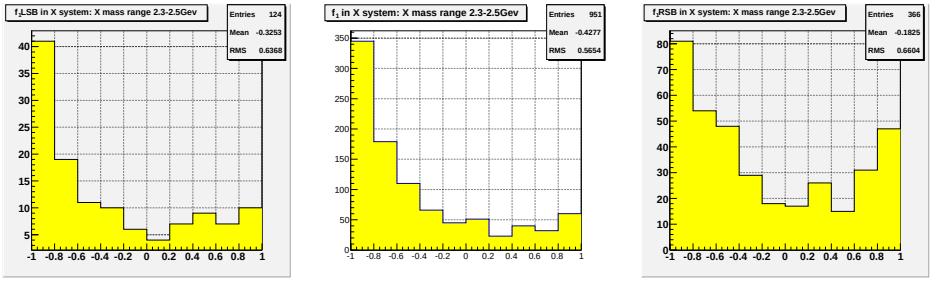

Figure C.13: Like figure C.7, mass:2.3-2.5.

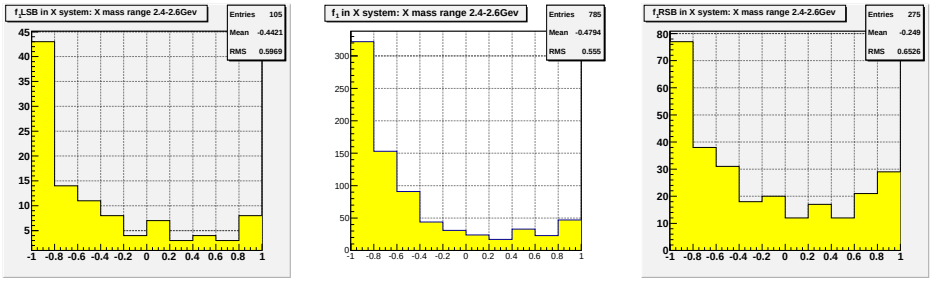

Figure C.14: Like figure C.7, mass:2.4-2.6.

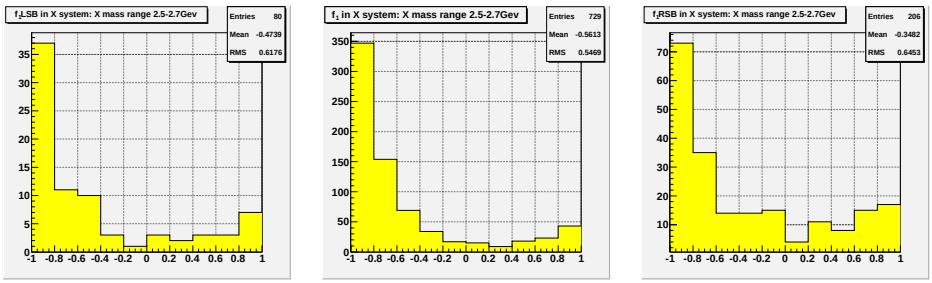

Figure C.15: Like figure C.7, mass:2.5-2.7.

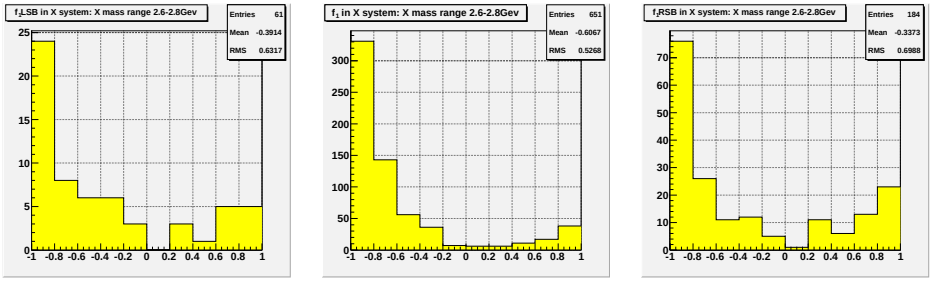

Figure C.16: Like figure C.7, mass:2.6-2.8.

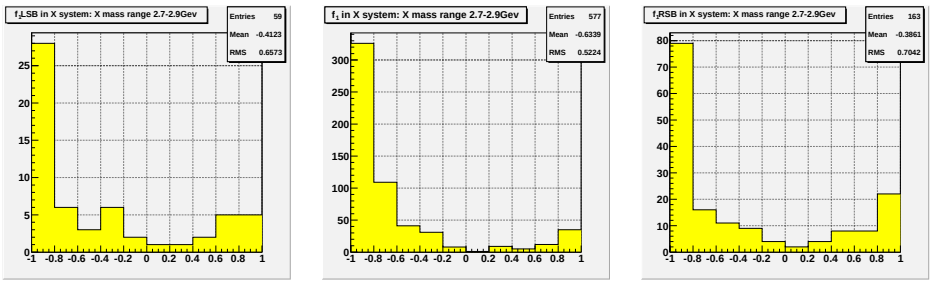

Figure C.17: Like figure C.7, mass:2.7-2.9.

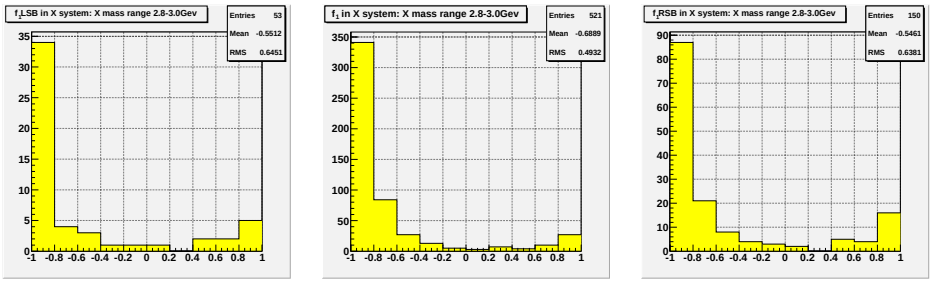

Figure C.18: Like figure C.7, mass:2.8-3.0.

Appendix D

The phase motion plots

The following figures show the combined terms in the total intensity and phase motion between $1^-1^{-+}1^+$ S wave, $1^-1^{++}0^+$ P wave, $1^-2^{++}1^+$ P wave, $1^-1^{-+}1^+$ D wave, $1^-2^{-+}0^+$ D wave, $1^-3^{++}0^+$ F wave and $1^-4^{++}1^+$ F wave[58].

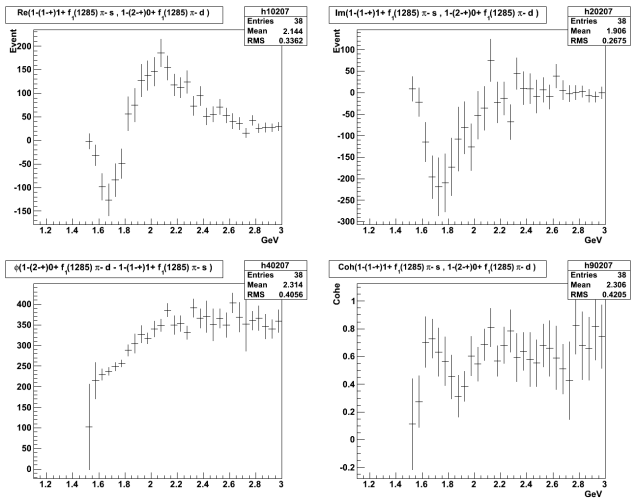

Figure D.1: The combined terms and phase motion between $1^-1^{-+}1^+$ S wave and $1^-2^{-+}0^+$ D wave. The left-top is the real part of $a^*(2^{-+}0^+)a(1^{++}0^+)$ and the right-top is the imaginary part of $a^*(1^{-+}1^+)a(2^{-+}0^+)$. The vertical axis is in units of events in the chosen mass bin of 50 MeV/c^2. The left-bottom is the phase motion in the units of degrees from -90° to +90° and the right-bottom is the coherence as defined in formula 7.38. All quantities are plotted as a function of m_x.

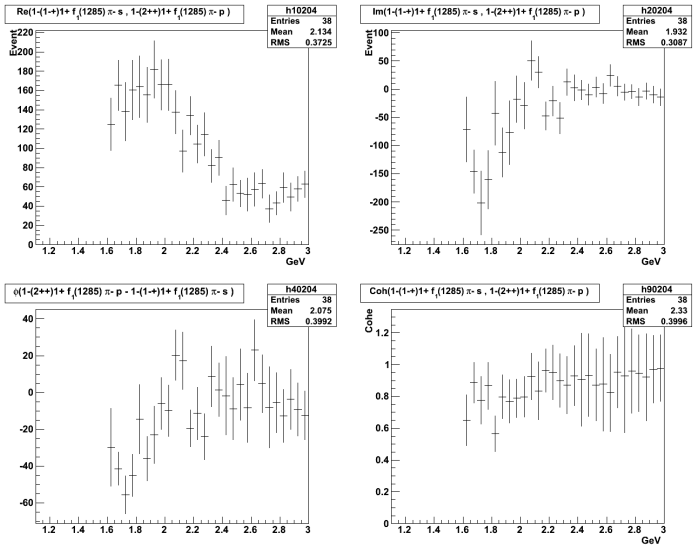

Figure D.2: Like figure D.1 for the $1^-1^{-+}1^+$S wave and $1^-2^{++}1^+$P wave.

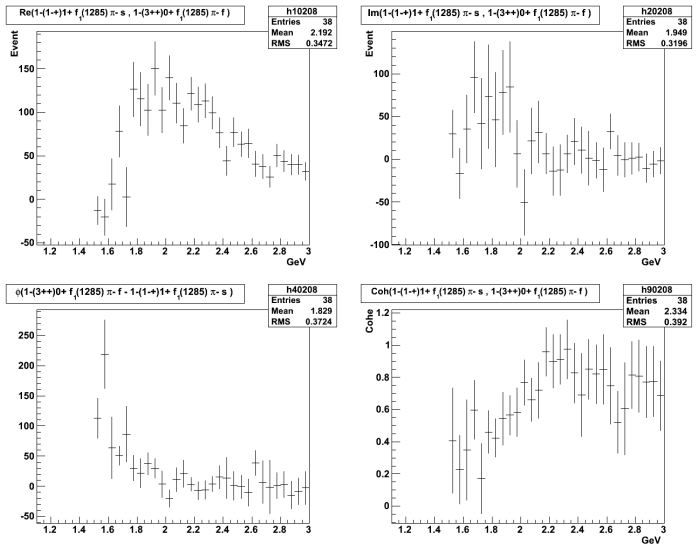

Figure D.3: Like figure D.1 for the $1^-1^{-+}1^+$S wave and $1^-3^{++}0^+$F wave.

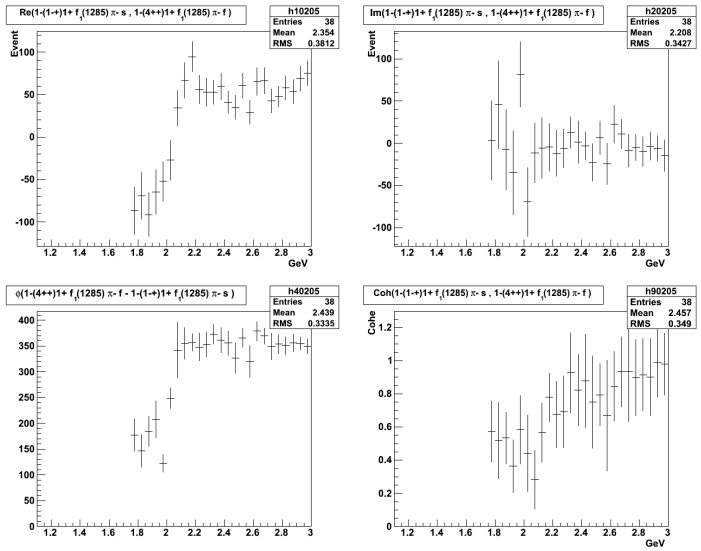

Figure D.4: Like figure D.1 for the $1^-1^{-+}1^+$S wave and $1^-4^{++}1^+$F wave.

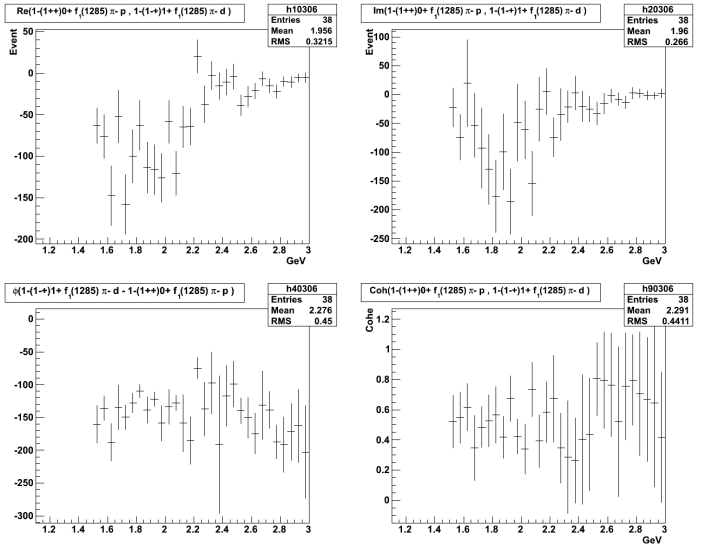

Figure D.5: Like figure D.1 for the $1^-1^{++}0^+$P wave and $1^-1^{-+}1^+$D wave.

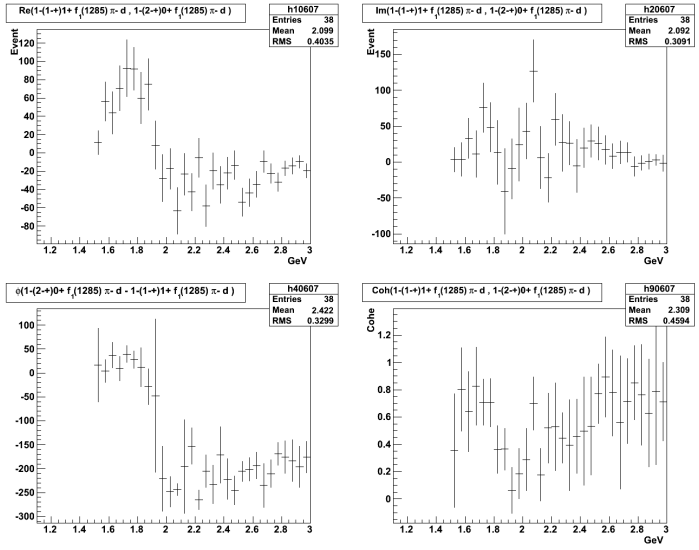

Figure D.6: Like figure D.1 for the $1^-1^{-+}1^+$D wave and $1^-2^{-+}0^+$D wave.

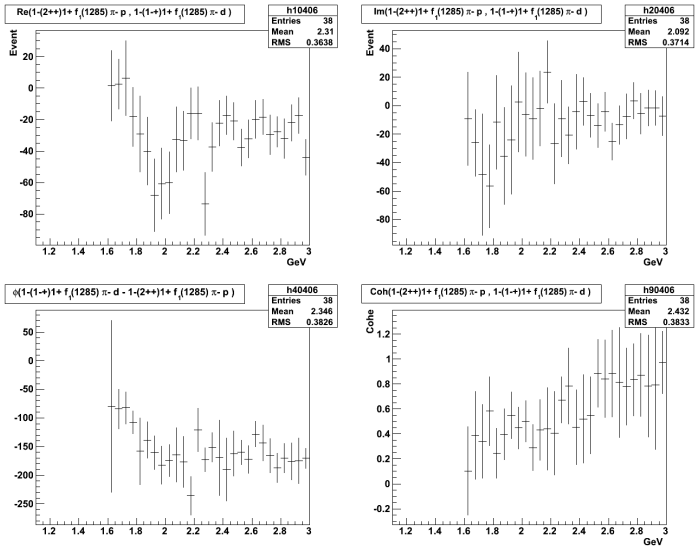

Figure D.7: Like figure D.1 for the $1^-2^{++}1^+$P wave and $1^-1^{-+}1^+$D wave.

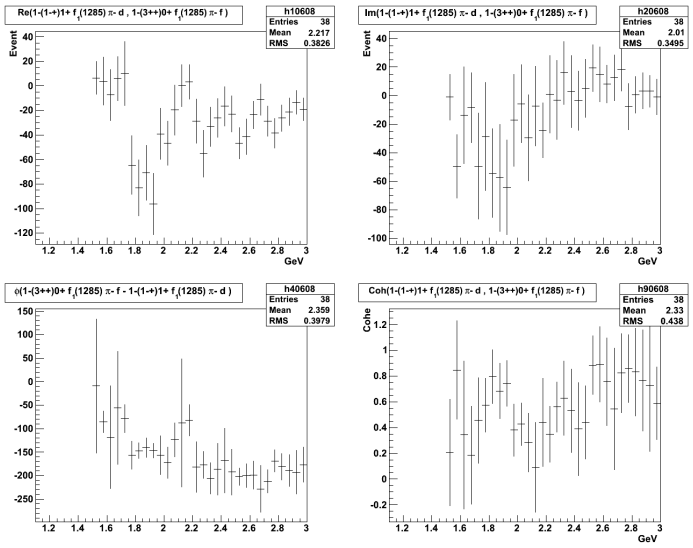

Figure D.8: Like figure D.1 for the $1^-1^{-+}1^+$D wave and $1^-3^{++}0^+$F wave.

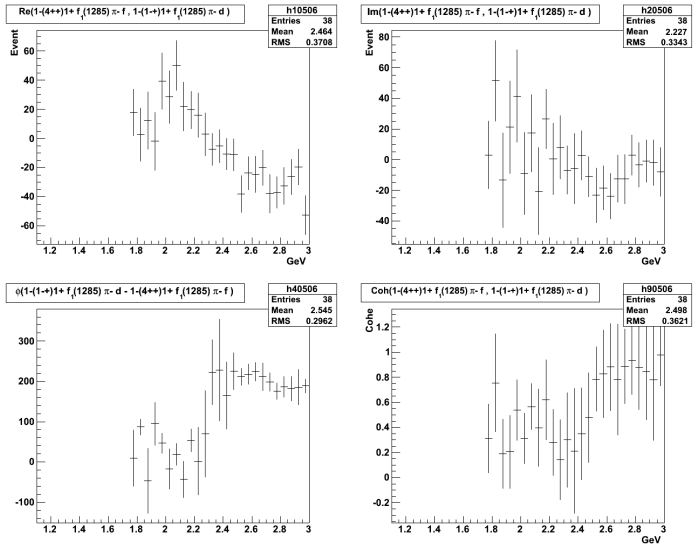

Figure D.9: Like figure D.1 for the $1^-4^{++}1^+$F wave and $1^-1^{-+}1^+$D wave.

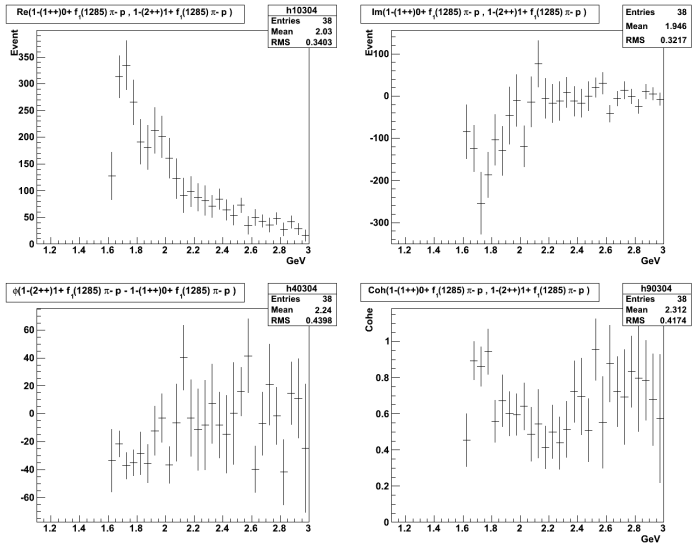

Figure D.10: Like figure D.1 for the $1^-1^{++}0^+$P wave and $1^-2^{++}1^+$P wave.

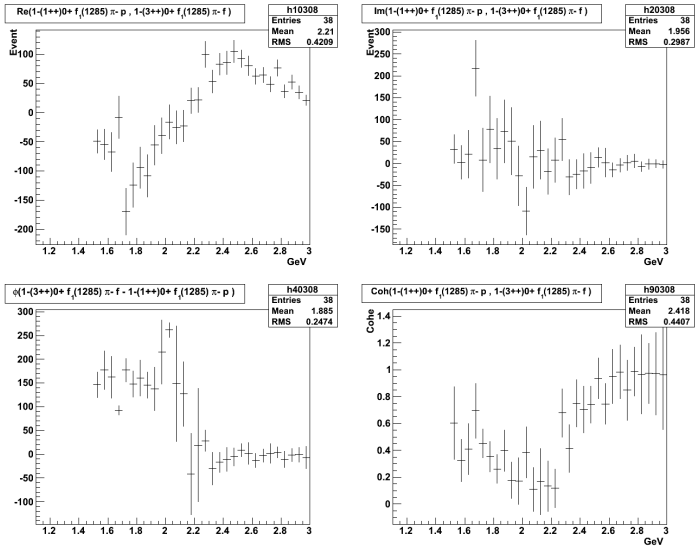

Figure D.11: Like figure D.1 for the $1^-1^{++}0^+$P wave and $1^-3^{++}0^+$F wave.

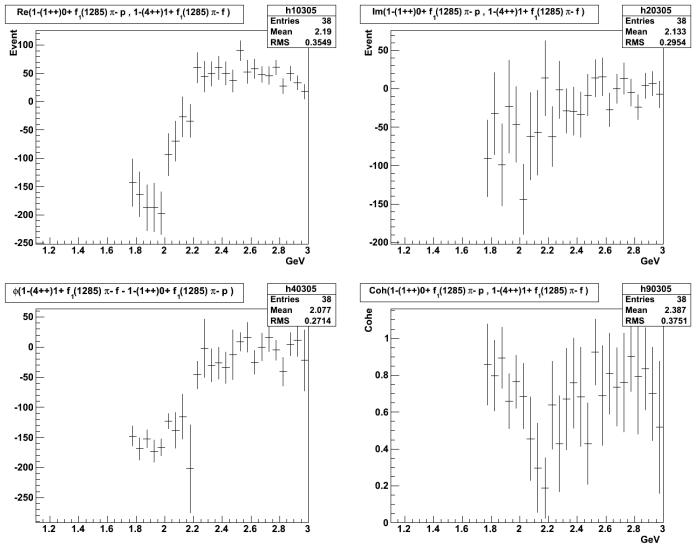

Figure D.12: Like figure D.1 for the $1^-1^{++}0^+$P wave and $1^-4^{++}1^+$F wave.

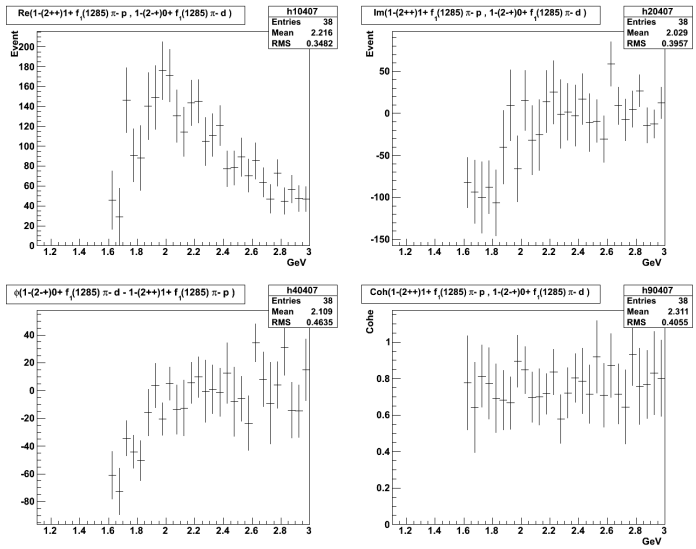

Figure D.13: Like figure D.1 for the $1^-2^{++}1^+$P wave and $1^-2^{-+}0^+$D wave.

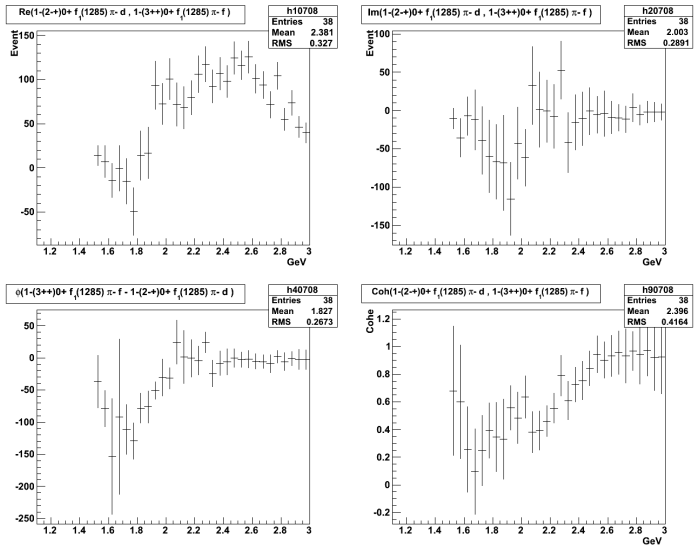

Figure D.14: Like figure D.1 for $1^-2^{-+}0^+$D wave and $1^-3^{++}0^+$F wave.

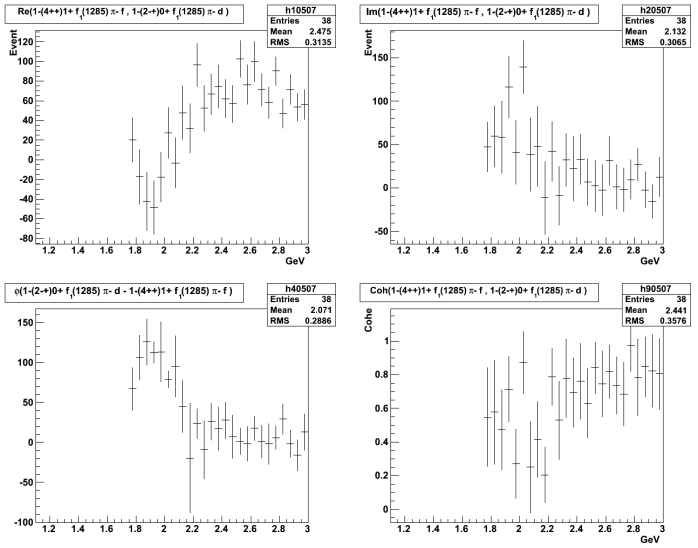

Figure D.15: Like figure D.1 for the $1^-4^{++}1^+$P wave and $1^-2^{-+}0^+$D wave.

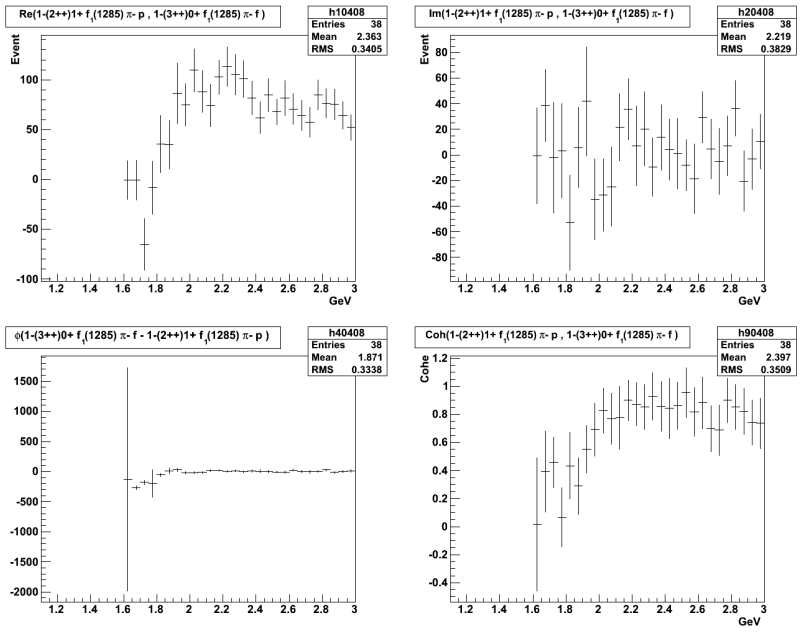

Figure D.16: Like figure D.1 for $1^-2^{++}1^+$P wave and $1^-3^{++}0^+$F wave.

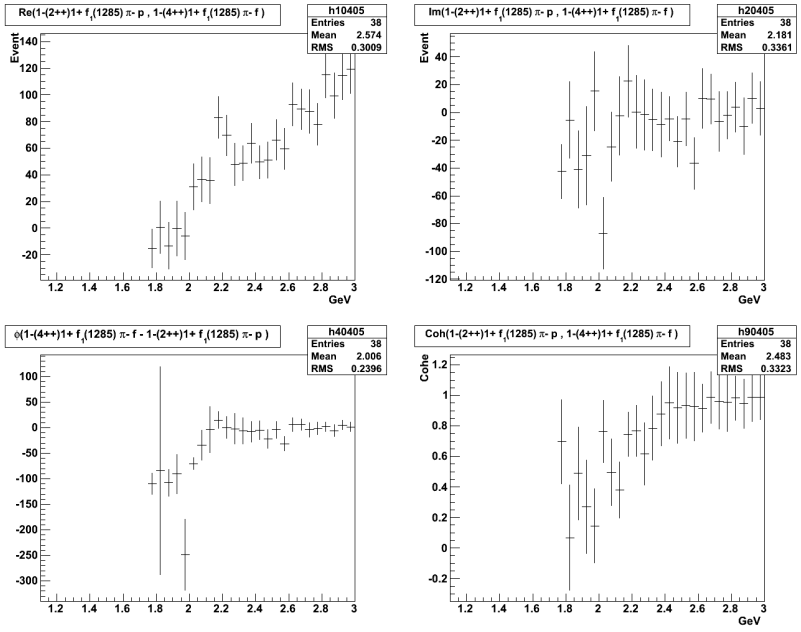

Figure D.17: Like figure D.1 for $1^-2^{++}1^+$P wave and $1^-4^{++}1^+$F wave.

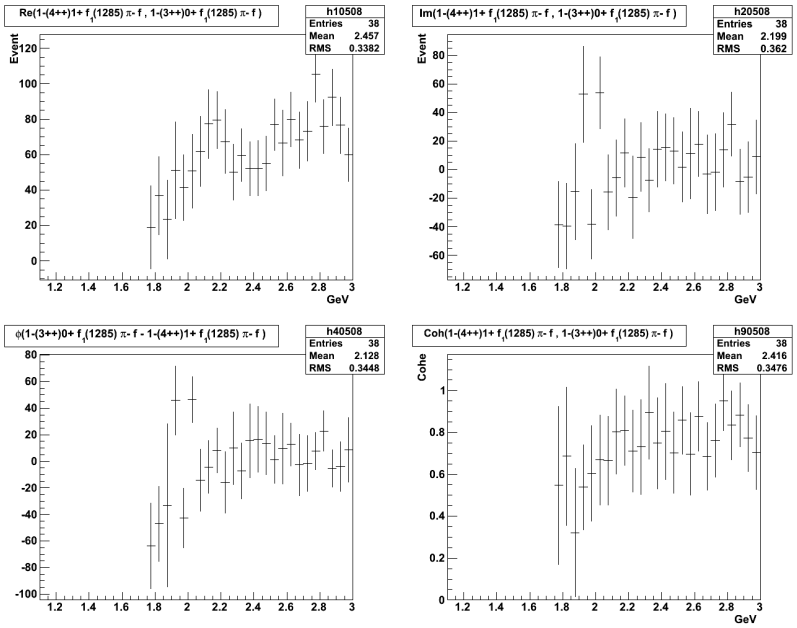

Figure D.18: Like figure D.1 for $1^-4^{++}1^+$F wave and $1^-3^{++}0^+$F wave.

Bibliography

[1] G. Ascoli. *Partial Wave Analysis of the 3π Decay of the A2.* Phys. Rev. Lett. 25: 962-965, 1970.

[2] D. Aston. *Evidence for two strangeonium resonances with $J^{PC} = 1^{++}$ and 1^{+-} in K^-p interactions at 11GeV/c.* Phys. Lett. B201: 566-573, 1988.

[3] G. Bali. *Lattice calculations of hadron properties.* Eur. Phys. J. A19: 1-8, 2004.

[4] V. Bernard und U. Meissner. *Chiral perturbation theory.* Ann. Rev. Nucl. Part. Sci.57: 33-60, 2007.

[5] J. Bernhard. *Aufbau des inneren Rings eines Recoildetektors am COMPASSExperiment.* Johannes-Gutenberg-Universität Mainz, Diplomar, 21-31, 2007.

[6] M. Bettinelli. *Exclusive $\omega\pi^0$ production with muons at COMPASS.* PHD thesis, Ludwig-Maximilians-Universität München, 2010.

[7] S. Chung. *Techniques of amplitude analysis for two pseudoscalar systems.* Phys. Rev. D56: 7299-7316, 1997.

[8] S. Chung und T.L. Trueman. *Positivity conditions on the spin density matrix: A simple parametrization.* Phys. Rev. D11: 633-646, 1975.

[9] P. Cummings. *The New BNL Partial Wave Analysis Programs.* Phys. Rev. D11: 633-646, 1975.

[10] M. Diefenbach. *Monte Carlo Analysis of The Acceptances In The $\pi^-\eta'$ and $\pi^-\eta$ Final states at COMPASS(CERN).* Diploma thesis, Ludwig-Maximilians-Universität München, 2011.

[11] S. Dinter. *Analysis of Final States with π^0 and η Mesons produced in $\pi^- p$ interactions and Studies of the Electromagnetic Calorimeters at COMPASS*. Diploma thesis, Ludwig-Maximilians-Universität München, 2010.

[12] S. Dinter. *Interactions and Studies of the Electromagnetic Calorimeters at COMPASS (CERN)*. 2010.

[13] F. Englert. *Broken Symmetry and the Mass of Gauge Vector Mesons*. Physical Review Letters 13: 326-333, 1964.

[14] A. Ferrero. *Light mesons spectroscopy and search for non-$q\bar{q}$ mesons at COMPASS*. COMPASS International Workshop Freiburg, 19 March 2007.

[15] From:CERN. Http://wwwcompass.cern.ch/compass/software/offline.

[16] From:CERN. *Physics Analysis Sofeware Tools*. 2010.

[17] From:CERN. *Worlds Largest Silicon Tracking Detector Installed At CERN*. Science Daily Article, 2007.

[18] From:COMPASS. Http://www.staff.uni-mainz.de/jasinsk/.

[19] From:COMPASS. Http://wwwcompass.cern.ch/compass/software.

[20] From:COMPASS. *Common Muon Proton Apparatus for Structure and Spectroscopy*. 2008.

[21] From:COMPASS. *Compass Trigger and Trigger Control System*. Retrieved February 12, 2010.

[22] From:COMPASS. *Location of the COMPASS experiment at CERN*. 2010.

[23] From:COMPASS. *A proposal for a Common Muon and Proton Apparatus for Structure and Spectroscopy*. CERN SPSLC 96: 3-22, 1996.

[24] From:COMPASS. *Sandwich Veto Detector*. COMPASS publication, 2011.

[25] From:GEANT. *GEANT-Detector Description and Simulation Tool*. 1993.

[26] From:PDG. *center of mass system*. 287-288, 2010.

[27] From:PDG. *Spherical Harmonic*. 286, 2010.

[28] From:PDG. *two-body reactions*. 288-289, 2010.

[29] From:Root. Http://root.cern.ch/drupal/content/usersguide.

[30] From:Wiki. *Fermions*. Http://en.wikipedia.org/wiki/StandardModel.

[31] From:Wiki. *Gauge bosons*. Http://en.wikipedia.org/wiki/StandardModel.

[32] From:Wiki. *Meson*. Http://en.wikipedia.org/wiki/Meson.

[33] From:Wiki. *Parity*. Http://en.wikipedia.org/wiki/MesonParity.

[34] From:Wiki. *Quark Model*. Http://en.wikipedia.org/wiki/QuarkModel.

[35] From:Wiki. *Quark Model*. Http://en.wikipedia.org/wiki/QuarkModel.

[36] From:Wiki. *Standard Model*. Http://en.wikipedia.org/wiki/StandardModel.

[37] S. Glashow. *Partial-symmetries of weak interactions*. Nuclear Physics 22: 579-588, 2008.

[38] S. Grabmuller. *Studies of Diffractive Particle Production at COMPASS*. Garching, 2005.

[39] O. Greenberg. *Spin and Unitary-Spin Independence in a Paraquark Model of Baryons and Mesons*. Physical Review Letters 13: 598, 1964.

[40] G. Guralnik. *Global Conservation Laws and Massless Particles*. Physical Review Letters 13: 585-587, 1965.

[41] D. Haidt. *The discovery of the weak neutral currents*. CERN Courier. http://cerncourier.com/cws/article/cern/29168. Retrieved 2008.

[42] J. Hammersley. *Monte Carlo Methods*. 2003.

[43] M. Han. *Three-Triplet Model with Double SU(3) Symmetry*. Physical Review 139: B1006, 1965.

[44] D. Hansen. *Formalism and Assumptions involved in Partial-Wave Analysis of three-Meson Systems*. Nucl. Phys. B81: 403-430, 1974.

[45] F. Hasert. *Search for elastic muon-neutrino electron scattering*. Physics Letters B46: 121-123, 1973.

[46] J. Hasert. *Observation of neutrino-like interactions without muon or electron in the gargamelle neutrino experiment*. Physics Letters B46: 138-139, 1973.

[47] J. Hedditch. 1^{-+} *exotic meson at light quark masse*. Phys. Rev.D72: 1-17, 2005.

[48] P. Higgs. *Broken Symmetries and the Masses of Gauge Bosons*. Physical Review Letters 13: 508-509, 1964.

[49] B. Johannes: *Aufbau des inneren Rings eines Recoildetektors am COMPASS-Experiment*. Johannes-Gutenberg-Universite Mainz, Diplomarbeit, Dezember 2007.

[50] J. Keters. *partial wave analysis*. Int. J. Mod. Phys. A21: 618-624, 2006.

[51] T. Manke. *Hybrid quarkonia on asymmetric lattices*. Phys. Rev.Lett. 82: 4396-4399, 1999.

[52] C. McNeile und C. Michael. *Decay width of light quark hybrid meson from the lattice*. Phys. Rev. D73: 7-16, 2006.

[53] N. Metropolis. *Equation of State Calculations by Fast Computing Machines*. Journal of Chemical Physics 21(6): 87-90, 1953.

[54] N. Metropolis. *The Monte Carlo Method*. Journal of the American Statistical Association 44(247):335341, 2006.

[55] C. Morningstar und M. Peardon. *The Glueball spectrum from an anisotropic lattice study*. Phys. Rev. D60: 1-13, 1999.

[56] R. Omnes. *Mandelstam Theory Regge Poles*. 1963.

[57] K. Peters. *A Primer on partial wave analysis*. Phys. Lett. B352: 463-467, 1995.

[58] D. Ryabchikov. *private communication*. Dmitri.Riabtchikov@cern.ch.

[59] V.D. S. Denisov. *A partial wave analysis of the $\pi^-\pi^-\pi^+$ and $\pi^-\pi^0\pi^0$ systems and the search for $J^{PC} = 1^{-+}$ meson*. Department of Physics and Nuclear Theory Center, 2008.

[60] S. Tobias. *D. Wolfgang and S. Tobias private communication*. 2011.

[61] I. Uman. *Study of diffractively and centrally produced resonances in $\pi^-p \to \pi^-\pi^0(\eta)p$ and $\pi^-p \to \pi^-\pi^0\pi^0(\eta\eta)p$*. CERN, 2009.

[62] A. Vasilescu. *The Particle Detector BriefBook*. 2006.

[63] Q. Weitzel. *Precision Meson Spectroscopy: Diffractive Production at COMPASS and Development of a GEM-based TPC for PANDA*. PHD thesis, Technic Universite Munich, 2008.

[64] H. Wöhrmann. *Diffractive production of 3-body final states in $\pi^- p$ interactions at the COMPASS experiment(CERN).* Diploma thesis, Ludwig-Maximilians-Universität München, 2011.

Danksagung

First of all I am very grateful to my tutor Martin Faessler, who giving me the opportunity to work on these interesting subjects. He always supported my work and gave the important guide and supervised me throughout all these years. From him I learned what is the means to work in a scientific way, and his accuracy has always been an ideal for me. In a word, It is hard to express my appreciate for all the help of Martin. In a word, Deepest gratitude for Martin's nice.

Then I will thank Wolfgang for his help, every time he can let me go to the right way when I am confused. Thanks for Meike, she was very nice to rent the house for me and give me a very beautiful bike. With this bike I have more chance to view the scenery in Munich which will be very nice remembrance for all my life.

Thanks for Hauke, I am very happy to do the research together with him. The only pity is that the together time is so short. Sincerest thanks to Dmitri Ryabchikov. Dima never got tired to explain me again and again the secrets of PWA and it was great fun to work with him. Still thanks for Tobias, we work together four years and he give me lots of help about program.

My parents have been a great support for me during these years, and their interest in my research has always been a great motivation for me. Thanks a lot!